# RESEARCH REPORT

BATTELLE MEMORIAL INSTITUTE

COLUMBUS LABORATORIES

BATTELLE MEMORIAL INSTITUTE

COLUMBUS LABORATORIES ● 505 KING AVENUE ● COLUMBUS, OHIO 43201

DEDICATED TO THE ADVANCEMENT OF SCIENCE

FIELDS OF RESEARCH

Aeronautics — Astronautics
Agricultural Chemistry
Agricultural Economics
Alloy Development
Applied Mathematics
Area Economics
Biochemistry
Biophysics — Bionics
Catalysis — Surface Chemistry
Ceramics
Chemical Engineering
Chemical Processes
Communications Science
Computer Technology
Corrosion Technology
Earth — Atmospheric Sciences
Electrochemistry
Electronics
Energy Conversion
Engineering — Structural Materials
Environmental Systems
Extractive Metallurgy
Extreme-Temperature Technology
Ferrous Metallurgy
Food Technology

Foundry Practice
Fuels — Combustion
Glass Technology
Graphic Arts Technology
Immunology — Cancer Studies
Industrial Economics
Industrial Physics
Information Research
Inorganic Chemistry
Instrumentation
Light Alloys — Rare Metals
Lubricant Technology
Materials Separation — Concentration
Mechanical Engineering
Metal Fabrication Engineering
Metal Finishing
Metallurgical Processes
Microbiology
Microscopy — Mineralogy
Nondestructive Evaluation Technology
Nonferrous Metallurgy
Nucleonics
Ocean Engineering
Organic Chemistry

Organic Coatings
Packaging Research
Particle Dynamics
Petrochemicals
Petroleum Engineering
Pharmaceutical Chemistry
Physical Chemistry
Production Engineering
Psychological Sciences
Pulp — Paper Technology
Radioisotopes — Radiation
Reactor Technology
Refractories
Reliability Engineering
Rubber — Plastics
Semiconductors — Solid-State Devices
Sound — Vibration
Systems Engineering
Textiles — Fibers
Theoretical — Applied Mechanics
Thermodynamics
Transportation
Welding — Metals-Joining Technology
Wood — Forest Products

FINAL SUMMARY REPORT

on

AN ADVANCED THERMOELECTRIC
COMPONENT DEVELOPMENT
PROGRAM

to

NATIONAL AERONAUTICS AND SPACE
ADMINISTRATION
GODDARD SPACE FLIGHT CENTER

February 18, 1966

W. E. Kortier, Program Director

BATTELLE MEMORIAL INSTITUTE
Columbus Laboratories
505 King Avenue
Columbus, Ohio   43201

DISTRIBUTION LIST

Addressee	No. of Copies

NASA-Goddard Space Flight Center
Greenbelt, Maryland 20771
Attention:

Office of the Director — Code 100	(1)
Office of the Assistant Director for Administration and Technical Services — Code 200	(3)
Office of the Assistant Director for Projects — Code 400	(1)
Office of the Assistant Director for Systems Reliability — Code 300	(1)
Office of the Assistant Director for Tracking and Data Systems — Code 500	(1)
Office of the Assistant Director for Space Sciences — Code 600	(1)
Office of the Assistant Director for Technology — Code 700	(1)
GSFC Library — Code 252	(2)
Contracting Officer — Code 247	(1)
Technical Information Division — Code 250	(4)
Technical Representative — Code 716.4	(2)

<u>(1) reproducible</u>

1 copy to each of the following:

Mr. Milton Knight
Bureau of Naval Weapons
Code RAAE-511
Department of the Navy
Washington, D.C.

Mr. Bernard B. Rosenbaum
Bureau of Ships (Code 342B)
Department of the Navy
Washington, D.C.

Mr. Robert T. Carpenter
Division of Reactor Development
Auxiliary Power Branch
U. S. Atomic Energy Commission
Washington, D.C.

Mr. Charles Glassburn
NASA-Manned Spacecraft Center
Houston, Texas 77058

Mr. Peter Rouklove
Jet Propulsion Lab
4800 Oak Grove Drive
Pasadena, California 91103

Mr. Robert English
NASA-Lewis Research Center
Code 86-5
21000 Brookpark Road
Cleveland, Ohio 44135

Dr. Fred Schulman
NASA Code RNP
Washington, D.C. 20548

Mr. Arvin Smith
NASA Headquarters Code RNW
1512 H Street, N.W.
Washington, D.C. 20546

Mr. Richard Ferguson
NASA-Manned Spacecraft Center
Houston, Texas 77058

Capt. Robert Morrow
APIP-2
Wright-Patterson Air Force Base
Dayton, Ohio

Dr. R. Roberts
Office of Naval Research
Washington, D.C.

B A T T E L L E   M E M O R I A L   I N S T I T U T E

Mr. Howard Matthews
NASA-Ames Research Center
Moffett Field
California 94035

Dr. Robert C. Hamilton
Research & Engineering Support
  Division
Institute for Defense Analyses
1825 Connecticut Avenue, N.W.
Washington, D.C.

Dr. Francis Schwarz — Code SP
NASA-Electronics Research Center
5775 Technology Square
Cambridge, Massachusetts 02139

Mr. Bayne Neild
U. S. Navy — Code 843
Marine Engineering Laboratory
Annapolis, Maryland

Mr. Paul R. Berthaud
APIP-3
Wright-Patterson Air Force Base
Dayton, Ohio

Mr. Bernard Leefer
NASA Code RNP
Washington, D.C. 20546

Mr. James L. Cioni
Code EP21
NASA-Manned Spacecraft Center
Houston, Texas 77058

Mr. Robert Berlin
AEC-New York Operations Office
376 Hudson Street
New York, New York

Mr. John Goldsmith
Jet Propulsion Laboratory
4800 Oak Grove Drive
Pasadena, California 91103

TABLE OF CONTENTS

LIST OF TABLES

LIST OF FIGURES

AN ADVANCED THERMOELECTRIC COMPONENT
DEVELOPMENT PROGRAM

ABSTRACT

28906

The tasks in the program are segregated by diverse technologies and are reported as separate chapters in this report. Under Task I, Computer Code Modification, a new program based upon the extension and generalization of an existing program has been written, debugged, and operated. The program in its present form is capable of analyzing thermoelectric generators for space use where the design under investigation uses the static heat-transfer mode and geometries based upon right-cylindrical configurations. A rapid means of analysis, which can treat large numbers of cases in order to identify minimum-weight designs, is available as a fundamental tool in lieu of time-consuming and repetitive manual computations. The work performed under Task II, High-Temperature Segmented Thermoelectric Development, progressed to the point where a series of fabrication schemes and segmented element configurations have been examined. Fundamental studies of thermoelectric materials properties, transition member bonding between SiGe and PbTe materials, hot shoe bonding to GeSi material, and PbTe-segment fabrication were performed to support the selection of the fabrication schemes and segmented element configurations. Under Task III, Development of a Thermal Insulation and Support Structure, test specimens composed of multilayered webs and foils and representing variances in web and foil thickness and web spacing have been fabricated and tested. A test program consisting of shear and mechanical strength and heat-transfer measurements was performed. The experimental data were reduced and compared to analytical predictions. A parametric display of the parameters of interest, weight, heat transfer, and strength was made.

i

INTRODUCTION

This is the Final Summary Report issued under Contract NAS5-9160 by Battelle Memorial Institute for National Aeronautics and Space Administration, Goddard Space Flight Center. Work under the program was initiated April 6, 1965, and was performed in three tasks.

Task I. Computer Program Modification

An existing program for the analysis of thermoelectric generators for space use was extended and generalized. The program was checked out by performing analyses on 50-watt(e) and 250-watt(e) generators. The program was delivered to NASA-Goddard Space Flight Center.

Task II. High-Temperature Segmented Thermoelectric Development

Development work leading to a demonstration of the feasibility of segmenting GeSi and PbTe materials was performed. Fabrication trials were performed utilizing a series of fabrication schemes and segmented element configurations. Limited tests, under simulated operating conditions, were performed on two segmented thermoelectric couples.

Task III. Development of a Thermal Insulation and Support Structure

Fabrication, thermal testing and structural testing were performed on structural insulation specimens designed to represent a broad range of weight, heat-transfer, and strength combinations. Two problematic factors appeared in this development: (1) a significant transition occurred at elevated temperatures in the material chosen for fabrication and (2) approximate methods were required to determine the emittance of the interior surfaces of the insulation structures. Despite these factors, a correlation between experimental data and the postulated design equations was made and verified. The resulting expressions were displayed parametrically so that optimum designs in terms of materials selection, weight, heat transfer and strength may be made for specific applications.

The ensuing chapters are identified by task and have been prepared by P. E. Eggers (Task I), J. J. Mueller and D. G. Freas (Task II), and J. J. Ketchman and R. H. Wittman (Task III).

TASK I. <u>COMPUTER PROGRAM MODIFICATION</u>

TASK I. COMPUTER PROGRAM MODIFICATION

Objective

The objective of this work is to modify an existing thermoelectric digital-computer program for the analysis of thermoelectric generators to achieve:

(1) A generalized program in which the design parameters will be located in the input-data section of the code

(2) An extended program in which subroutines will be added to establish a more complete analysis of the thermal balance, dimensions, and weight of the thermoelectric generator

(3) A detailed program which will trade off total generator weight with thermoelectric dimensions, end-insulation and radial-insulation thickness, and generator length.

Scope of Work

The program was expanded to include the treatment of all known phases of thermoelectric-generator analysis. This included enumeration of the major- and minor-component dimensions and weights, thermal losses through the media surrounding the heat source, and a detailed balance of heat losses with fuel inventory. In addition, the flexibility of the program was extended to include the analysis of several fuel-form arrays, several heat-source-support methods, and thermoelectric arrays. Options have been included in the program to trade off the end-insulation thickness, thermoelectric-element length, and generator length with the total generator weight. An input instruction can be given to the program to (1) print out all calculated data; (2) print out only the total generator weight and a limited number of pertinent generator dimensions (i. e., generator length, end-insulation thickness, element length, and thermoelectric array); and (3) operate a minimum-seeking iterative loop which identifies and prints out data for only the minimum-weight generator.

Formulation of Analytical Model

An analytical model was formulated emphasizing a general case for the design layout of thermoelectric generators. The model is limited to the static-heat-transfer concept and geometries built upon right-cylindrical configurations. The model contains the major and minor weight-contributing components of the generator in a preselected geometric configuration. The major weight-contributing components are:

(1) Fuel form
(2) Fuel-form cladding and liner
(3) Thermoelectrics
(4) Generator case and the radiator fins.

The minor weight-contributing components include:

(1) Insulation

(2) Heat-source support

(3) Thermoelectric associated hardware (peripheral material, interelement insulation, cold- and hot-junction hardware)

(4) Ablator.

Using a parametric approach to generator analysis, the design conditions governing the above-mentioned components can be varied over a range of values yielding minimum-weight combination(s). Sketches (two views) representing the geometric configuration of the model are shown in Figure 1. The nomenclature used for identification of the components is given in the Glossary of Computer Program Terms, Appendix A, Part I.

The fixed conditions of the analytical model are that the fuel form must conform to one of three geometries:

(1) Right-cylinder geometry for single fuel form

(2) Right-cylinder geometry for fuel pins and overall right-cylinder geometry for a fuel block with the locus of all fuel-pin centers being a circle

(3) Right-cylinder geometry for fuel pins in an overall right-cylinder geometry for fuel block with close packing of fuel pins.

These fuel-form arrays are illustrated in Figure 2. Also, the radiator-fin length is constrained to match the generator length (this length excludes the optional ablative thickness on the generator shell).

Development of Computer Program

Based upon the analytical model, the computer program logic provides for the acceptance of input data, the computations, and the handling of output data. The program has been generalized by writing all design parameters into the input data section.

Program Inputs

The program inputs are listed in the Glossary of Computer Program Terms appearing in Appendix A, Part I, and include the following categories:

(1) Material properties of all components (density, thermal conductivity, power density, thermoelectric parameters, modulus of elasticity, emissivity, toughness parameter)

(2) Generator power output (e)

(3) Radiator-fin length, thickness, and weight parameters corresponding to the number of fins selected

(4) Range of generator lengths
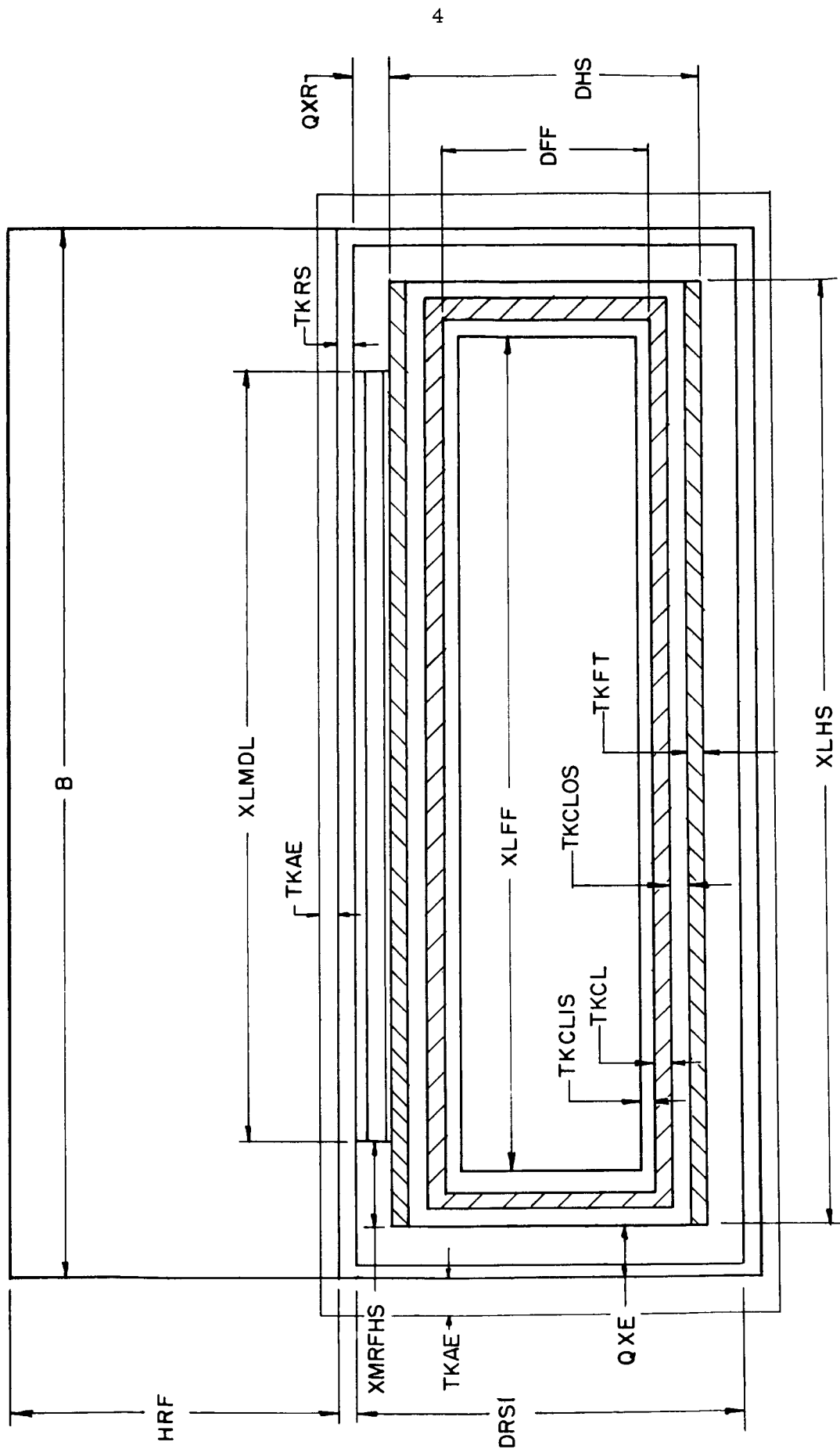
FIGURE 1. ANALYTICAL MODEL

a. Side View

K747-294

BATTELLE MEMORIAL INSTITUTE

b. End View

K747-293
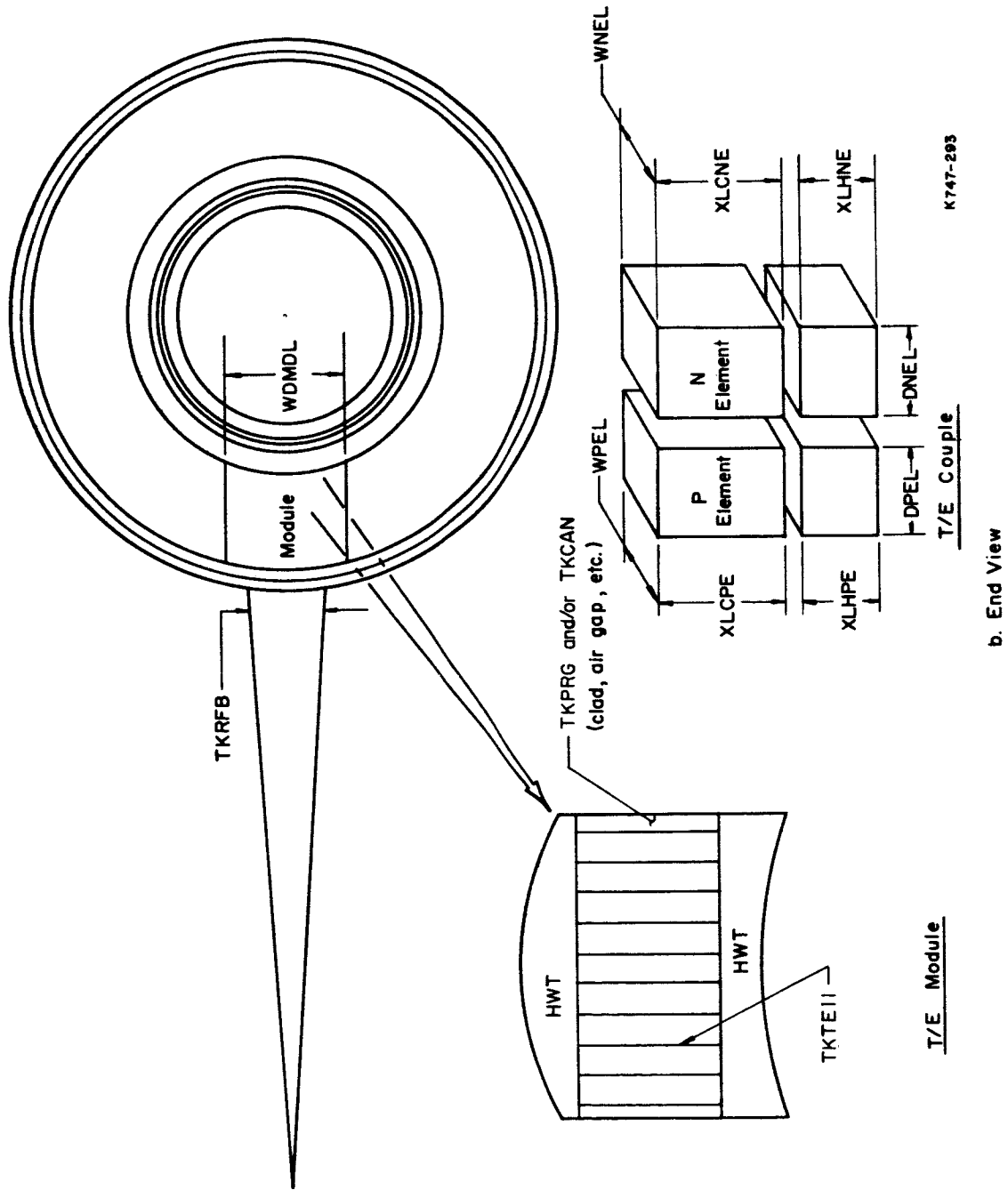
FIGURE 1. (CONTINUED)
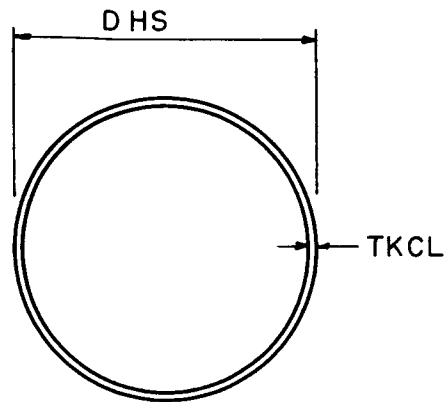
a. Right cylinder geometry for single fuel form
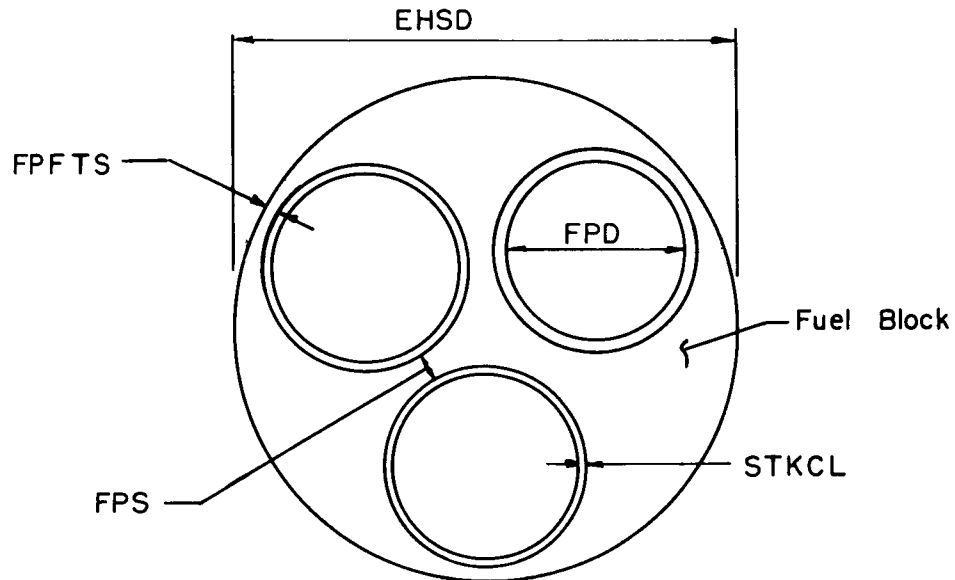
b. Locus of all fuel pin centers form a circle
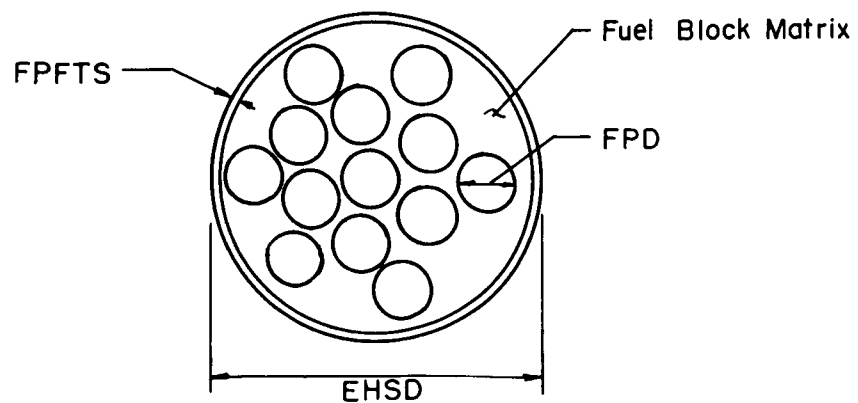
c. Close packing of fuel pins in fuel block matrix

K747-284

FIGURE 2. FUEL-FORM-ARRAY OPTIONS

BATTELLE MEMORIAL INSTITUTE

(5) Thickness of optional inner and outer claddings, ablator, fuel tube, module periphery, thermoelectric shoes, interelement electrical insulation, generator shell, radiation gap, thermoelectric hardware, end and radial insulation, end and radial heat-source support

(6) Thermoelectric current, L/A ratio, and element segment number

(7) Number of modules

(8) Limiting aspect ratios of fuel form, generator casing, and generator envelope

(9) Heat-transfer mode (conductive or radiative)

(10) Temperature profile of generator

(11) Percent of total heat-dump capability of generator ends

(12) Tolerable deflection of heat source based on compression and shear modulus of heat-source support

(13) "g" loading axially and radially

(14) Impact velocity of heat source (cladding analysis)

(15) Epsilon (tolerance) and delta (iterative steps) functions

(16) Maximum number of allowed iterations specified for each subroutine

(17) Optional choice of thermoelectric array (the option to have thermoelectrics, in module form, limited either by heat-source length or heat-source width, or have couples individually dispersed in a matrix and surrounded by insulation)

(18) Generator computation sequence (the option to use fixed iterative steps between a minimum and maximum value of generator length, or to use large iterative steps until the minimum weight point is exceeded and to use small iterative steps to locate accurately the minimum weight point)

(19) Thermoelectric-element length computation option (the option to iterate upon element length and print out after each iteration, to print out only after the minimum-weight generator has been reached, or to fix the element length)

(20) Fuel-form array (the option to select for analysis one of three available fuel-form arrays, outlined in the section Formulation of the Analytical Model

(21) Heat-source support option (the option to effect support by the ends of the heat source only, by the radial portion of the heat source only, or by both the ends and the radial portion)

(22) End insulation computation option (the option to iterate upon end-insulation thickness and print out after each iteration, to print out only after the minimum-weight generator has been reached, or to fix the end-insulation thickness).

The optional analyses described in Items (17) through (22) above can be used by iterating on component dimensions and evaluating their effect on the total generator weight. For example, if the thermoelectric-element length is iterated upon, the total area of the thermoelectric module changes in addition to the radial-insulation thickness

which follows the element length. Indirectly, the variation of the element length changes the radial bearing area available for heat-source support and also the surface-power-density requirements, total generator-shell dimensions, and weight of the thermoelectrics. In a similar fashion, the program is capable of iterating upon the end-insulation thickness, total generator length, and thermoelectric-element array to investigate their effect upon the other components of the generator and the total generator weight.

An iteration control has been included in the program to economize on computer operation time. This control mechanism adjusts the size of the iterative steps (delta functions) and tolerance values (epsilon functions) to avoid excessive loss of computer time as a result of inappropriately selected values of these functions. The iteration control will monitor the number of iterations performed, known as the iteration index number, and will terminate the analysis and print out a diagnosis if an adjustment fails to produce a solution within a prescribed recurrence limit.

Program Computations

The computational scheme of the computer code is illustrated in Figure 3 and is itemized in subroutines below. The majority of the subroutine computations are straightforward. However, those that involve more sophisticated treatment have been referenced.

(1) Thermal-Input and -Output Analysis

    Calculate: Heat required

                  Heat dump.

(2) Fuel-Form Analysis

    Calculate: Fuel-form volume

                  Fuel-form weight

                  Fuel-form dimensions

                  Number of fuel pins.

(3) Segmenting Subroutine

    Maintain fuel form within limiting aspect ratio

    Calculate: Number of fuel-form segments.

(4) Cladding Analysis[1]

    Calculate: Thickness of cladding

                Weight of cladding

                Thickness and weight of inner and outer claddings.

---

(1) Analysis is based on mass required to absorb energy of impact. The development of this analysis appears in NASA Contract NAS5-3697 Final Report.
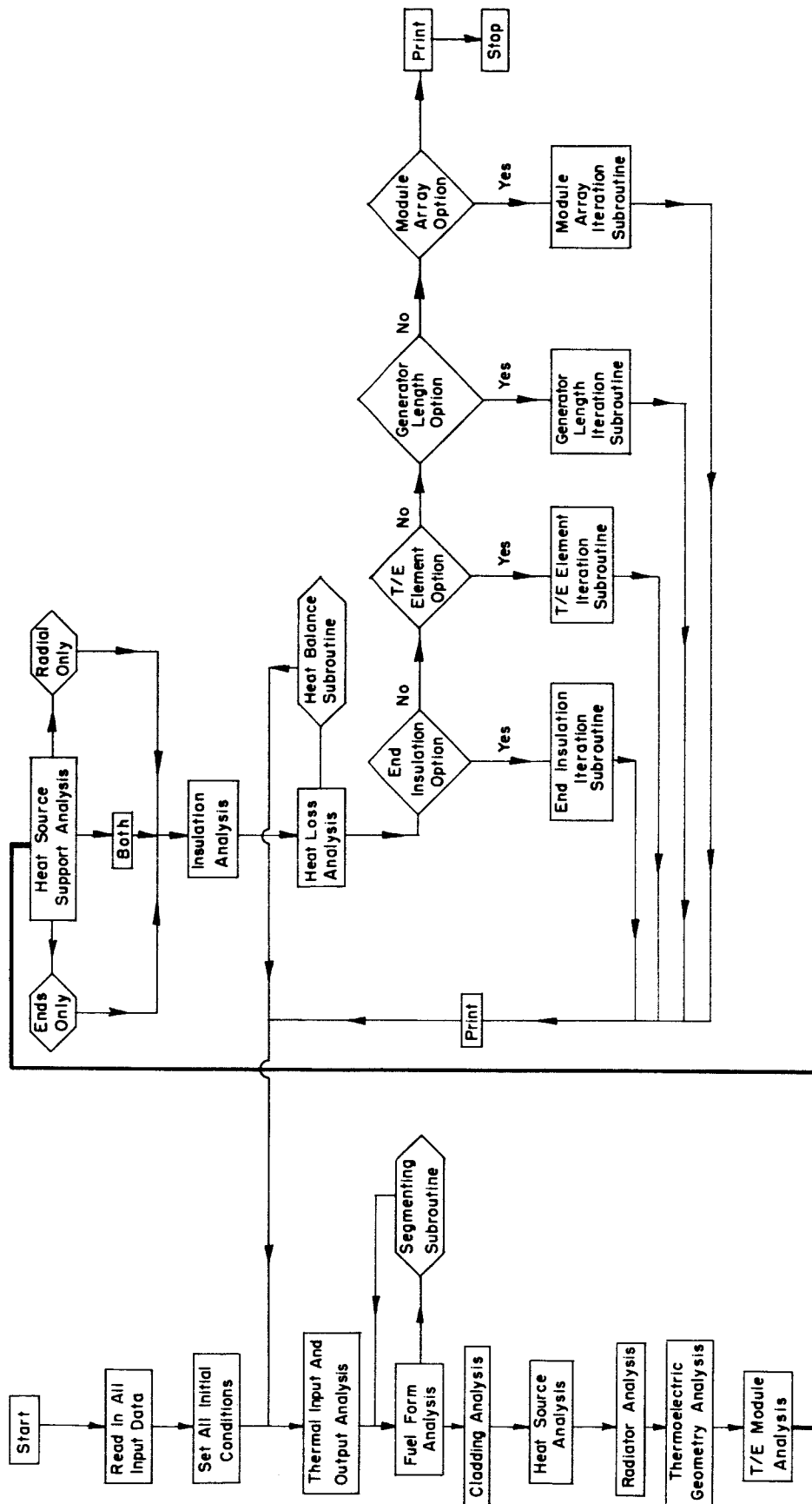
FIGURE 3. COMPUTER CODE FLOW CHART

(5) Heat-Source Analysis

    Calculate: Heat-source length

                      Heat-source diameter

                      Heat-source volume

                      Heat-source surface area (available for T/E coverage)

                      Fuel-block weight.

(6) Radiator Analysis[2]

    Calculate: Radiator-fin height

                      Radiator-fin thickness (base)

                      Generator-shell diameter (inside)

                      Generator-shell weight

                      Radiator-fin weight.

(7) Thermoelectric Geometry Analysis

    Calculate: Number of couples

                      Number of elements

                      Number of couples per module

                      N-element dimensions

                      P-element dimensions.

(8) Thermoelectric-Module-Array Analysis

    Calculate: Module width

                      Module length

                      Module depth

                      Heat-loss area for module periphery

                      Module weight

                      Weight of module periphery

                      Thermoelectric weight

                      Surface power-density required.

---

(2) This analysis is developed in the Final Report of NASA Contract NAS5-3697, page 25.

(9) Heat-Source-Support Analysis and Subroutine*

   Calculate: Area required for transverse support

                Area required for longitudinal support

                Weight of heat-source support (radially)

                Weight of heat-source support (ends)

                Deflection of support under given conditions (ends)

                Deflection of support under given conditions (radially).

(10) Insulation Analysis

   Calculate: Area available for radial insulation

                Area available for end insulation

                Weight of insulation (ends)

                Weight of insulation (radially).

(11) Heat-Loss Analysis

   Calculate: Heat loss through electrical and thermal insulation

                Heat loss through module periphery

                Heat loss through radial insulation[3]

                Heat loss through end insulation[3]

                Heat loss through radial heat-source support[3]

                Heat loss through end heat-source support[3]

                Effective surface power density available for module

                Total heat loss.

(12) Heat-Balance Subroutine

   Calculate: Engineering efficiency.

(13) End-Insulation Subroutine

   Iterate on end-insulation thickness

   Calculate: All output data.

(14) Thermoelectric-Element Subroutine

   Iterate on element length

   Calculate: All output data.

(15) Generator-Length Subroutine

   Iterate on generator length

   Calculate: All output data.

---

*See Appendix B.

(3) This analysis is discussed in the Final Report of NASA Contract NAS5-3697, page 40.

Outputs and Example Cases

The output data listed in the Glossary of Computer Program Terms (Appendix A, Part I) contain the following categories:

(1) Dimensions
(2) Weights
(3) Thermal losses
(4) Iteration index numbers.

The output data may be handled in several ways:

(1) Print out all calculated data for each generator case considered

(2) Print out only the data associated with the minimum-weight generator

(3) Plot data directly onto an X-Y plotter by means of array storage of the pertinent data, thus eliminating the time required for manual manipulation of data.

Several test cases were used in the development of the computer program. These included radioisotope generators at output power levels of 50 and 250 watts(e) having fuels that are characterized by 3.7 and 5.7 watts/cm^3 power densities. Two examples of the 250-watt(e) case are shown in Figures 4 and 5 to illustrate the dependence of generator component weights upon generator length, B. This relationship is also shown for the 50-watt(e) case in Figure 6. These figures are tracings of the originals made directly by the computer plotter. The speed of modern computers permits the analysis of about one case per second with 110 bits of output information per case.

Operation Manual

A manual for the operation of the program entitled, "The Space Generator Computer Program Operation Manual" has been written and appears in Appendix A. The manual includes:

(1) Glossary of Computer Program Terms (Appendix A, Part I)

This is a lexicon of the input and output computer language, containing both the definition and the physical units of the terms.

(2) Input Data Form (Appendix A, Part II)

This is a list of program inputs. Several of the inputs are referenced and further discussed in the Input Data Reference section of the appendix to aid in the data compilation.

(3) Appendix of Recommended Inputs (Appendix A, Part III)

This list contains suggested epsilon and delta functions for use as a starting point in a particular program. These inputs have been estimated on the basis of trial cases of 50- and 250-watt(e) generators.
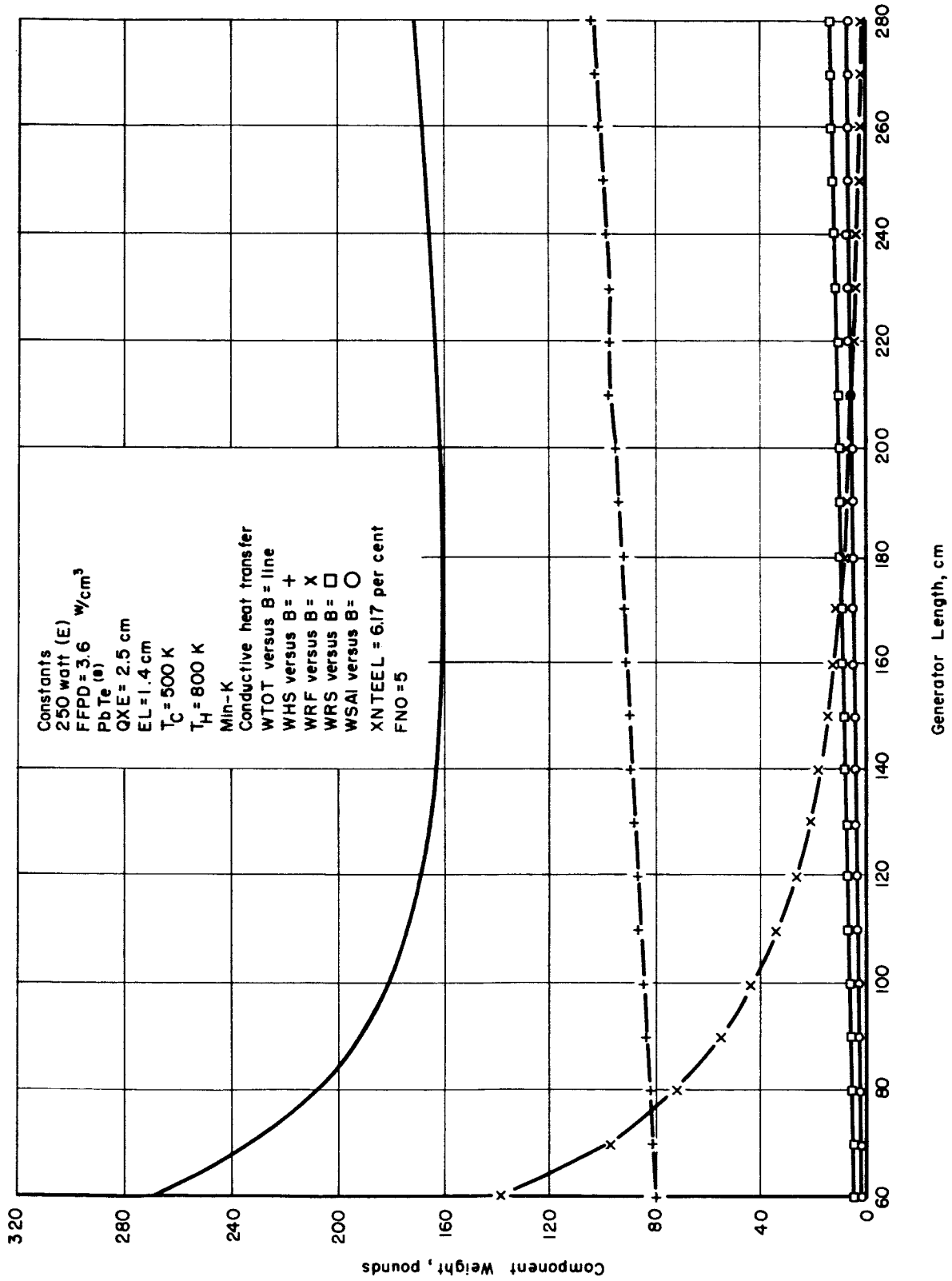
FIGURE 4. GENERATOR COMPONENT WEIGHT VS GENERATOR LENGTH
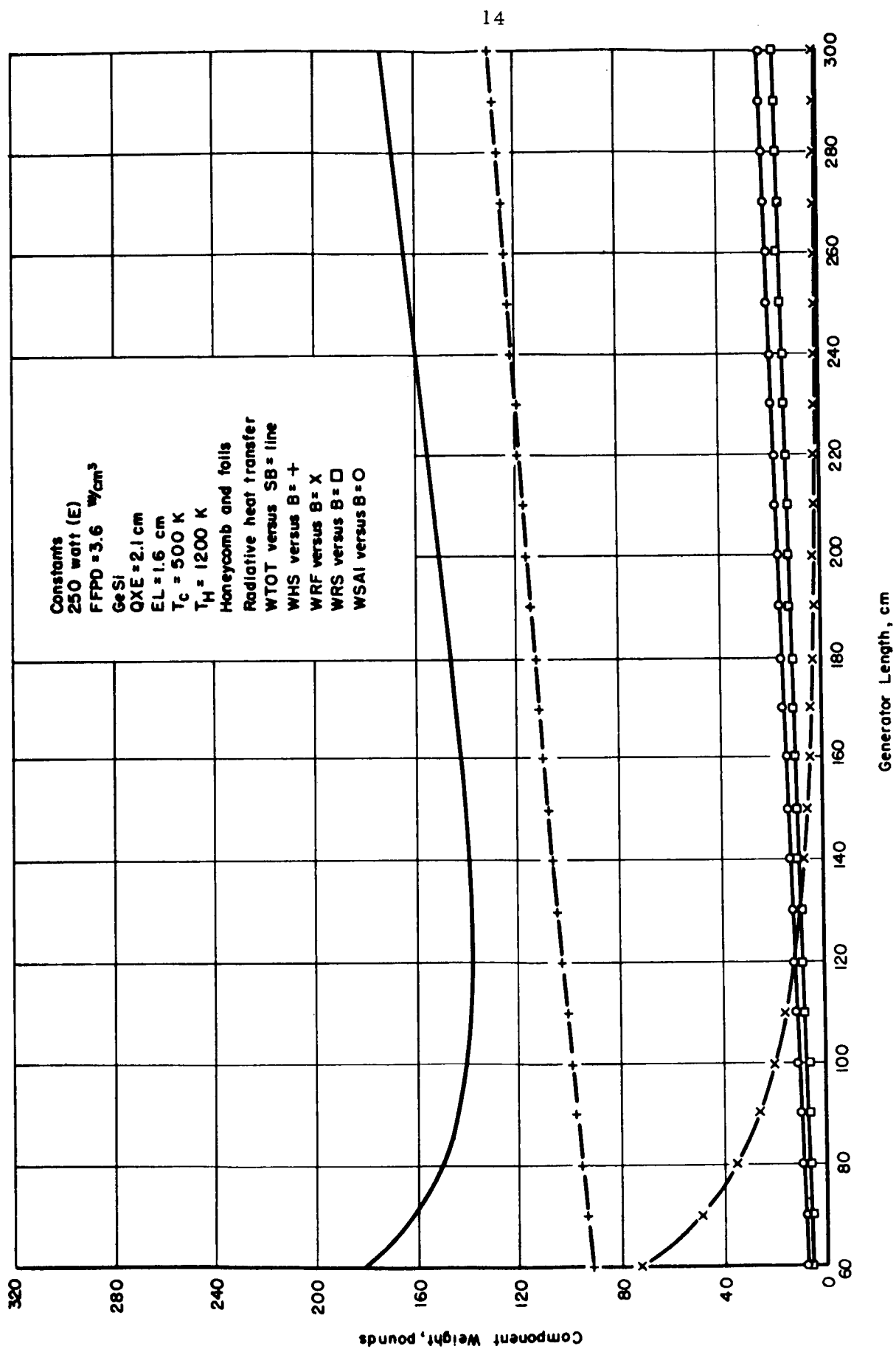
FIGURE 5.   GENERATOR COMPONENT WEIGHT VS GENERATOR LENGTH
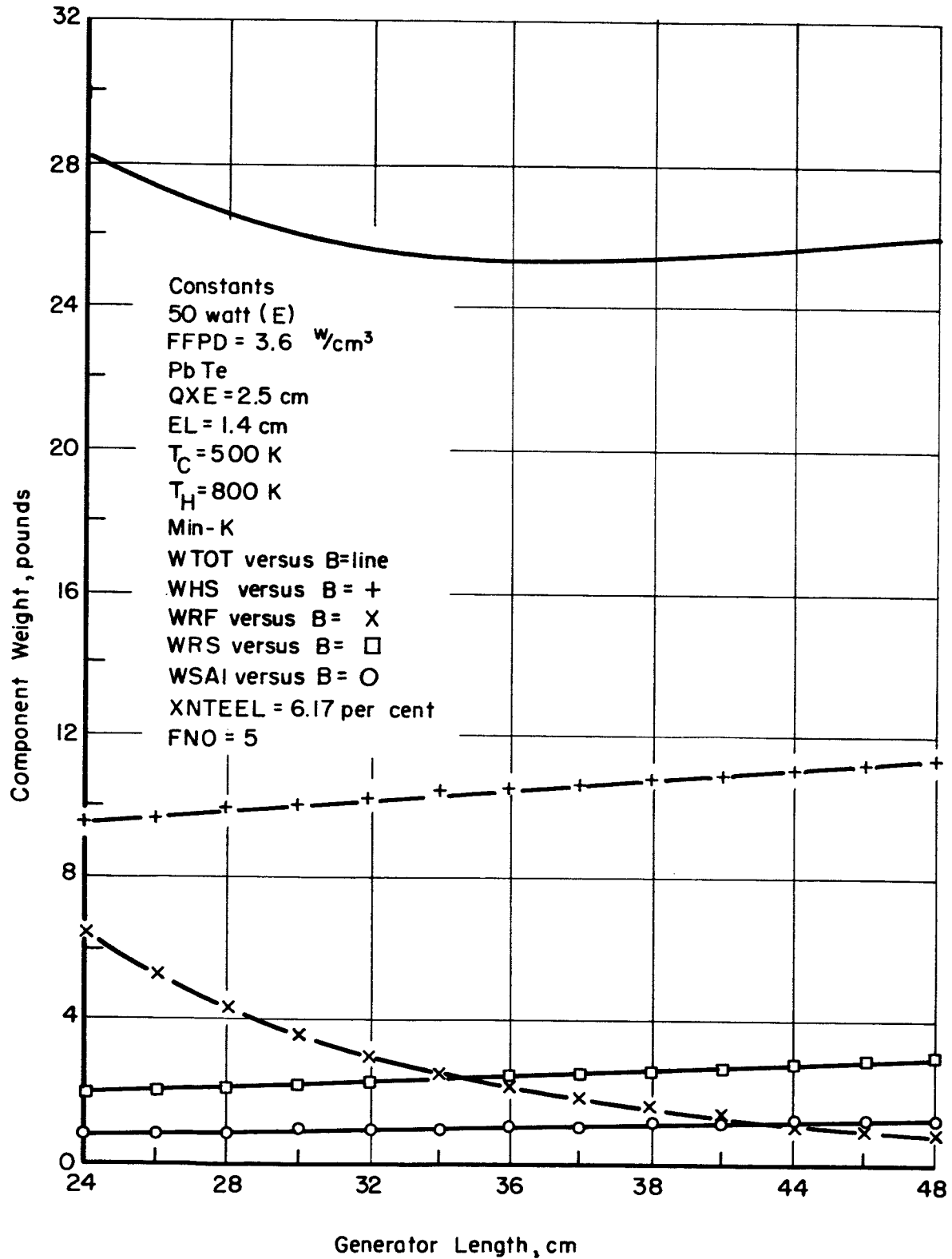
FIGURE 6. GENERATOR COMPONENT WEIGHT VS GENERATOR LENGTH

(4) Glossary of Diagnoses (Appendix A, Part IV)

   This list contains the corrective measures that are printed out in the event of either an incorrect tolerance or iterative step function. The print-out is in the literal form shown.

Summary

  The space-generator computer program has been written and debugged and is now operating. The program provides a versatile and comprehensive analysis tool for the evaluation of space generators characterized by the static-heat-transfer operational mode and geometries of right-cylindrical configuration. The computations performed by the program have been extended to include the minor components of the generator and the energy balance of the device. Thus, the analysis performed by the code closely approximates a real generator design. A rapid means of space-generator analysis, which can treat large numbers of cases in order to identify minimum-weight designs, is now available as a fundamental tool in lieu of time-consuming and repetitive manual computations.

TASK II. HIGH-TEMPERATURE SEGMENTED
THERMOELECTRIC DEVELOPMENT

TASK II. HIGH-TEMPERATURE SEGMENTED THERMOELECTRIC DEVELOPMENT

Objective

The over-all objective of the thermoelectric development work is to demonstrate the feasibility of segmenting PbTe and SiGe materials. It is the goal of this work to demonstrate that a segmented couple operating between a hot-junction temperature of 1200 K (1700 F) and a cold-junction temperature of 300 K (25 F) will perform at a conversion efficiency of 10 percent or greater without significant degradation.

Scope of Work

The electrical properties of the thermoelectric materials were determined as a function of temperature to provide the data for the analysis of couple performance and calculation of segment lengths. Techniques for fabrication of a transition member between SiGe and PbTe, which have widely differing expansion rates, were studied. Tungsten was selected as the contacting member for the SiGe segment on the basis of its proven state-of-the-art usage. Iron was selected for the hot-end contacting member of the lead telluride on the basis of its generally exclusive usage and accepted chemical compatibility. A study of bonding SiGe to a tungsten shoe was initiated for the purpose of establishing a method of producing a bond which is compatible with the sequence and parameters of the over-all element-fabrication process. The fabrication of the PbTe segment, although based on state-of-the-art technology, was studied to determine the relative effects of selected hot-isostatic-pressing conditions on the general structural characteristics and PbTe-to-iron shoe bonds. A recently developed iron-base alloy (designated BMI-8) with an expansion rate intermediate between that of iron and PbTe was used as a shoe material for comparative evaluation in this program. The information generated from the supporting studies, which considered separately the different parts of the segmented element, was used to establish schemes for element-fabrication methods and element configuration.

Thermoelectric-Materials Characterization

The Seebeck coefficient and resistivity were determined as a function of temperature for lead telluride (PbTe) consolidated at two temperatures of interest and silicon germanium (SiGe) in its initially purchased, cast form. The data obtained provide the design curves for analytical determination of the segment lengths and the theoretical performance of the overall segmented PbTe-SiGe couple. The thermal conductivities were obtained from published data.

The apparatus utilized to obtain property measurements, details of test specimen fabrication, and results of the property measurements are discussed below.

Elevated-Temperature Seebeck-Coefficient
Test Apparatus

The Seebeck coefficient, which is the rate of change of Seebeck voltage with temperature, is one of the main parameters used to characterize thermoelectric materials. The units generally measured and those used in this work are microvolts per degree Centigrade. The Seebeck coefficient was determined as a function of temperature over the appropriate temperature range of operation for each material tested. The equipment used in making these measurements is shown schematically in Figure 7. Figure 8 shows the test apparatus which holds the thermoelement during testing.

To make the Seebeck-coefficient determination, the test element is fitted snugly between two spring-loaded electrodes which are held in guided Lavite insulating blocks. Each contact electrode contains a centrally located sheathed thermocouple which extends from the end of the electrode and supports the specimen at the thermocouple bead. The springs for providing the pressure contact are located at the cold end of the apparatus. The apparatus is slipped into a Vycor tube located in a tube furnace. The specimen is positioned in the center of the furnace and the tube is purged with argon. The heater attached to one of the contacting electrodes is powered to obtain a desired temperature difference across the length of the element (30 C minimum was found to be most reliable). The temperature difference is read by taking separate readings at either end of the specimen. After an initial room-temperature reading is taken, the tube furnace is powered and the temperature slowly increased. The two specimen temperatures and the output voltage of the specimen are plotted as a function of time by means of a temperature (or millivolt) recorder. The curves obtained by joining the respective points are used to obtain the temperature difference and corresponding output voltage at selected points in time.

Elevated-Temperature-Resistivity Test
Apparatus

The apparatus used for measuring resistivity as a function of temperature is similar in design to the Seebeck coefficient apparatus, the major exception being that an electrode heater is not used and only one thermocouple is used to measure temperature. The electrical system is shown schematically in Figure 9. The electrodes which support the specimen in the resistivity apparatus are used to carry current which is passed through the specimen. The apparatus incorporates a voltage-probe collar assembly which is fitted over the specimen before it is inserted between the electrodes. This probe collar and its electrical leads are shown in Figure 10.

The probe collar consists of two circular rings, each of which contain three equally spaced, radially positioned probe screws. The rings are fastened parallel to one another at a fixed distance by insulating spacers. The specimen is positioned centrally in the collars and is held firmly by the six probe screws. The electrical leads attached to the collars are used to measure the average voltage drop between the two sets of probe screws.

During operation, a 100-cycle alternating current of approximately 0.7 ampere is passed through the specimen and measured on a 1-ampere-range precision meter. The voltage drop between the probes is measured with a Ballantine a-c vacuum-tube voltmeter. Current and voltage readings are taken as the temperature of the specimen
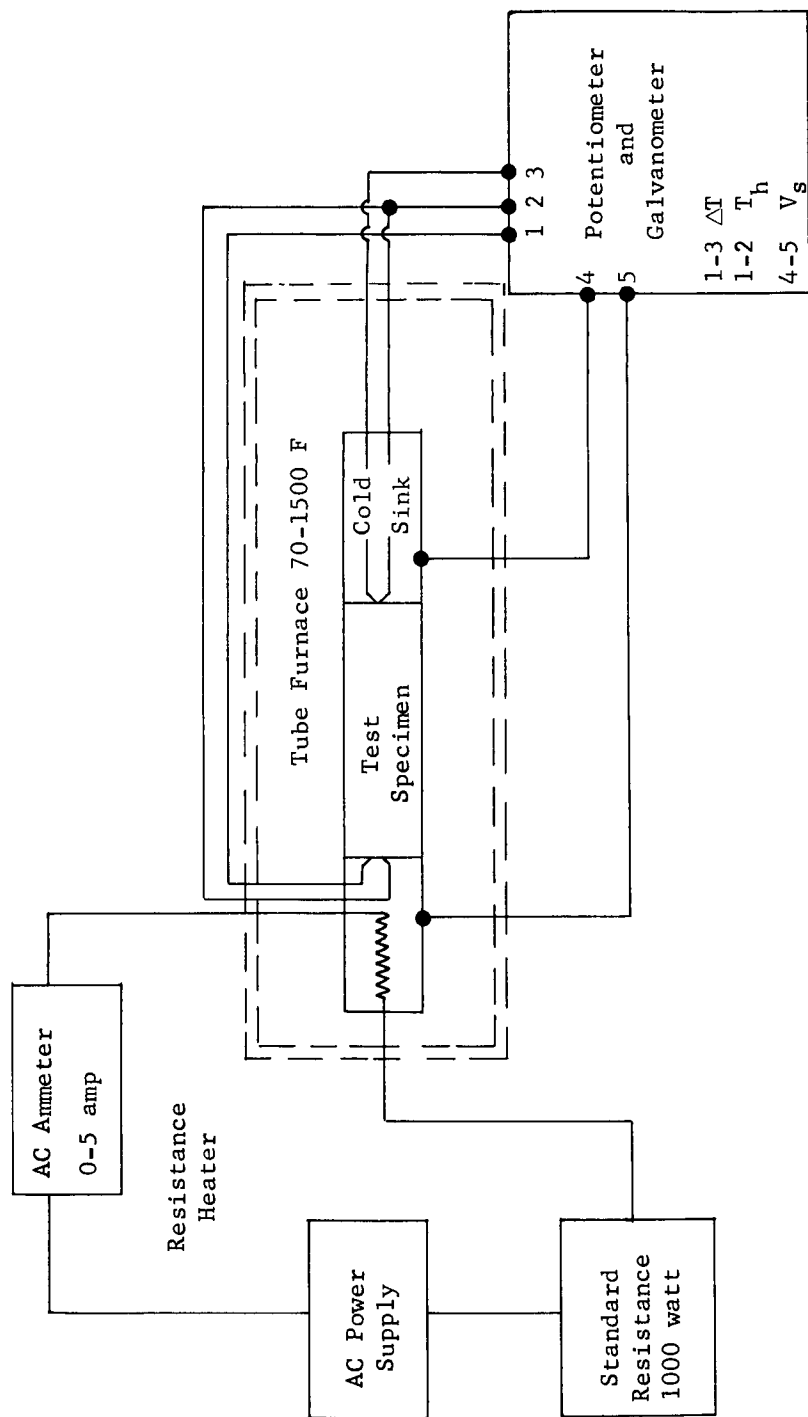
FIGURE 7. SCHEMATIC FOR ELEVATED-TEMPERATURE SEEBECK-COEFFICIENT-MEASURING APPARATUS
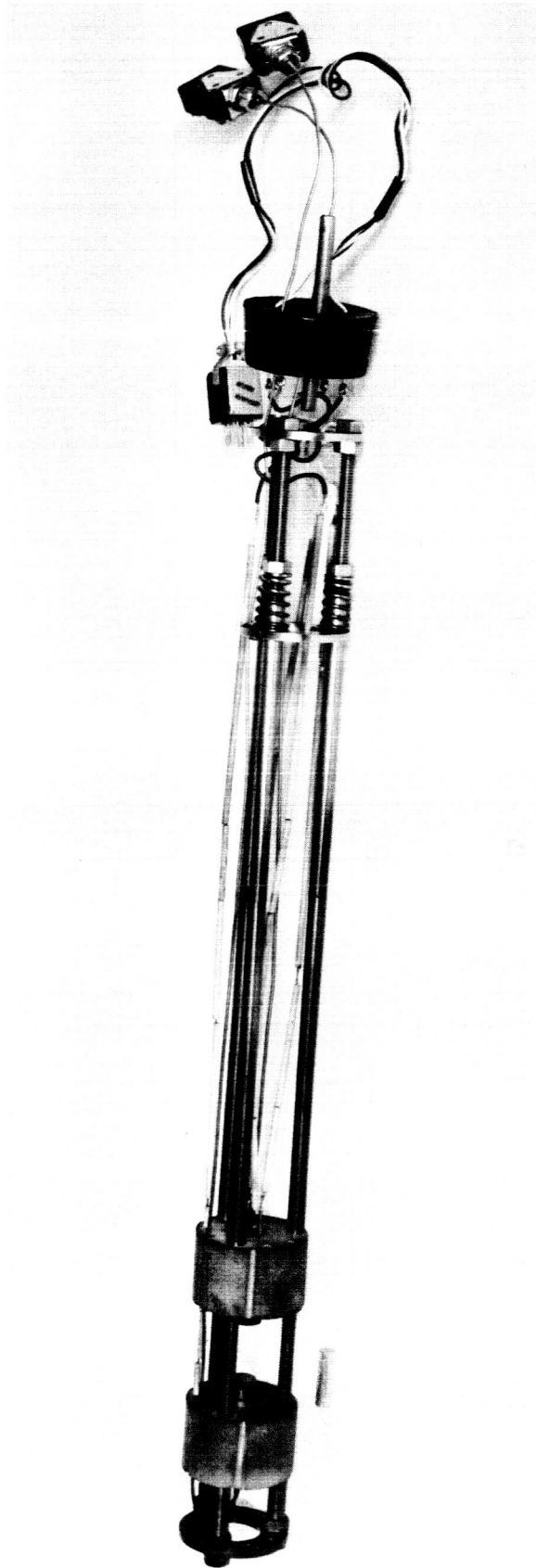
18803

FIGURE 8. DEVICE FOR MEASURING SEEBECK COEFFICIENT
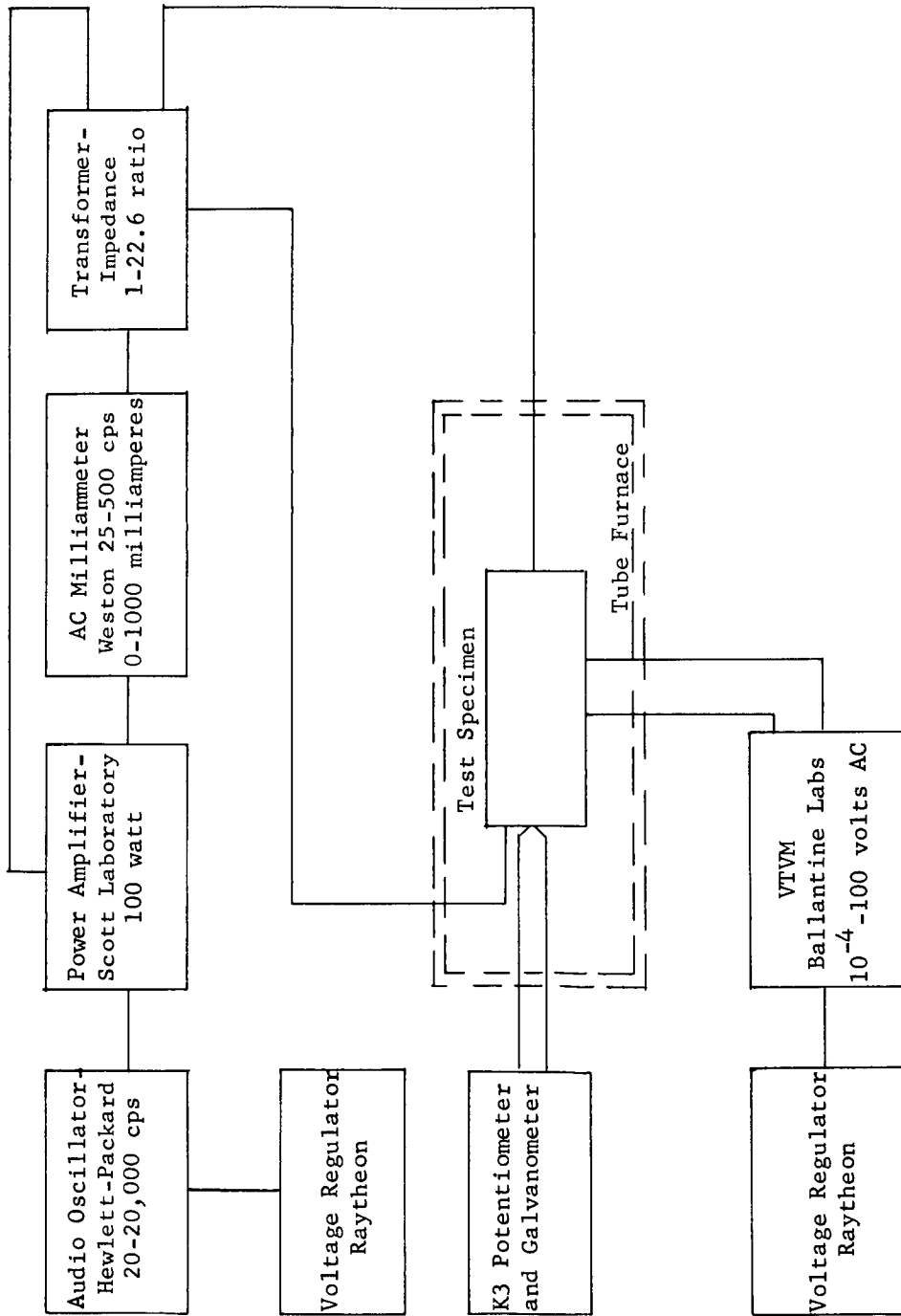
FIGURE 9. SCHEMATIC FOR ELEVATED-TEMPERATURE-RESISTIVITY MEASURING APPARATUS
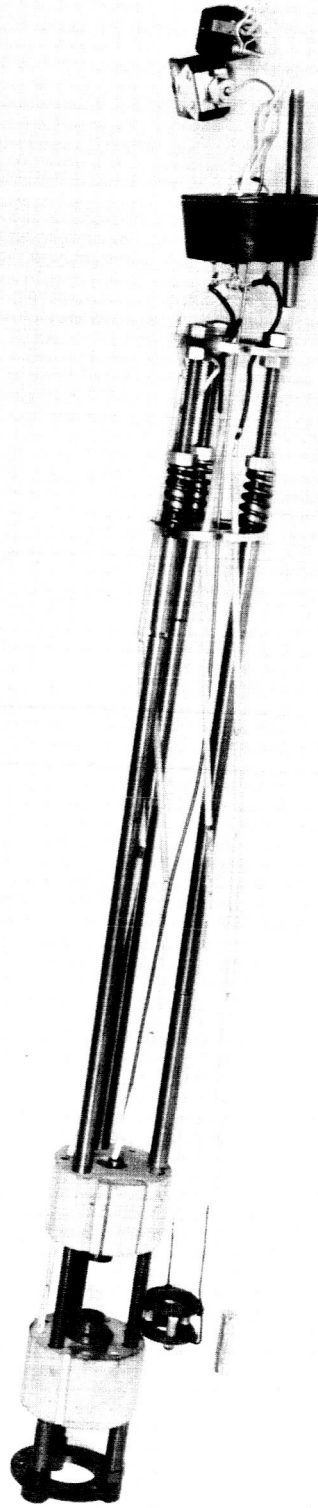
FIGURE 10. DEVICE FOR MEASURING ELEVATED-TEMPERATURE RESISTIVITY

18801

is increased gradually from room temperature to the maximum desired temperature. Heating is performed with the apparatus contained in an argon-filled Vycor tube positioned in a tube furnace.

The resistivity is calculated, using the relationship $\rho = R\dfrac{A}{L} = \dfrac{VA}{IL}$, where ρ is the resistivity in ohm-cm, V is the measured voltage drop, I is the measured current (in amperes) passed through the specimen, L is the distance in centimeters over which the voltage drop is determined (distance between probe collars), and A is the area of the specimen cross section in square centimeters. The values obtained are plotted as a function of the temperature at which the readings were taken.

Test Specimen Preparation and Test Results

Lead Telluride. The lead telluride used in this program was procured in powder form from Minnesota Mining and Manufacturing Company. Three formulations of lead telluride were used, conforming to the standard designations Tegs 2p, Tegs 2n, and Tegs 3p. The Tegs 3p-PbTe was considered a supplement to the other two types and was selected because of its reportedly greater durability, a characteristic which could make it a potential replacement for the Tegs 2p-type material.

The hot-isostatic-pressing process was selected for the fabrication of the PbTe-Fe composite of the segmented element. Consequently, the specimens used for electrical-property measurements were processed in this manner. The basis for the selection of the hot-isostatic process is discussed in a later section of the report.

Test-Specimen Preparation Procedure

The specimens for electrical-property measurements were prepared from minus 100-mesh powder according to the following procedure.

(1) The powder was loaded into a tubular rubber mold, evacuated, and then hydrostatically pressed at room temperature to produce a rod-like green body approximately 1/4 inch in diameter.

(2) The green-pressed PbTe was encased in a mica sleeve and an outer stainless steel container. Mica has been found to be a satisfactory encasing material having no effect on the electrical properties.

(3) The specimen can was sealed in an electron-beam welder, resulting in a vacuum within the can.

(4) The canned specimen was consolidated further by hot-isostatic pressing for 1 hour at 2500 psi. Two hot-isostatic-pressing temperatures were selected to represent the higher and lower pressing temperatures considered applicable for PbTe-SiGe segmenting. The two temperatures were 1200 F and 900 F.

(5) The specimens were decanned as the final step in their fabrication.

Test Results. The Seebeck coefficient and resistivity curves resulting from the tests are presented in Figures 11 through 13. All three PbTe materials fabricated at 1200 F were characterized, while the Tegs 3p PbTe fabricated at 900 F was excluded from characterization. The much lower power-producing capability (based on power-factor calculation of the specimen pressed at 1200 F) and the observed poor shoe-bonding characteristic of the Tegs 3p material provided the basis for subsequent exclusion of this material from the study.

The average properties of each material are listed in Table 1. The averages were determined over the operating range of 150 C and 500 C. The Seebeck coefficients, resistivities, and calculated power factors are compared. Lead telluride elements of the pressed and sintered type which were purchased from 3M Company were used for reference purposes. Their measured electrical properties are included in Table 1 for comparison.

The power factors for both the Tegs 2p- and 2n-type PbTe specimens pressed at 1200 F were greater than those for the reference elements. The differences are mainly attributable to the higher Seebeck coefficients of the materials pressed at 1200 F. The power factors for both the p- and n-type specimens pressed at 900 F are lower than those for the reference elements. The lower values result from a lower Seebeck coefficient for the n-type PbTe and a higher resistivity for the p-type PbTe. Since the power factors for the Tegs 2-type PbTe pressed at 900 and 1200 F were greater than 90 percent of the power factors for the reference elements, the properties were accepted for couple calculations. The pressing temperature used will depend on the results of the couple-fabrication development.

The power factor for the hot-pressed Tegs 3p PbTe compared favorably with that for the reference elements. However, the values were so much lower than the Tegs 2p PbTe values that further consideration of the Tegs 3p PbTe was eliminated. The poor results obtained in attempts to join this material to iron by an established technique strengthened the decision to exclude the Tegs 3p PbTe from further study.

Silicon Germanium. Silicon germanium was procured from Radio Corporation of America (RCA) in raw ingot form. The 1/4-inch-diameter specimens for property measurements were obtained by abrasive cutting and grinding. No difficulties were encountered in this operation.

The properties were measured and the data compared with the data supplied by RCA for the specific materials purchased. The average values of Seebeck coefficient and resistivity calculated between 500 and 900 C were compared. The average values of resistivity differed by less than 10 percent, as is apparent from the data shown below.

	Average Resistivity of SiGe (500-900 C), ohm-cm	
	n-Type	p-Type
RCA Data	2.89	1.98
Battelle Measurements	3.04	1.89
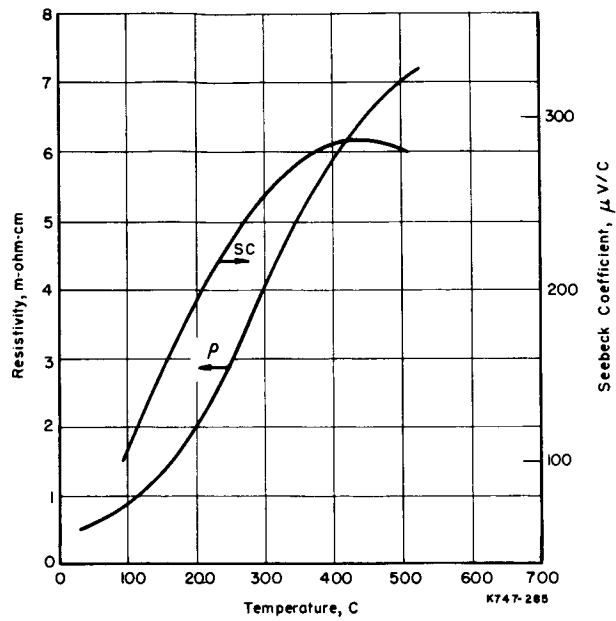
a. At 1200
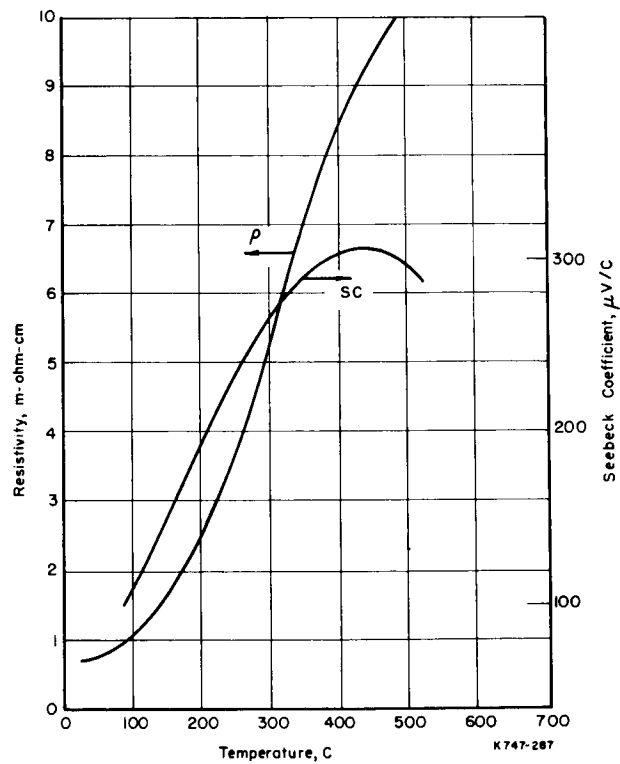
b. At 900 F

FIGURE 11.   ELECTRICAL PROPERTIES OF TEGS 2P PbTe HOT
ISOSTATICALLY PRESSED AT 1200 F
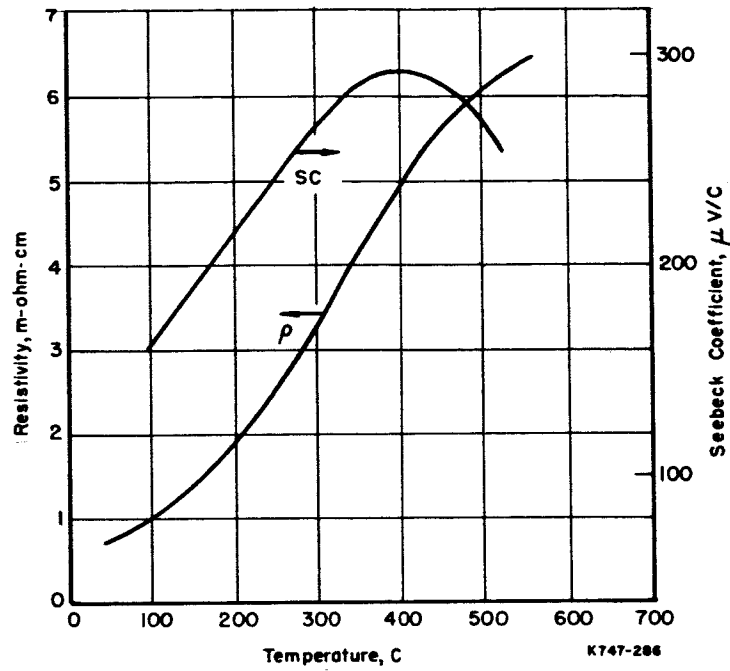
a. At 1200 F
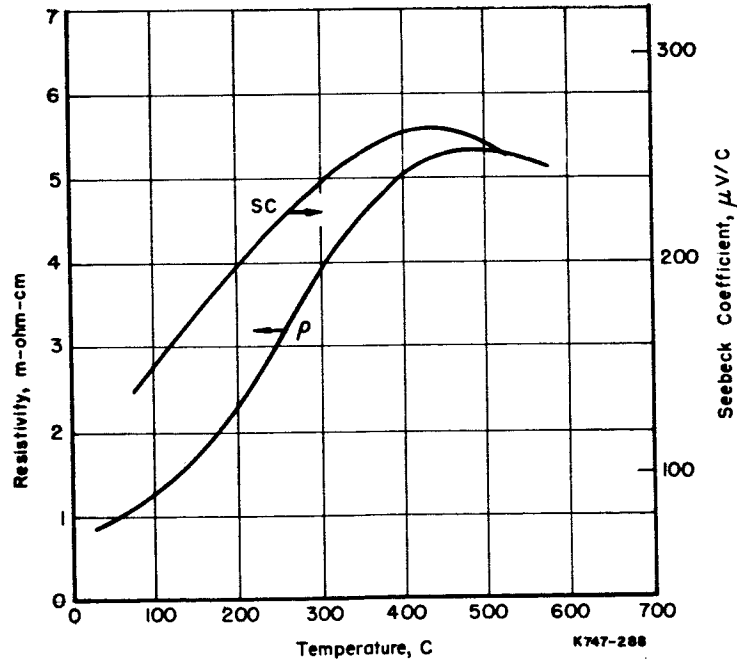
b. At 900 F

FIGURE 12. ELECTRICAL PROPERTIES OF TEGS 2N PbTe
HOT ISOSTATICALLY PRESSED AT 1200 F

BATTELLE MEMORIAL INSTITUTE
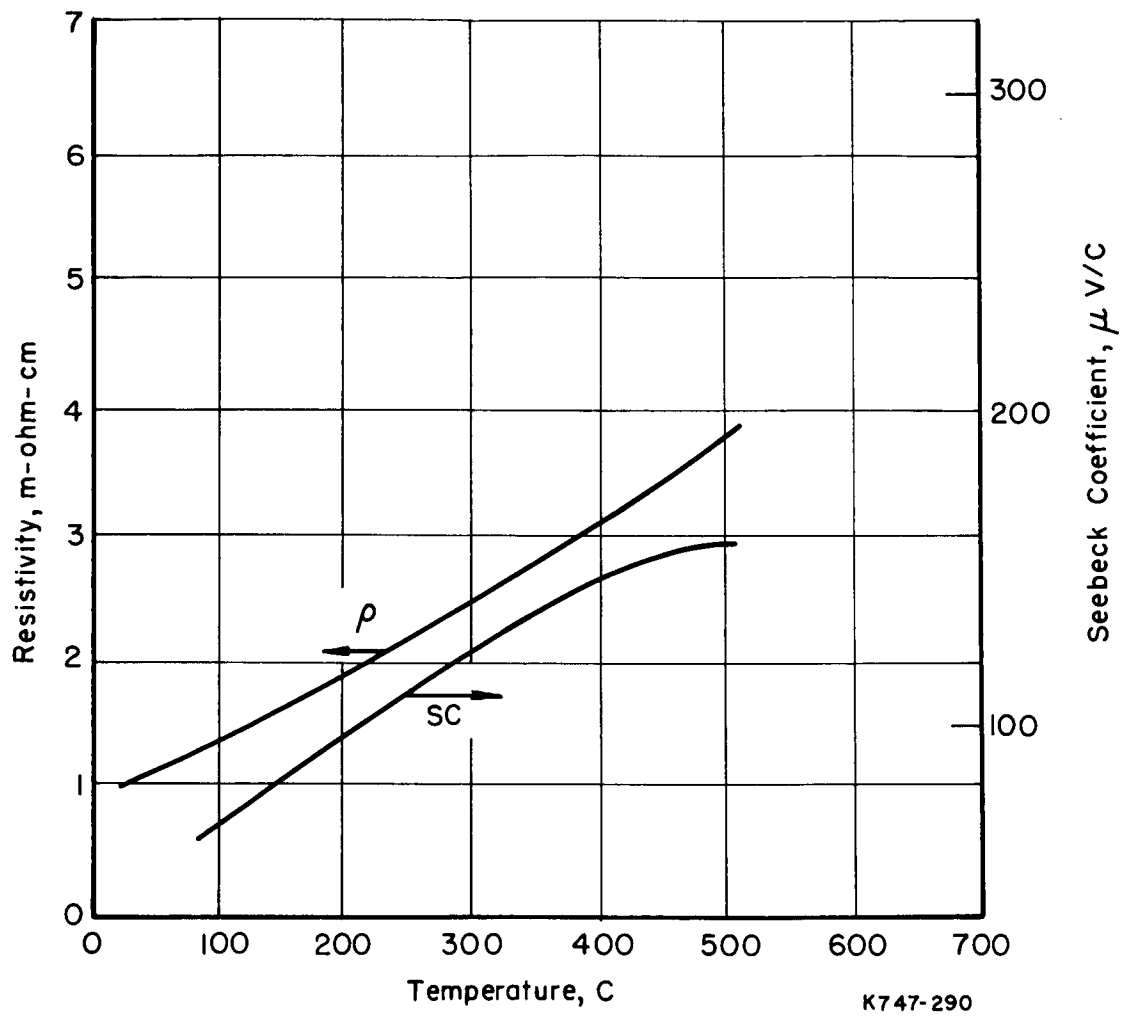
FIGURE 13. ELECTRICAL PROPERTIES OF TEGS 3P PbTe HOT
ISOSTATICALLY PRESSED AT 1200 F

TABLE 1. ELECTRICAL PROPERTIES OF PbTe ELEMENTS

Average Values Between 150 and 500 C

Type of Element	Seebeck Coefficient, $\mu v/C$	Resistivity, $\mu ohm-cm$	Power Factor (S^2/ρ), $10^{-6}\left(\dfrac{V}{C}\right)^2/ohm-cm$
Elements Hot Isostatically Pressed at 1200 F			
Tegs 2p	247	4175	14.6
Tegs 2n	258	3750	17.8
Tegs 3p	125	2650	5.9
Elements Hot Isostatically Pressed at 900 F			
Tegs 2p	261	5975	11.4
Tegs 2n	235	3920	14.1
3M Elements Measured by Battelle			
Tegs 2p	225	4175	12.1
Tegs 2n	248	4030	15.3
Tegs 3p	137	2990	6.4

Difficulties were encountered, however, in obtaining reproducible values of Seebeck coefficient. The variability in test results appeared to be the result of random variations in the thermal conduction at the thermocouple contacts. Data were obtained which matched the RCA data over most of the temperature range. At high temperatures, however, the Battelle data tended to deviate, sometimes at abnormal rates, indicating error in the measurement.

On the basis of the correspondence of Seebeck coefficient values over the lower range of temperatures and the good correspondence of the resistivity values over the entire range, the RCA data were selected for use in couple calculations. The electrical-property curves for the SiGe materials are given in Figures 14 and 15. The average values of the Seebeck coefficients over the temperature range 500 to 900 C are given below.

Average Seebeck Coefficient of SiGe
(500-900 C), μV/C

	n-Type	p-Type
RCA Data	290	234

Transition-Member Bonding Studies

The greatly differing thermal-expansion rates of SiGe and PbTe [2 and 10 μ in. / (in.) (F), respectively] dictate the need for an intermediate transition member to accomplish joining to these two thermoelectric-element segments. On the basis of the state-of-the-art technology, tungsten can be joined to SiGe, and iron (powder product) to PbTe, for service as shoes. The problem of joining SiGe and PbTe segments thus reduces to one of joining tungsten to iron while the process limitations of the thermoelectric materials and bonding to their respective shoe materials are imposed. The maximum temperature for processing PbTe is in the vicinity of 1500 F, at which point PbTe becomes very plastic. The SiGe-W bonds formed by a direct reaction process are limited to operating temperatures below about 1000 F. If exceeded, continued reaction with tungsten occurs which results in cracking of the SiGe. This is assumed to be the result of the reaction product having a specific volume widely differing from that of its makeup constituents.

The aim in this study is to explore several bonding combinations to arrive at one which is compatible with an element fabrication schedule. The use of temperatures higher than 1000 F was predicted on schemes which involve either, (1) reacting the tungsten and SiGe after forming the transition member or, (2) using a braze-bonded SiGe tungsten composite which would withstand the high temperatures of subsequent pressure bonding to the transition member.

Two basic approaches considered for joining iron and tungsten to form a transition member utilized nickel as a solid state bonding agent as depicted in Figure 16. In both cases although temperatures of 1200 and 1400 F and pressures of 2500 and 10,000 psi were used in bonding trials, only the higher temperature and pressure combination was found to produce adequate bonds.
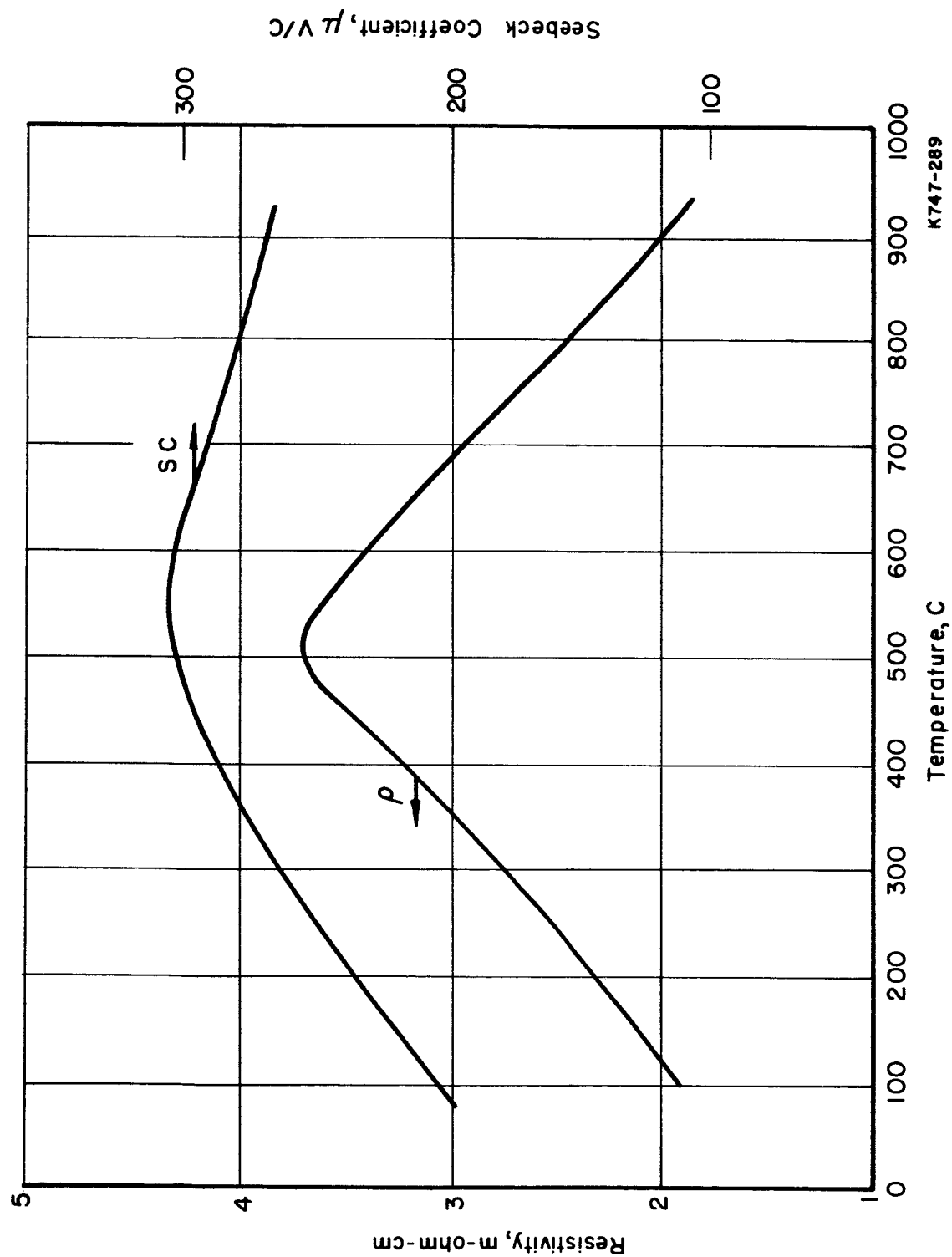
FIGURE 14. ELECTRICAL PROPERTIES OF n-TYPE SiGe INGOT STOCK
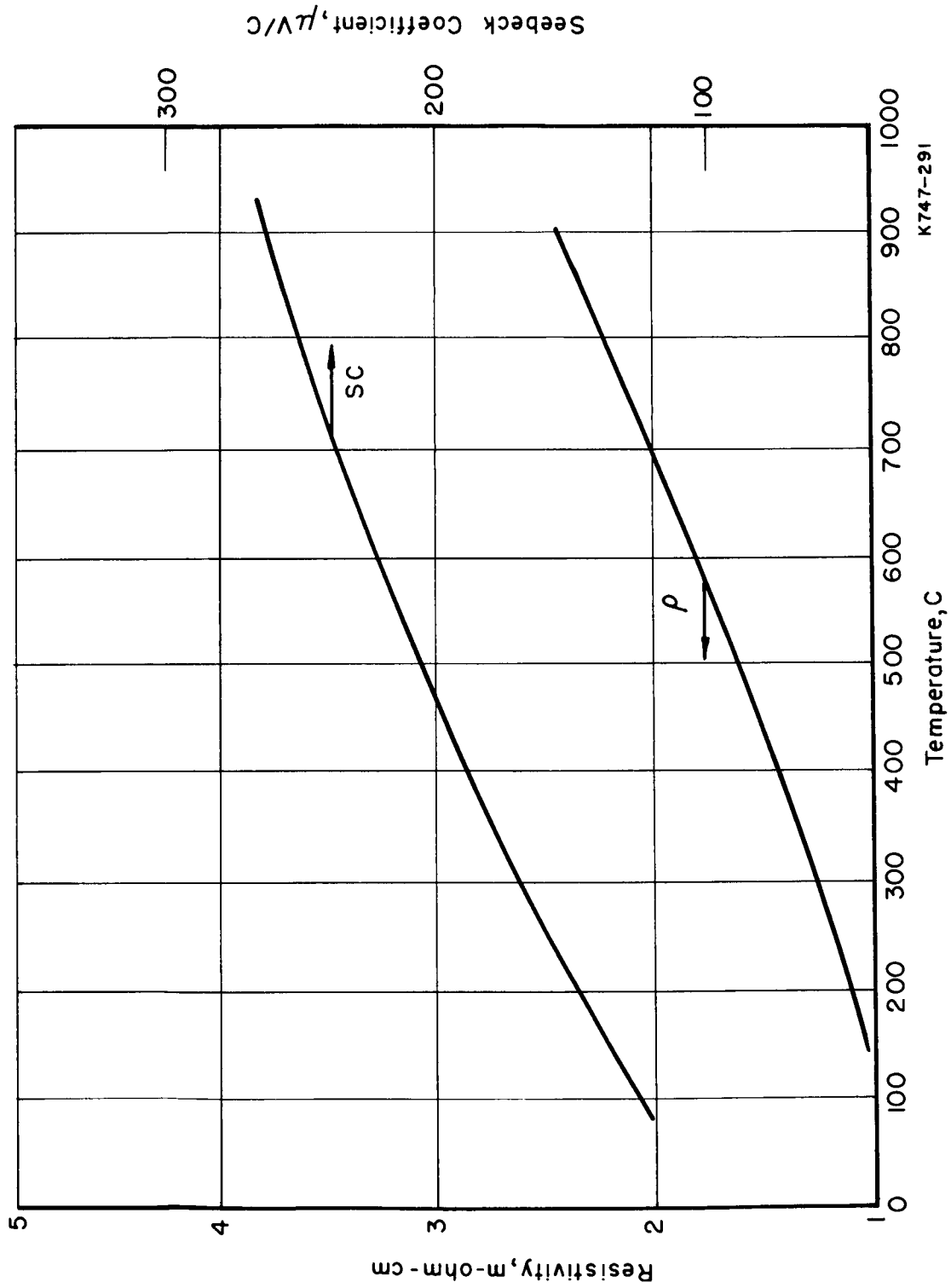
FIGURE 15. ELECTRICAL PROPERTIES OF p-TYPE SiGe INGOT STOCK

K747-291
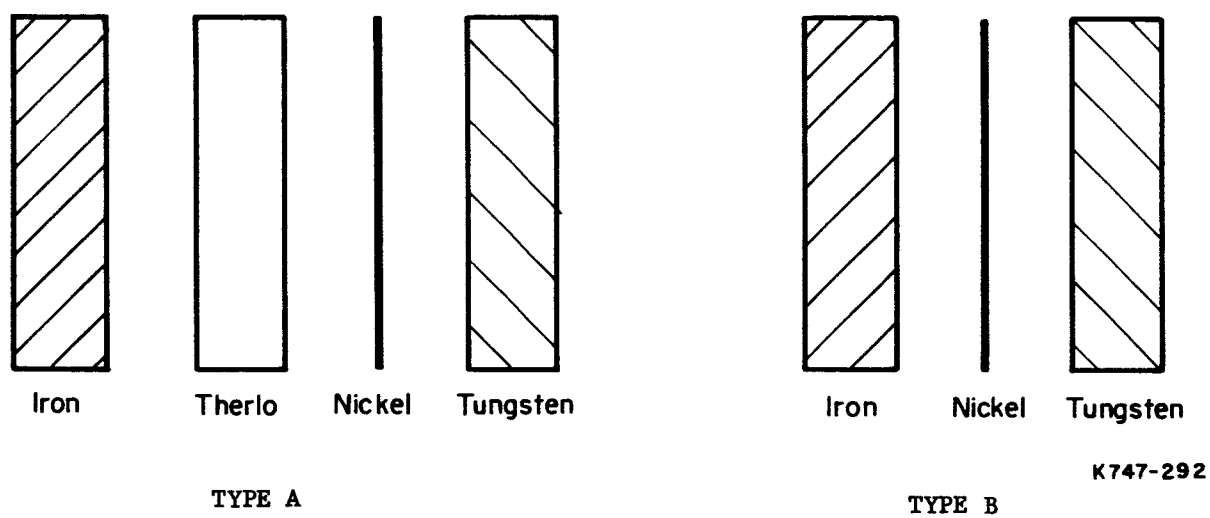
FIGURE 16. BASIC APPROACHES TO TRANSITION-MEMBER JOINING

The first materials system shown in Type A of Figure 10 incorporates an alloy layer (Therlo) with an expansion rate between those of the iron and tungsten members (2.5 vs 3.3 vs 6.3 μ in./in. F). This combinations of materials was devised to provide a gradual transition in expansion rate and reduce the deleterious stresses at the bond resulting from differential expansion at elevated temperatures.

The prime difficulty with the material combination of Type A occurred at the Therlo-nickel-tungsten bond. Although bonding of the constituents was achieved, the Therlo-to-nickel bonds separated as shown in Figure 17. A nickel diffusion zone, although not clearly apparent in the photomicrograph, existed in the surface of the Therlo, giving evidence of initial bonding. The area photographed was selected to show where the nickel remained bonded to the Therlo and was torn free from the parent material. The failure was attributed to a weak bond between the nickel and Therlo and the relatively high strength of the differentially contracting tungsten and Therlo members.

Satisfactory bonds were obtained between iron and the Therlo member without the use of a bonding agent as is shown in Figure 18. The success with the iron-to-tungsten bonds in Type A is attributed to the relatively low strength of the pure-iron-powder product.

The second materials system considered for achieving transition bonds from iron to tungsten incorporated nickel as the sole bonding agent, as shown by Type B of Figure 16. Although this combination of materials did not provide the gradual transition in expansion rate as in Type A, it was found to be more suitable for fabrication.

Bonding of iron to tungsten with nickel, when attempted at 1200 F, was entirely unsuccessful. The quality of bonds produced with a lower pressure of 2500 psi at 1400 F was mechanically poor. The bonding was spotty, leading to separation under a light force. Bonds of this type failed completely during three cycles when subjected to thermal cycling from room temperature to 950 F.

Suitable transition members of this system were achieved when bonding was attempted at 1400 F and 10,000 psi. As shown in Figure 19, sound bonds were obtained by incorporating nickel as a plated coating on the tungsten. Similar bonds were also obtained with the nickel applied in the form of 1-mil-thick foil. The latter is preferred because of the variability found in the quality of nickel plates on tungsten. Laminated nickel plate was found to remain completely unbonded during the pressure-bonding cycle.

In summary, the iron-nickel-tungsten Type B combination appeared to provide a sound transition member, when fabricated at 1400 F and 10,000 psi.

250X   Etched   23220
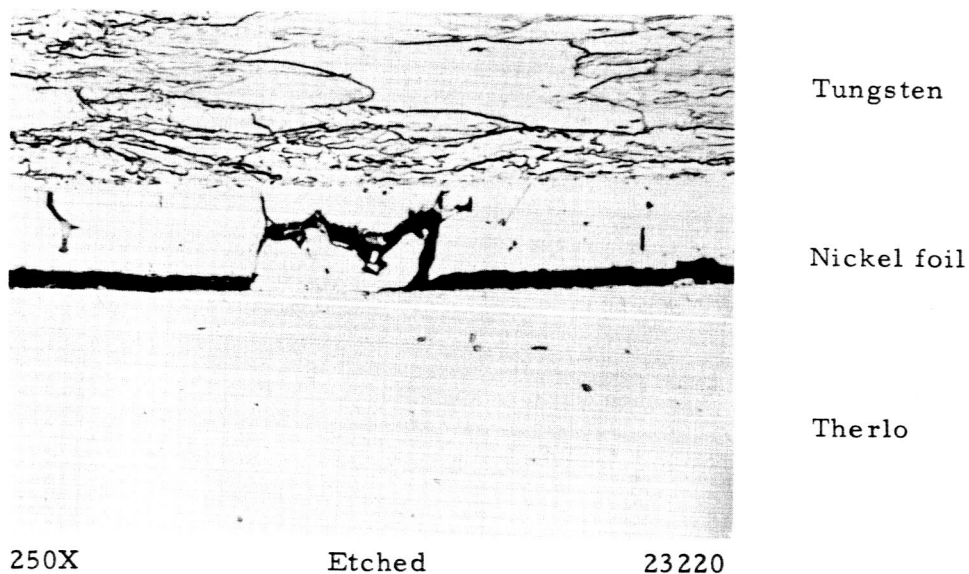
FIGURE 17. TUNGSTEN-NICKEL-THERLO ALLOY BONDS FORMED BY HOT
ISOSTATIC PRESSING AT 1400 F, 10,000 PSI

250X   Etched   23022
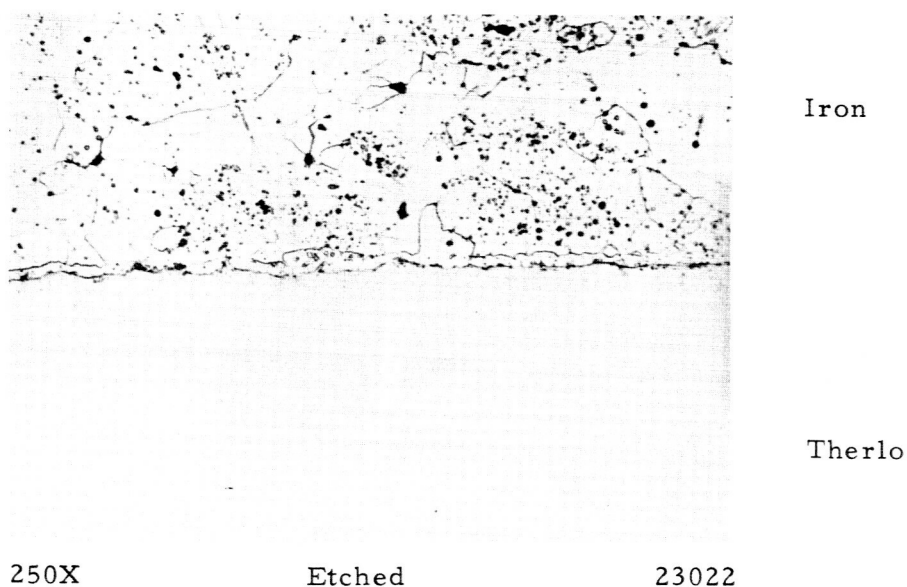
FIGURE 18. IRON-THERLO BOND FORMED BY HOT ISOSTATIC
PRESSING AT 1400 F, 10,000 PSI

Tungsten

Nickel plate
on tungsten

Iron

250X   As Polished   23023
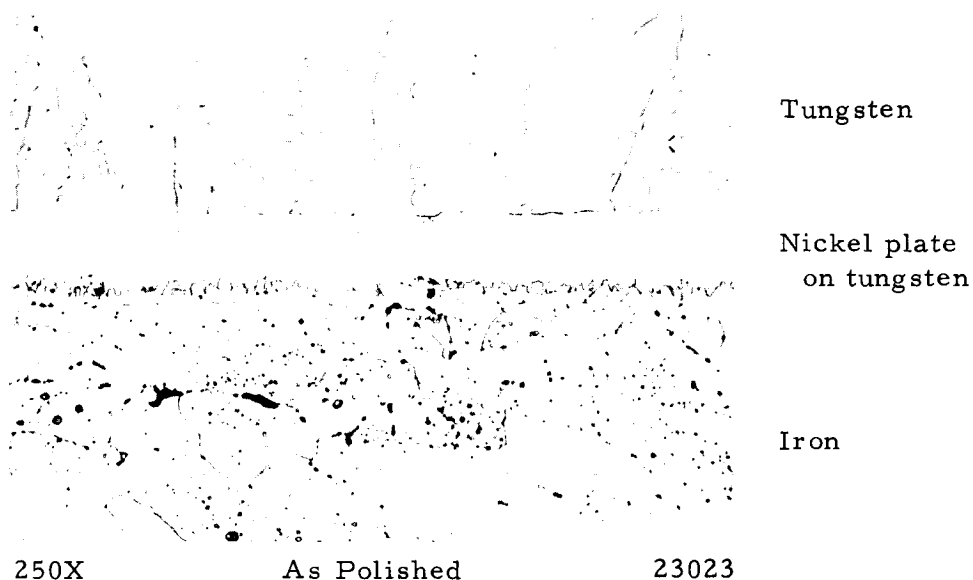
FIGURE 19.   IRON-NICKEL-TUNGSTEN BOND FORMED BY HOT ISOSTATIC
             PRESSING AT 1400 F, 10,000 PSI

Tungsten-SiGe Bonding Studies

Since the state-of-the-art bond between tungsten and SiGe has a temperature limitations of about 1000 F, several approaches were explored to produce this junction. They involve bonding during total element fabrication or by an alternative route where this junction is made prior to incorporating the SiGe segment in the element. The approaches evaluated follow three primary paths as outlined below.

(1) Production of the tungsten-SiGe bond at a relatively high temperature (1400 F) by direct reaction or braze bonding under the pressure conditions of the hot-isostatic-pressing process. The segmented element would be produced completely in this one-step operation. The time of bonding might be sufficiently short to prevent damage to the SiGe by reaction with the tungsten.

(2) Join the SiGe segment to the tungsten member of the prefabricated PbTe segment by means of a low-temperature (less than 1000 F) eutectic braze which might be accomplished with gold. Gold forms eutectics with both silicon and germanium at temperatures near 700 F which is below the normal operating temperature (about 975 F) of this junction.

(3) Produce a braze bonded tungsten-SiGe composite which will survive subsequent pressure bonding at temperatures of about 1000 F.

The information relating to these three areas of investigation is discussed below.

Tungsten to SiGe Joining During Pressure Bonding

Attempts to produce a direct reaction bond at the conditions which are considered the maximum applicable for segmenting, namely 1400 F and 10,000 psi, were completely unsuccessful. In no instance was there any signs of reaction or adherance of the members. Although the hot-isostatic-pressing container is evacuated prior to use, the atmosphere within is apparently insufficiently clean to maintain the necessary cleanliness of the bonding surfaces. The mica used for element encasements is a flake-type product which is a prime source of occluded gases.

Similar attempts made under the same conditions with gold as an eutectic-forming braze were also unsuccessful. This approach was pursued no further.

Low-Temperature Gold Braze. The use of gold as a braze agent for joining the tungsten to SiGe was first considered as a possible means of accomplishing the bond at a temperature below 1000 F. The gold-silicon or gold-germanium eutectic reactions which occur at about 700 F might possibly be utilized in producing bonds, in place, during normal operation of the couple or in a separate brazing operation. Either approach could then be used to join the SiGe segment to a prefabricated PbTe segment which has the transition member attached.

Attempts to effect such a bond at 1000 F in either argon or hydrogen atmospheres were unsuccessful. Reaction between the gold (in the form of foil) and SiGe occurred only spottily at apparent localized points of pressure contacting, causing small holes to be formed in the gold foil. The inability to react the member was attributed to the presence of a thin film of silicon dioxide (SiO_2) on the surface of the SiGe.

Several attempts were then made to effect the braze with the aid of fluxing agents. Although the temperature was low for titanium hydride it was used in a thin slurry over the SiGe surface for the purpose of providing at least a small source of nascent hydrogen for oxide reduction. No improvement was achieved. The use of ammonium bifluoride at the bond surface as a source of HF and F_2, which are effective reactants with SiO_2, produced partial successes on a random basis. The best result involved effective brazing of about one-third of the surface of an 0.3-inch-diameter specimen.

This approach was pursued no further.

High-Temperature Braze. With the lack of success in evolving a low-temperature brazing schedule with gold as the braze material, the temperatures required to effect a braze in argon and vacuum were determined. Sound brazes were produced in both argon at 2000 F and in vacuum as low as 1475 F. Vacuum was selected for use in preparing test specimens to take advantage of lower temperatures, however, a braze temperature of 1800 F was found to be more reliable in making reproducible brazes. Figure 20 shows a photomicrograph of the gold-brazed tungsten-SiGe composite.

The gold-brazed composite was evaluated for its compatibility with a high-temperature element fabrication schedule by processing specimens through a typical 1400 F pressure-bonding cycle of 1 hour's duration. This treatment caused complete

separation of the tungsten shoes. The separation occurred at the bond interface with no tear-out of SiGe, indicating a weak bond to the tungsten. The gold was then re-placed by a gold-nickel alloy braze to improve the potential for bonding to the tung-sten with the addition of nickel. The as-brazed bonds were equal in quality to those obtained with gold, but were more serviceable. The suitability of this type of bond was evaluated by means of a 1-hour furnace treatment at 1400 F. Satisfactory re-sults were obtained in this case. Figure 21 shows a photomicrograph of the braze area after the additional thermal treatment. The bond area consists of a uniform, homogenized band of reaction product. No cracks were apparent in the SiGe.

Lead Telluride Segment Fabrication and Evaluation

The lead telluride segment in this study consists of the thermoelectric material with shoes attached at either end. The hot-isostatic-pressing process was selected for fabrication of this segment, its selection being based on the following considerations.

(1) The process as applied by Battelle has been shown to be capable of producing PbTe thermoelements of good quality from powder starting materials.

(2) The process is effective in producing strong and well-bonded element-shoe composites from all powder starting materials.

(3) The range of processing temperatures over which PbTe elements can be fabricated is greater than for any other process. Applica-bility over the range 750 F to 1400 F has been demonstrated.

(4) The above-listed features can be combined with an effective pressure-bonding capability useful for joining other members of a segmented element.

(5) The process is not as restricted by l/d ratio limitations as are some fabrication processes such as hot die pressing.

Segment Preparation

The materials of the PbTe segment were incorporated entirely in powder form. The PbTe was -100 mesh and iron as the reference shoe material was -200 +270 mesh. A second shoe material was studied and is discussed later in the report.

The segment composite was prepared for hot isostatic pressing by first pre-paring a green-pressed body. The shoes were firmly attached to the PbTe in the green form by layering the powders in the die and pressing them together. A low pressure, approximately 10,000 psi, was used to form each layer in the die before the next layer was put atop the previous one. The final pressing was performed at 100,000 psi. Sufficient interlocking of the iron and PbTe powders occurs to make a strong mechanical bond. The green-pressed segment was slipped into a preformed mica sleeve and then encased in an evacuated thin-wall stainless steel container for hot isostatic pressing.
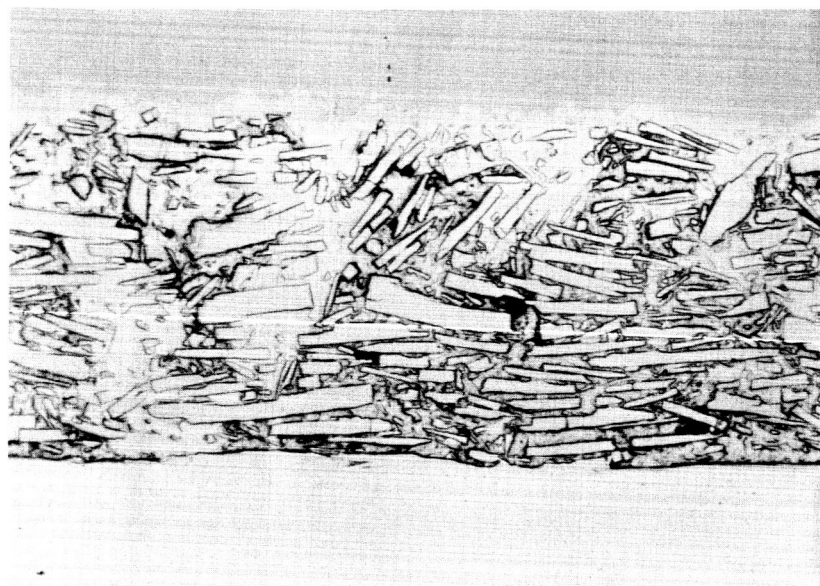
250X   23363

FIGURE 20.   GOLD-BRAZE BOND OF TUNGSTEN TO
             SiGe MADE IN VACUUM AT 1475 F
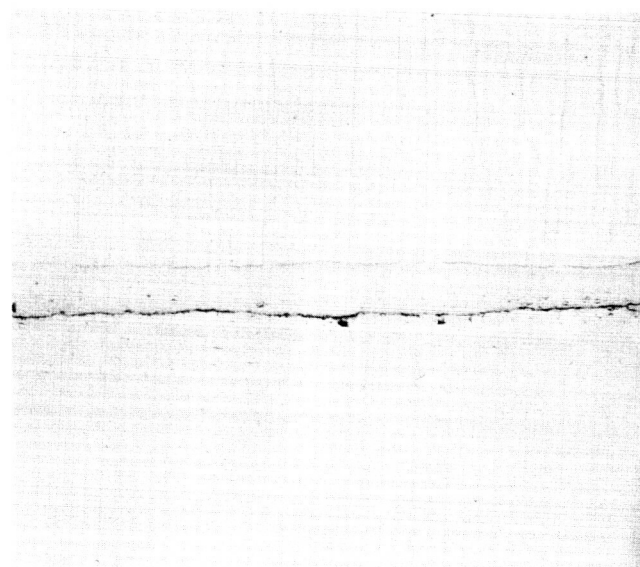
100X   25198

FIGURE 21. GOLD-NICKEL ALLOY BRAZE OF TUNGSTEN TO
           SiGe PERFORMED AT 1800 F IN VACUUM

Specimen was thermally aged 1 hour at 1400 F.

A round-shaped element was initially selected for development, but later a square shape was used to achieve better deformation characteristics. During pressing, the element container collapses onto the specimen and, as a result of the initial clearances and reduction in thickness of the element and mica sleeve, the can attempts to reduce in perimeter. In the case of the round can, wrinkles form in the surface which are roughly duplicated in the element surface. This was considered objectionable because of the variation in cross section which occurs randomly along the element. In addition, the can tends to bend and can conceivably cause breaking of the specimen. In the case of the square container, the deformation is quite uniform with the excess can material moving to the corners causing them to sharpen. The sides of the square element develop a gentle concave shape which has not been found objectionable.

Segment-Material Characteristics

The structural condition of the hot-pressed PbTe segments was examined to determine the effects of the pressing temperature. The two temperatures of prime interest were 900 F and 1400 F. Metallographic specimens were studied in the as-polished condition under bright-field illumination with particular attention given to density, shoe-element reaction products, and cracking.

Both the p- and n-types of PbTe are effectively consolidated to a high density at 900 F and 2500-psi pressure. Representative photomicrographs are shown in Figures 22 and 23. After pressing at 1400 F and 2500 psi, the p-type PbTe contains a considerable amount of porosity as exemplified in Figure 24. The porosity in the p-type PbTe pressed at 1200 F is similar but is not as great. Although the porosity in p-type PbTe pressed at 1400 F is quite extensive, it has no apparent effect on the electrical properties, this conclusion being based on the property characterizations presented in an earlier section.

The porosity is attributed to entrapped gas from the green-pressing operation and possibly volatile surface oxides. When pressed at 900 F, the PbTe is sufficiently strong to resist creep growth of the pores during the short period over which the pressure is released at the pressing temperature, thus producing a dense structure. In the case of the 1400 F pressing condition, the PbTe is so weak when the pressure is released at temperature that the high-pressure gas in the pores can cause the surrounding material to creep.

Evidence of this was found in p-type PbTe pressed at 900 F or lower which is subsequently aged for a prolonged time at a temperature of 950 to 1000 F. Significant porosity is generated, as exemplified by the specimen shown in Figure 25. In this case the porosity also had no apparent effect on element performance. The n-type PbTe exhibits similar behavior, but to a much smaller degree. The total void volume is smaller and the pores tends to coalesce at the grain boundaries.

The bonds between Tegs 2 PbTe and iron fabricated at both 1400 F and 900 F were examined metallographically. Reaction of the iron with the p-type PbTe was observed in specimens pressed at both temperatures. Figure 26 shows the reaction product present near the bond interface in a 1400 F specimen. The new phase is believed to be iron telluride. Microprobe analysis performed on a path across the interface shows localized concentrations of iron and tellurium in the PbTe near the

100X   As Polished   26103   100X   As Polished   26104

FIGURE 22.   p-TYPE PbTe FABRICATED   FIGURE 23.   n-TYPE PbTe FABRICATED
AT 900 F   AT 900 F
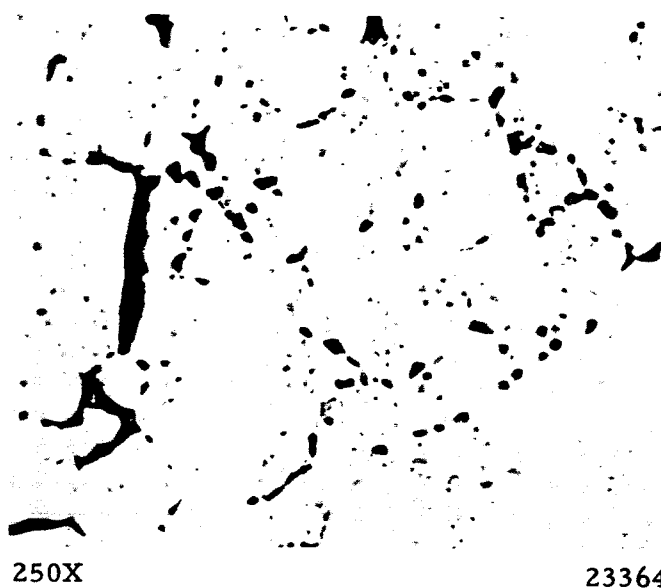
250X   23364

FIGURE 24.   STRUCTURE OF p-TYPE PbTe HOT
ISOSTATICALLY PRESSED AT 1400 F

250X   As Polished   25300
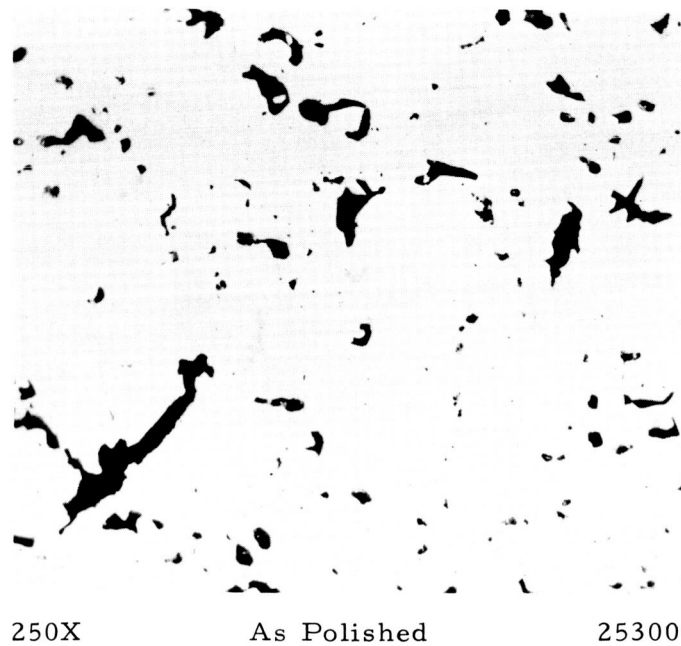
FIGURE 25.   STRUCTURE OF p-TYPE PbTe AFTER AGING AT 950 F

PbTe

Fe

250X   As Polished   23366
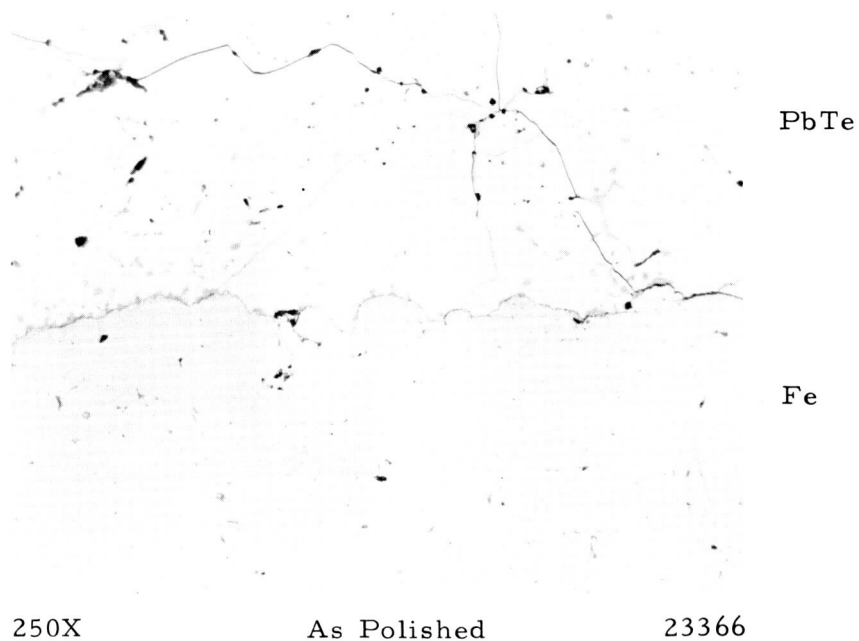
FIGURE 26.   IRON - 2p PbTe BOND PRODUCED AT 1400 F SHOWING
Fe - PbTe REACTION PRODUCTS AND CRACKING OF
PbTe

interface, with accompanying depletion of lead. The specimens pressed at 900 F show smaller amounts of the new phase, while n-type PbTe shows no evidence of such reaction at either temperature.

Because of the notably great propensity of p-type PbTe (Tegs 2) to crack under stress, the relative effects of pressing temperature and pressure on cracking were examined. Earlier experience by Battelle with hot isostatic pressing has shown that p-type PbTe can be overpressed at 900 F. A pressure of 10,000 psi causes internal stresses in the material making it extremely sensitive to cracking. Pressing was attempted at 10,000 psi and 1400 F, however, so that the higher temperature might allow the stresses to relax before the specimen was cooled. This was found not to be the case, and extensive cracking still occurred. With a pressing schedule involving 1 hour at 10,000 psi followed by 2 hours at 2000 psi to permit relief of the overpressing, the material showed improvement but cracks of the type shown in Figure 20 were prominent and the bulk material was abnormally sensitive to stress. In addition, the shoes were easily broken free from the elements. It is not known whether the cracks in the latter case actually resulted from overstressing or from the large temperature change and resulting differential expansion in cooling to room temperature.

A pressure of 2500 psi was established for pressing of p-type PbTe at all temperatures. N-type PbTe has shown no apparent sensitivity to pressing at pressures to 10,000 psi.

Element-Shoe Testing

The selection of iron as the shoe material for PbTe is based primarily on its accepted chemical compatibility and ability to be bonded to PbTe. To date, the major problem associated with iron results from its insufficiently high expansion rate. It is about 30 percent lower in expansion rate than PbTe, causing the PbTe to undergo tensile stressing upon cooling from the bonding or operating temperature. In the case of the very fragile p-type (Tegs 2) PbTe, cracking becomes a serious problem. The two considerations given to this problem with the p-type material were: (1) determination of the relative effects of pressing temperature on the presence of cracks, and (2) evaluation of a higher expansion rate, iron-base alloy as a possible replacement for iron.

The bonded specimens prepared for this study were evaluated by means of resistance traverse measurements made across the bond interfaces and the adjacent thermoelectric material. These measurements were made with the apparatus shown in Figure 27. In making the measurements, the specimen is held between contact electrodes while an a-c current of about 0.7 ampere is passed through. A calibrated screw drive mechanism is used to accurately locate a voltage probe at precise points along the specimen. The voltage drop between the probe and a fixed end electrode is measured at each probe location by means of a vacuum-tube voltmeter. The current is determined by measuring the voltage drop across a calibrated resistor. The measured voltage drops between the fixed and movable electrodes are plotted as a function of probe traversing distance. The increments of distance between probe locations in the vicinity of the bonds was 10 mils.

The curves obtained in the above manner are useful in determining the presence of cracks or discontinuities at or near the shoe-element bond interface. A crack, if

FIGURE 27. RESISTANCE-TRAVERSE APPARATUS
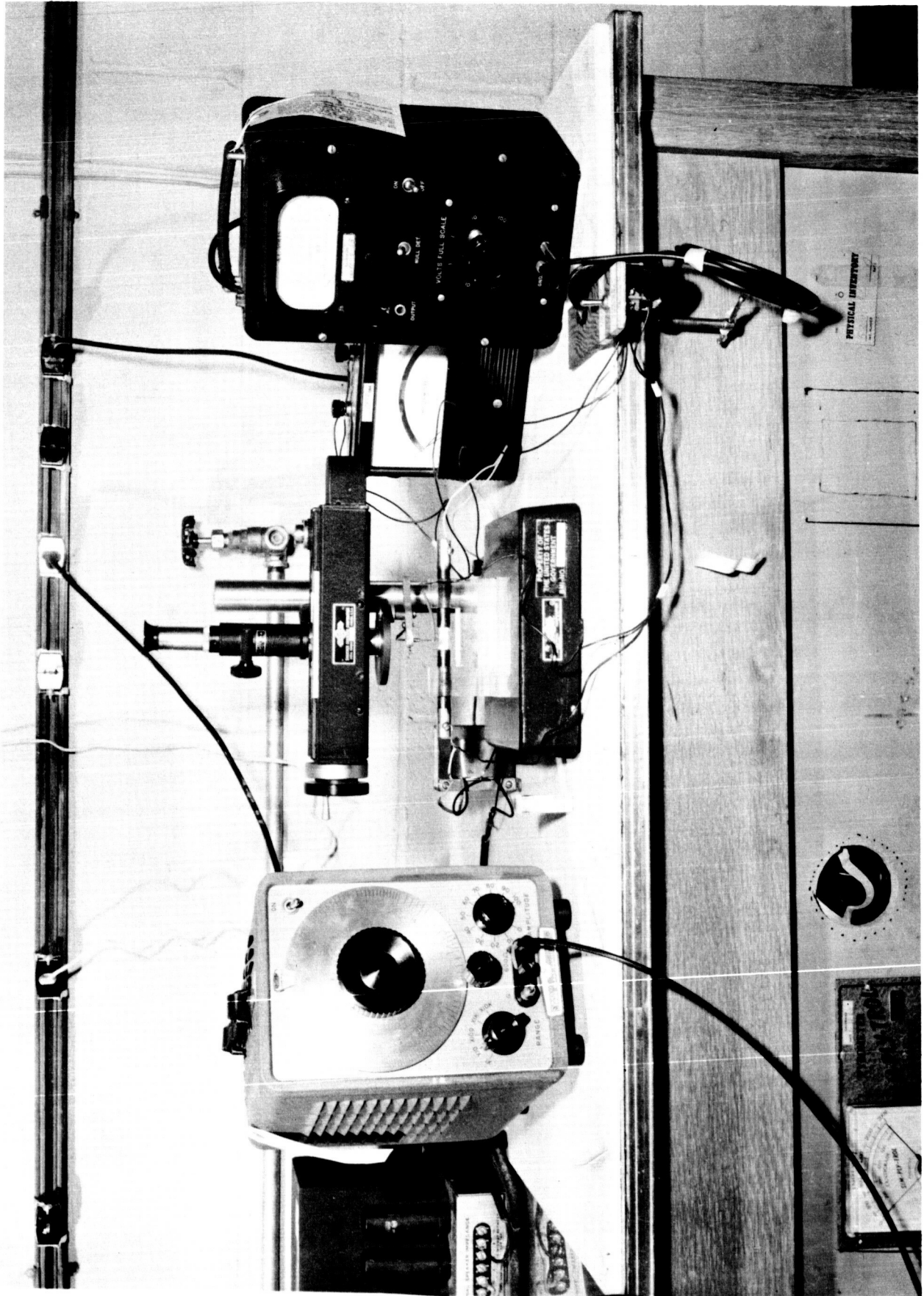
present at the surface being traversed, will generally produce an abrupt shift in the curve, indicating a sharp increase in resistance from the localized defect. A crack or discontinuity below the surface will cause the normally straight, sloping curve to become distorted in shape, producing a more rapid increase in voltage drop or resistance with traverse distance. Extrapolation of the straight-line portion of the curve of the thermoelectric material back to the interface permits one to determine the resistance attributable to defects and contact resistance. The sum of these effects may be considered as effective contact resistance.

Figure 28 shows examples of a "good" and "poor" specimen of p-type PbTe (Tegs 2) with iron shoes attached that had been hot pressed at 1400 F. The sharp discontinuity in the poor specimen indicates a sharp rise in resistance as the result of a crack in the thermoelectric material.

Effect of Pressing Temperature. Examination of resistance traverses of p-type specimens pressed at 1400 F and 900 F show the higher temperature to yield generally larger and more frequent discontinuities. This was supported by the observed greater frequency in the higher temperature specimens of shoes being separated from the elements upon decanning. On the basis of these results, the 900 F pressing temperature is to be preferred for the p-type material.

The Tegs 3p PbTe was also fabricated into specimens for resistance traversing but the extremely high degree of shoe separations obviated their inclusion in the test program. Two attempts to incorporate the Tegs 3p material were unsuccessful for lack of bonding. Tegs 3p-type PbTe was consequently eliminated from consideration in segment fabrication. Its relatively low power factor supported this decision.

Because of the favorable characteristics of the Tegs 2N-type PbTe, it was excluded from this traverse study. Random traverses and metallographic examinations performed on specimens pressed at 900 and 1400 F have shown no apparent difference in bond characteristics or element cracking tendencies. Cracks have seldom been detected in as-pressed n-type specimens. Temperatures in the range 900 to 1400 F are considered equally acceptable for the n-type PbTe fabrication.

Iron-Base-Alloy Evaluation. An alloy of iron-8 percent tin (designated BMI-8) investigated by Battelle was found to have an expansivity greater than iron, placing it between iron and PbTe. Since tin is commonly alloyed with both p- and n-type PbTe in the form of tin telluride, its presence in an iron shoe was considered to be potentially acceptable. On the basis of these factors, the alloy was evaluated against iron as a shoe material that might reduce cracking and possibly increase the life characteristics of the junction with PbTe.

The BMI-8 alloy was prepared by arc casting and was converted to powder by filing. Two powder sizes were prepared by milling in a mortar and pestle: -100 +270 mesh and -270 mesh. The test specimens were die pressed and hot isostatically pressed at 1400 F in a like manner with specimens containing iron shoes of -200 +270-mesh powder.

The fabricated specimens were traversed and then subjected to thermal aging in argon at 950 F. The aging was performed in three periods to provide these thermal
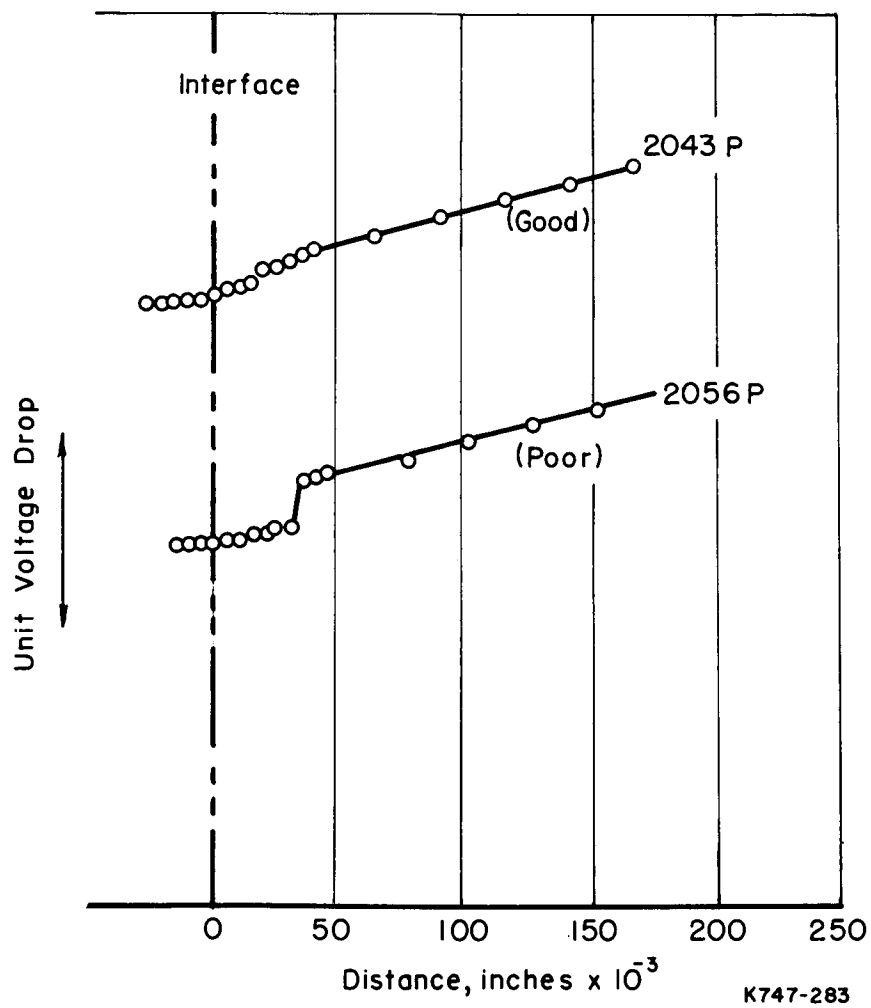
FIGURE 28.   EXAMPLES OF BONDED PbTe SPECIMENS BASED
ON RESISTANCE TRAVERSE MEASUREMENTS

cycles to room temperature. Resistance traverses were performed after each cycle. A total of 263 hours were accumulated at the aging temperature. The following observations were made as a result of this study.

(1) The fine, -270-mesh, alloy powder consolidated well, while the coarse, -100 +270-mesh, powder did not. The coarse shoes tended to crumble at their edges.

(2) The shoes made of coarse powder (poorly densified) showed the greatest tendency to remain intact on the specimens during cycling.

(3) The frequency of cracks or discontinuities in the traverse curves and the response to cycling among the three groups of specimens were essentially alike. The results showed no preference for either shoe material.

(4) The general effect of cycling was to create and/or increase the magnitude of each discontinuity in the traverse curve. Figure 29 shows an example of the effect of cycling and aging on the resistance-traverse curves of a BMI-8 specimen.

On the basis of these results, the following conclusions were drawn:

(1) Iron should be used for element fabrication until such time that the BMI-8 alloy, which is under investigation in other studies, is shown to offer merit.

(2) The high temperature of hot pressing (1400 F) and/or the thermal-cycle test may have imparted conditions too severe to show differences in shoe performance.

Concurrent with the above investigation, tests were initiated to ascertain whether the BMI-8 alloy is in fact free of adverse poisoning effects. The compatibility tests were performed on PbTe test specimens with iron and BMI-8 as separate powder additives to the p- and n-type PbTe. One weight percent additions were used and the specimens were hot isostatically pressed at 900 F. Elevated-temperature Seebeck-coefficient and room-temperature-resistivity determinations were made after pressing and after thermally aging for 70 hours and 220 hours at 950 F. The results are compared in Table 2.

The test data show that neither the n-type nor p-type PbTe specimens were adversely affected by the BMI-8 alloy. In the case of the n-type PbTe, after a 10-hour aging period at 950 F, the properties of the specimens with the two additions, closely matched the properties of the reference specimen having no addition. Similarly, after 220 hours of aging at 950 F, the specimen with the BMI-8 addition and the reference specimen exhibited essentially like properties. The p-type PbTe specimens containing iron and BMI-8 yielded properties which differed negligibly from one another, indicating no effect from tin. These two p-type PbTe specimens with additions did, however, differ significantly from the reference specimen containing no additions. This difference must be considered either an effect of the iron content alone or the presence of particles in the low ductility p-type material.
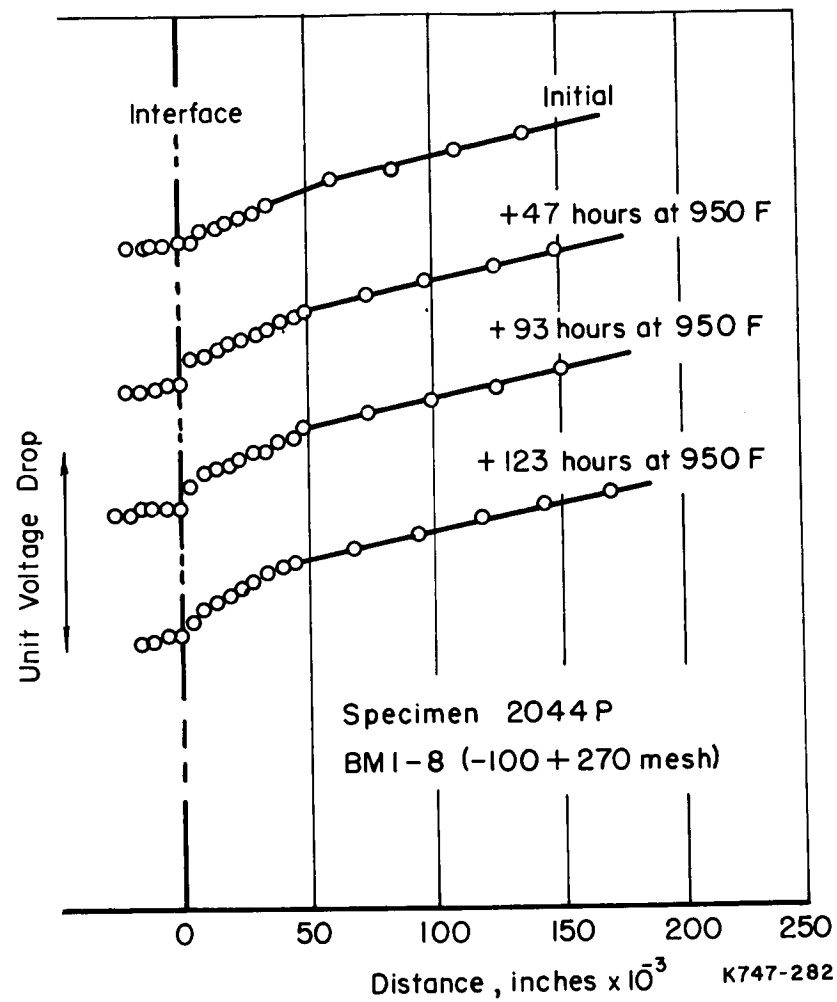
FIGURE 29. EFFECTS OF THERMAL CYCLING AND AGING ON
RESISTANCE TRAVERSES FOR p-TYPE PbTe

TABLE 2. EFFECTS OF SHOE-MATERIAL ADDITIVES ON THE ELECTRICAL PROPERTIES OF PbTe

Additive w/o	HIP 900 F Initial Properties		After 70 Hours at 950 F		After 220 Hours at 950 F	
	Resistivity(a), μohm-cm	Seebeck Coefficient(b), μV/C	Resistivity(a), μohm-cm	Seebeck Coefficient(b), μV/C	Resistivity(a), μohm-cm	Seebeck Coefficient(b), μV/C
p-Type PbTe						
No additive (ref. specimen)	780	261	780	259	585	260
1 Fe	538	224	1210	276	1360	276
1 BMI-8	627	237	1480	267	1400	277
n-Type PbTe						
No additive (ref. specimen)	735	235	623	231	630	231
1 Fe	677	240	647	232	--(c)	--(c)
1 BMI-8	627	226	647	228	620	233

(a) Room temperature.
(b) Average between 150 and 500 C.
(c) Lost as result of temperature excursion.

BATTELLE MEMORIAL INSTITUTE

Segmented Element Fabrication

The information generated in the aforementioned supporting studies, where the different parts of the segmented element were considered separately, was used to establish potential schemes for element fabrication. The term configuration as used herein applies to identification of the kinds and array of makeup materials in a particular element. Once a configuration was conceived, trial fabrications were attempted to assess the validity or practicality of the various factors involved. Fabrication of seven distinct element configurations by seven independent schemes was attempted in an effort to produce acceptable elements for performance testing.

Fabrication Scheme A

The first fabrication scheme, A, utilized the process of pressure bonding tungsten to iron with nickel as a bonding agent followed by either pressure bonding or brazing tungsten to SiGe with gold as a bonding agent. This is shown in Figure 30. The resulting configuration, A, was derived from the successful tungsten-nickel-iron transition members which could be produced by pressure bonding at 1400 F and 10,000 psi using either nickel foil or nickel preplated on the tungsten. Difficulties were encountered, however, in achieving sound SiGe-tungsten bonds with gold. These led to a series of studies previously discussed which indicated that oxide films on the SiGe prevents bonding below 1000 F. Consequently, Fabrication Scheme A was abandoned.

Fabrication Scheme B

On the basis of results obtained in studies of the high-temperature brazing of SiGe to tungsten, Fabrication Scheme B and associated Configuration B shown in Figure 31 evolved. Since the gold-nickel alloy was found to be a successful bonding agent for SiGe and tungsten which could withstand 1400 F, the pressure-bonding operation to form the tungsten-nickel-iron bond was selected to be the final operation. Although successful n-type elements could be produced by this process, it was found through study that the high-processing temperature (1400 F) required to produce the transition member bond resulted in a high frequency of iron-PbTe separations in p-type elements. Also, the 10,000 psi processing pressure caused internal stressing in the p-type PbTe, making it extremely sensitive to cracking. Figure 32 shows an n-type segmented element produced by this fabrication scheme. Upon grinding a surface of the element for visual study, it was found that cracks were present in the SiGe just above the bond interface. It was not apparent whether the cracks resulted from the tungsten-SiGe reaction or from internal stresses resulting from bending during the cool-down period after pressing. Further attempts to produce n-type elements by this approach were not successful, therefore this approach was discontinued.

Fabrication Schemes C and D

As a result of the technology developed in producing both n-type and p-type PbTe-iron segments by hot isostatic pressing at 900 F and 2500 psi previously described, and the success in brazing SiGe to tungsten with a gold-nickel alloy at 1800 F, Fabrication Scheme C shown in Figure 33 was devised. Fabrication Scheme C incorporates an
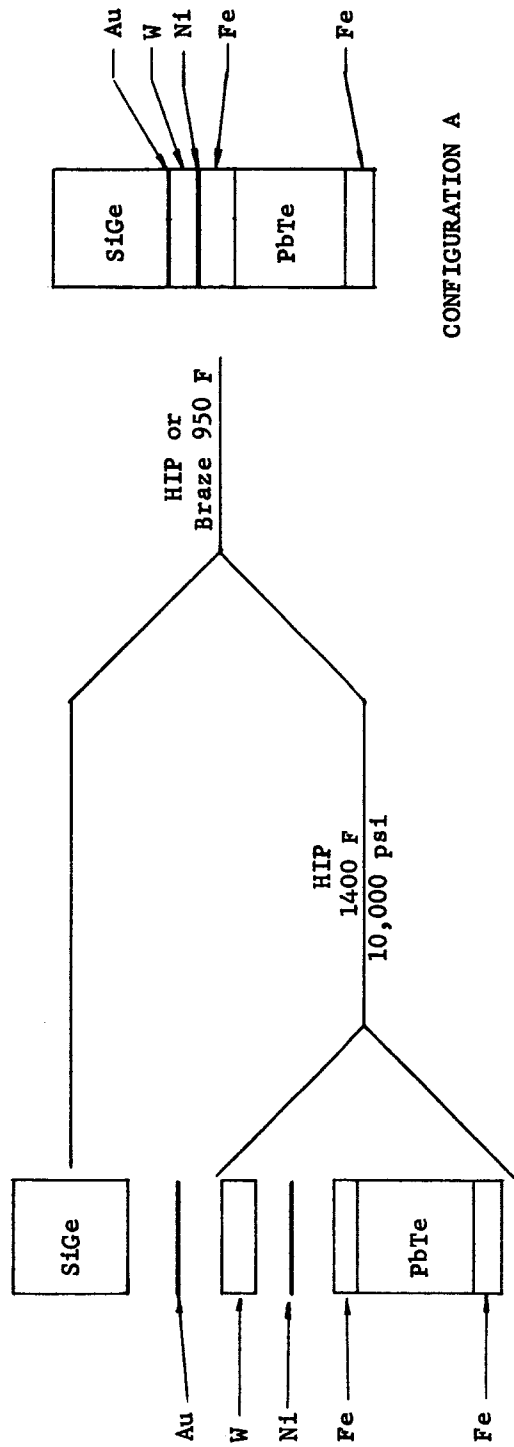
FIGURE 30. FABRICATION SCHEME A
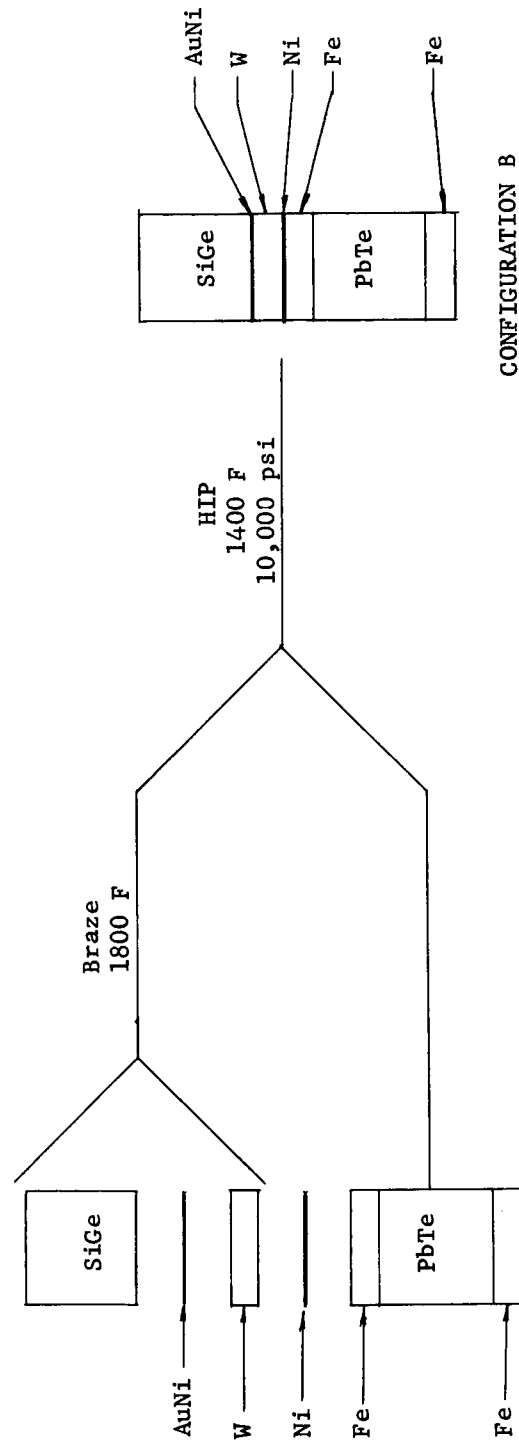
FIGURE 31.   FABRICATION SCHEME B

SiGe

Tungsten
Iron
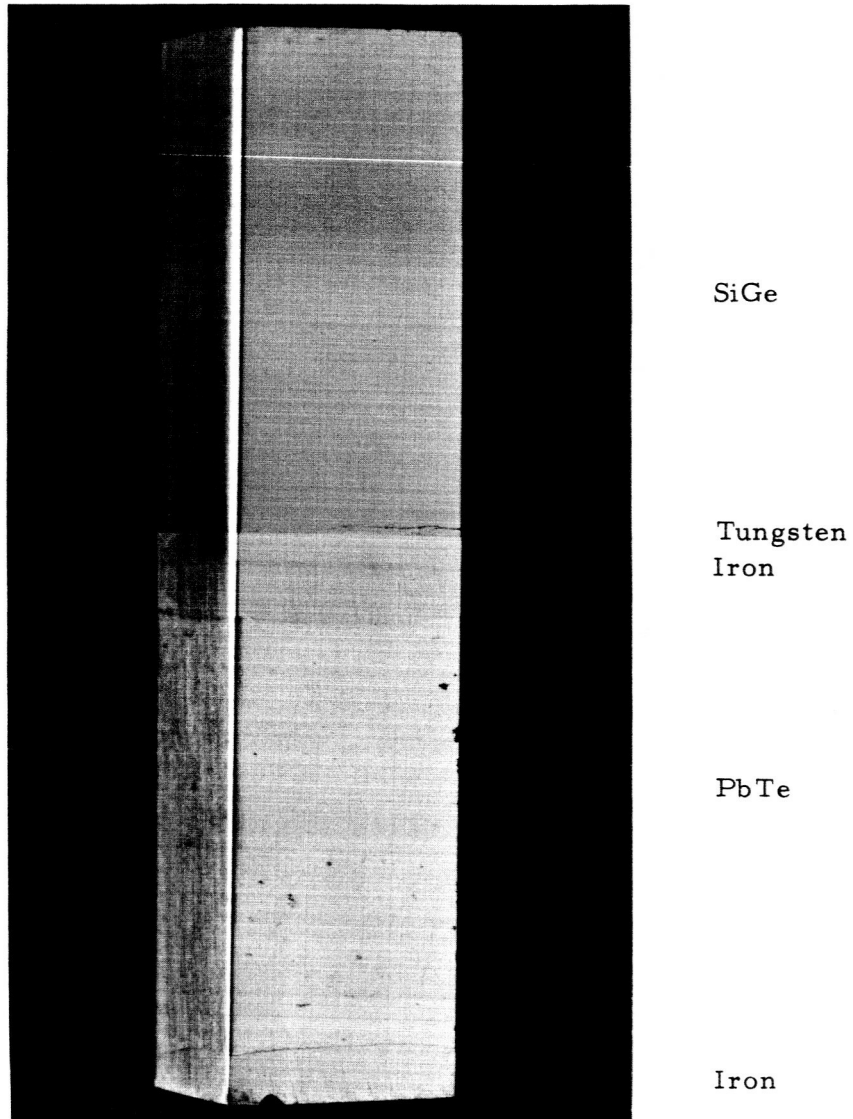
PbTe

Iron

FIGURE 32.   n-TYPE SEGMENTED SiGe-PbTe ELEMENT
FABRICATED BY SCHEME B
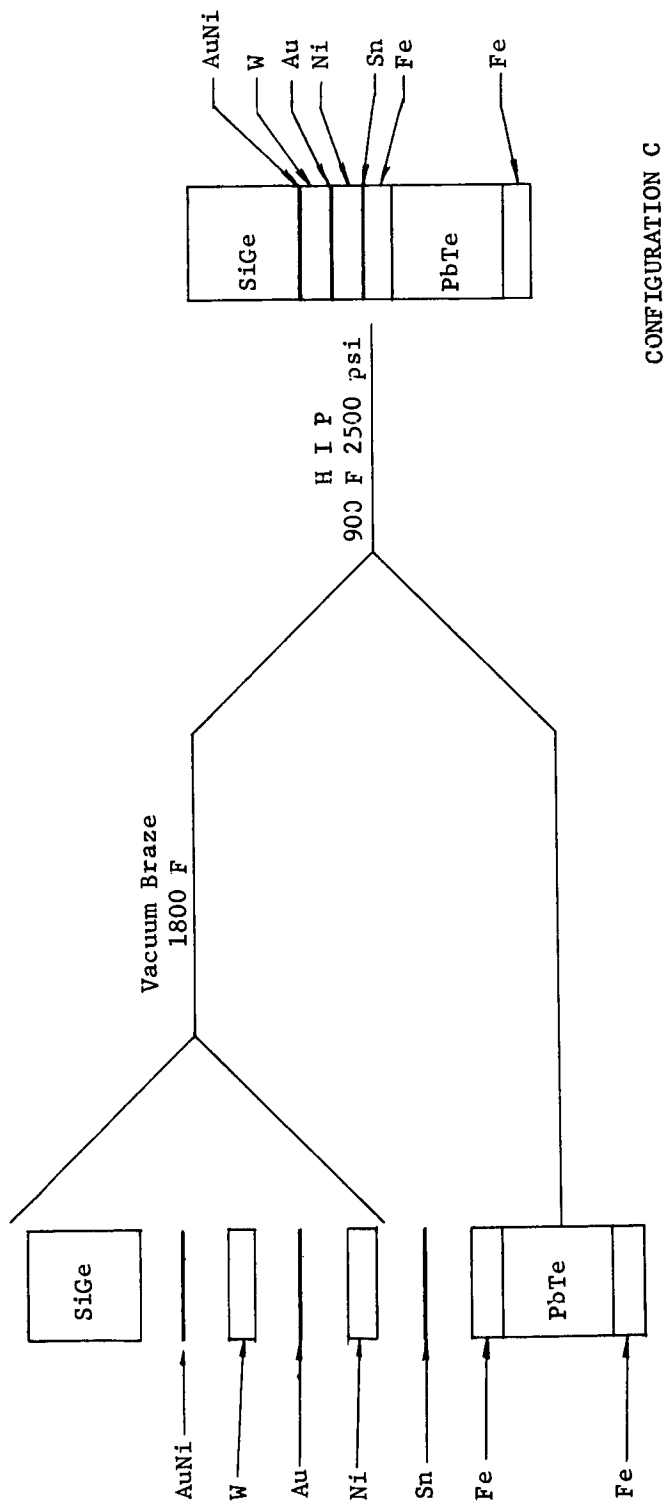
FIGURE 33. FABRICATION SCHEME C

intermediate layer of nickel brazed to the tungsten layer. Although the use of tin to join nickel and iron was based on previous experience, the bonding of the tungsten to nickel with gold remained to be demonstrated.

At this point of development, it was decided to additionally employ the state-of-the-art SiGe to tungsten direct reaction bond formed at 2000 F in vacuum. Fabrication Scheme D shown in Figure 34 incorporates this process. Since Fabrication Schemes C and D were quite similar, they were evaluated simultaneously.

The initial attempts to achieve the SiGe-to-tungsten bond with the gold-nickel alloy according to Scheme C resulted in unexpected failure whereas the direct reaction of SiGe to tungsten in Scheme D were totally successful. In both configurations the gold braze of a powder-pressed nickel layer to tungsten remained intact even though severe attack of the nickel by the gold braze material had occurred. Close examination of this condition indicated that the particles of the die-pressed-powder nickel were separated by the action of the molten gold phase. Although the attack produced a considerable amount of internal porosity in the nickel, the electrical resistance of the transition member was not found to be objectionably affected. With both Schemes C and D, re-producibility of the tin braze of nickel to iron was found to be quite variable. Upon examination it was found that in instances when this bond was unsuccessful, gold from the tungsten-nickel union was found to have penetrated completely through the porous nickel, preventing good melting at the nickel-iron interface. The gold infiltrated nickel member is shown in Figure 35.

In an effort to overcome the problem of penetration of gold into the porous powder nickel, fabrication of these configurations was repeated using a solid-wrought nickel member in place of die-pressed powder nickel. Although the previous difficulties associated with the tungsten-nickel-iron transitions were found to be greatly reduced, the production of sound SiGe-tungsten bonds of Fabrication Schemes C and D both became quite variable. The poor SiGe-to-tungsten bonds achieved were attributed to the use of wrought nickel. The theory is that the nickel became soundly bonded to the tungsten near the brazing temperature and the differential thermal expansion of the two members that occurs during cooling caused the tungsten shoe to bow, thereby disrupting the SiGe-to-tungsten bond. This occurrence was evidenced by the warped and sometimes cracked condition of the bonded tungsten-nickel composites found after the high-temperature brazing process. To confirm the theory on the SiGe-tungsten bond disruption problem, the initial brazing step in Scheme D was repeated using pressed-powder nickel members as in earlier attempts. Sound SiGe-to-tungsten bonds were achieved.

It was necessary to replace die-pressed powder nickel in Fabrication Schemes C and D with wrought nickel to overcome the variability in forming the nickel-iron transitions. Hot die pressing was considered in place of the initial brazing process to permit incorporation of wrought-nickel without disruption of the SiGe-tungsten bond. In theory, it was believed that if sufficient pressure could be applied during bonding to prevent the warpage that occurred in the tungsten-nickel composites during brazing, sound SiGe-to-tungsten bonds might result. In the initial attempt to hot press the SiGe-tungsten-nickel composite in Fabrication Scheme D at 2000 F and 500 psi for 20 minutes, it was found that the gold from the tungsten-nickel joint had squeezed out during pressing and reacted with the SiGe. It was recognized that this reaction resulted from extrusion of a gold-nickel liquid phase that could have formed as low as 1800 F. Since it had previously been found that sound mechanical bonds between tungsten and nickel could be obtained within 20 minutes at 1700 F using gold as a bonding agent, the hot pressing temperature was reduced to 1700 F. The period of processing was increased to one
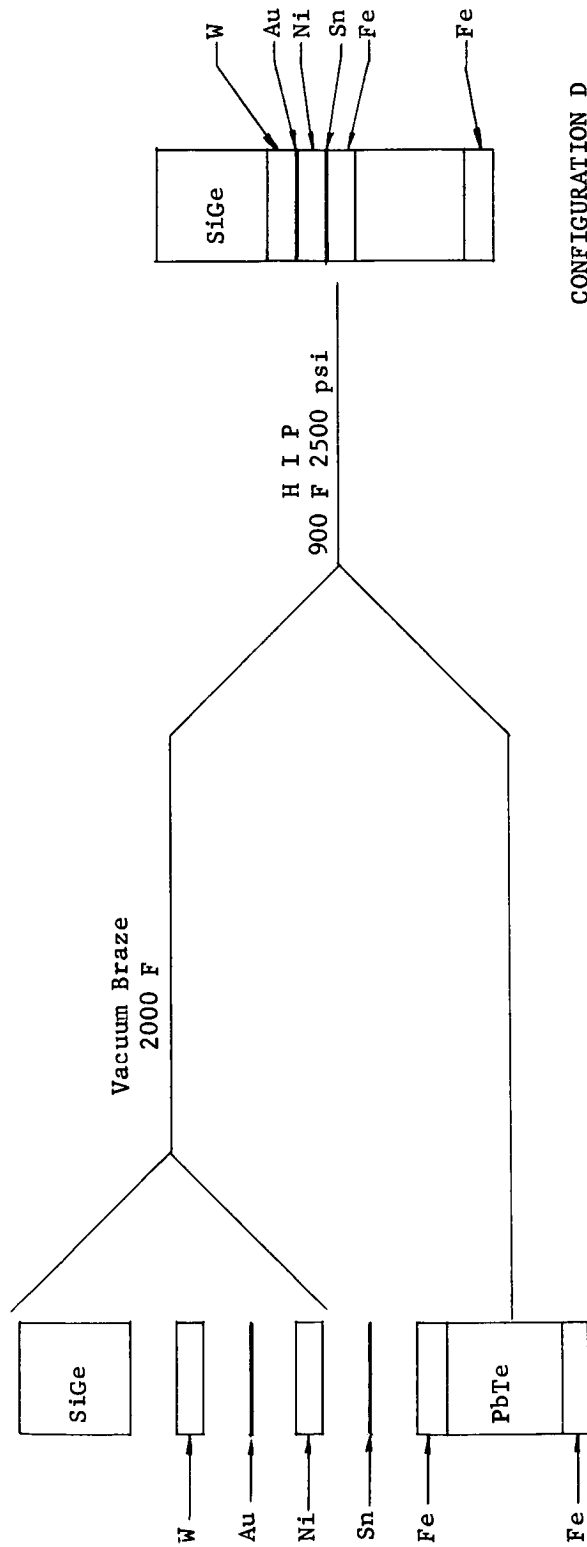
FIGURE 34.   FABRICATION SCHEME D

Ni

Au penetration

Sn braze

Fe

500X   26792
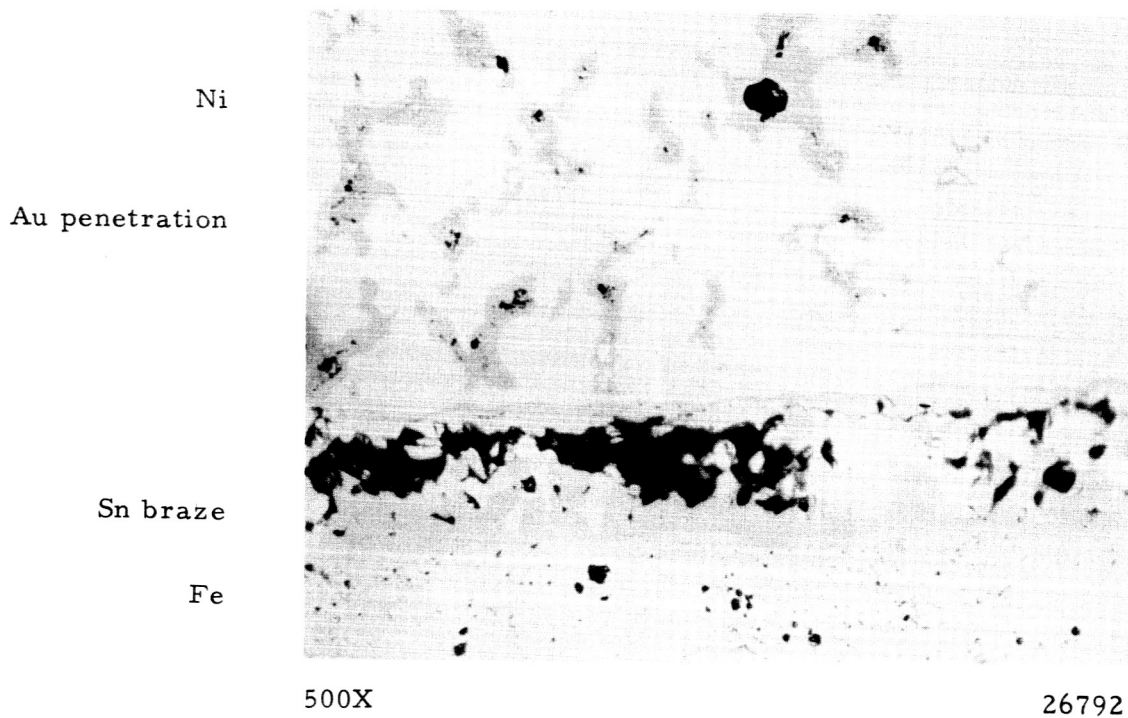
FIGURE 35.   PHOTOMICROGRAPH SHOWING THE PENETRATION OF
             GOLD THROUGH THE NICKEL TO THE NICKEL-IRON
             TRANSITION

hour, however, to enhance the formation of the direct SiGe-to-tungsten reaction bond. Acceptable nickel-to-tungsten bonds were obtained but the 1700 F pressing temperature was inadequate to form the SiGe-to-tungsten bond. Hot pressing in place of brazing in Scheme D was consequently abandoned.

Hot pressing of the SiGe-tungsten-nickel composite was further evaluated in Scheme C which employs the gold-nickel braze material at the SiGe-to-tungsten bonds. Hot pressing was again performed at 1700 F but only partial SiGe-to-tungsten bonds were obtained.

Fabrication Scheme E

Since the direct reaction bonding of SiGe to tungsten and the use of die-pressed powder nickel members appeared promising if the gold infiltration problem could be circumvented, Fabrication Scheme E shown in Figure 36 was devised. In this scheme the hot-isostatic-pressing operation for joining the SiGe-tungsten-nickel composite to the iron-PbTe composite as in the previous fabrication schemes was replaced by a 500 F brazing operation used to form a bronze-type bond between the iron and nickel. Copper was plated on the nickel to provide a suitable bonding surface and tin was used to alloy with the copper in forming the bond to iron. The poisoning effect of copper on PbTe was not considered to present a problem here because the high-density iron shoe acts effectively as a barrier to copper diffusion to the PbTe. The hot-isostatic-pressing procedure required for forming the iron-PbTe composite was isolated as a separate earlier step.

Prior to employing Fabrication Scheme E, a heretofore unrecognized inherent deficiency in the powder-nickel member was uncovered. Elements successfully made by Schemes C and D were found to break through the powder-nickel member during the brazing cycle or upon subsequent heatup operational performance testing. Fracture occurred in the weaker porous center section of the nickel member as an apparent result of differential thermal expansion caused by the attacked iron and tungsten. To increase the strength of the nickel members, densification was attempted by application of greater pressure during bonding. This was accomplished by employing a bonding rig designed to apply pressure through the differential thermal expansion of molybdenum and stainless steel. Previously a dead weight loading system had been used. By incorporating a dual screw arrangement in the bonding rig, coupling of the SiGe segment with a SiGe strap during the initial bonding operation became standard practice.

Several elements of Configuration E were successfully produced; however, obtaining adequate reproducibility of the SiGe-tungsten bonds during the high-temperature vacuum brazing was unexpectedly found to be a major problem. The SiGe-tungsten bond was variable in contrast with the results seen earlier with the powder-product member. Visual examination of the bonded tungsten-nickel composites revealed that warpage had occurred similar to that experienced with the use of wrought nickel. The acceptable elements of Configuration E which were produced were found by study of the electrical resistance characteristics to possess no undesirable discontinuities. The lack of reproducibility of Configuration E required exploration along another path.
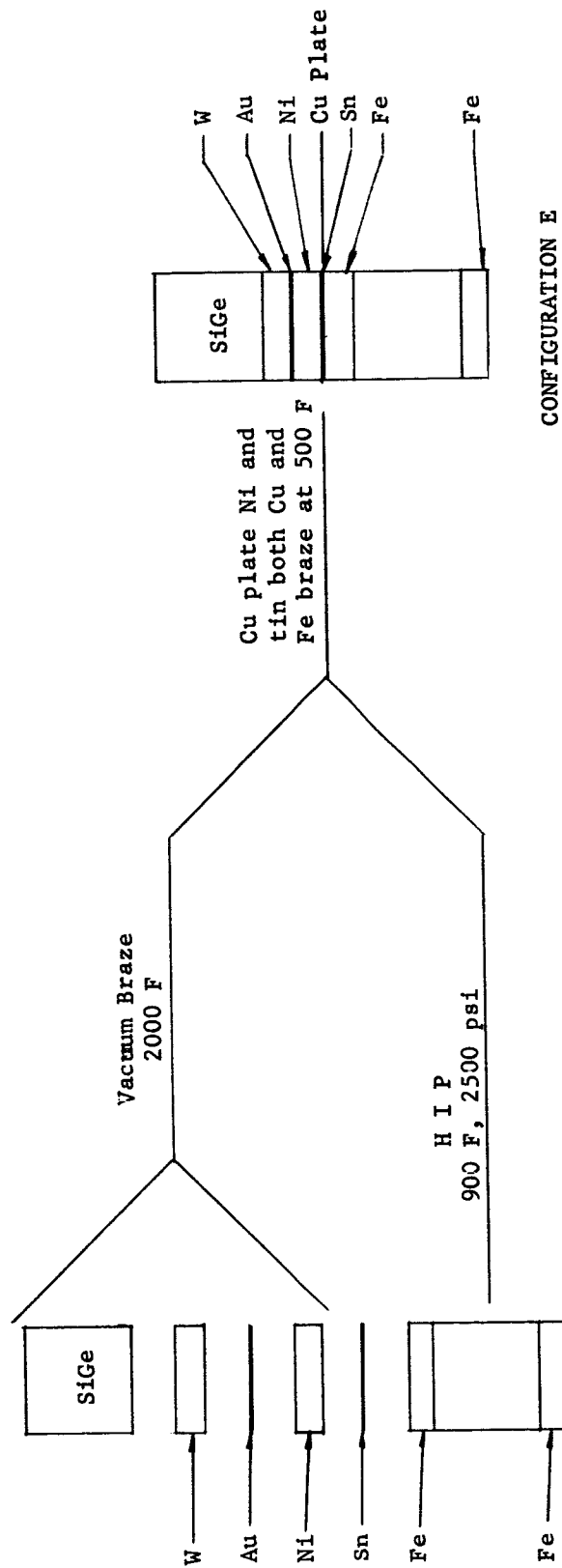
FIGURE 36. FABRICATION SCHEME E

Fabrication Scheme F

Fabrication Scheme F shown in Figure 37 was devised to take advantage of the reproducibility achievable in separately forming the direct reaction SiGe-to-tungsten bonds. Plating of a layer of electroless nickel on the tungsten was selected to permit application of the nickel member without the previously experienced warpage problem. Joining of the iron member to the tungsten again employs the bronze alloy bond as previously discussed. Applying the layer of nickel on the tungsten after achievement of the SiGe-tungsten bond effectively avoided the warpage and difficulties encountered in simultaneous bonding the two at a high temperature. Acceptable elements were fabricated by this scheme but considerable difficulty was encountered in obtaining an adherent layer of electroless nickel on the tungsten.

Fabrication Scheme G

The variability still encountered with Schemes E and F necessitated study of other systems of segmenting which might reduce the problem of bonding materials with large differences in thermal expansion rate. Since the high expansion rate of nickel apparently causes disruption of the SiGe-to-tungsten bonds, a substitute material for nickel was sought. Platinum which possesses a thermal expansion rate midway between tungsten and iron (nickel expansion coefficient is greater than iron) and which could potentially be bonded to tungsten was selected for evaluation. Study showed that platinum could be bonded to tungsten with gold at 1950 F and could be readily copper plated for formation of the braze alloy. A two-step process for forming the SiGe-tungsten-platinum member was selected. The tungsten-to-platinum member was formed initially at 1950 F followed by gold brazing of the SiGe to tungsten at 1500 F. At 1500 F, the eutectics of gold-silicon and gold-germanium produced sound bonds between SiGe and tungsten. Also the 1500 F operation reduced the temperature range through which the bonds were cooled, thereby additionally reducing the stressing effect of differential thermal expansion. Fabrication Scheme G which is based on these changes is shown in Figure 38. Several thermoelements of this configuration were then prepared for testing.

Performance Testing of Segmented Couples

To study the operational behavior of the segmented thermoelements produced in this program, a test apparatus designed to measure the power and voltage characteristics of a couple under conditions typical of generator operation was employed. Basically, the apparatus is equipped with an electrical heater which provides controlled temperature to the hot strap of the test couple, and a water-cooled pedestal onto which the test couple is mounted. The electrical circuitry of the apparatus is such that the power output of the p- and n-elements of the test couple can be measured separately. The environmental conditions of a test couple can be controlled by either evacuating the enclosure in which the couple is located or by introducing a protective gas cover under controlled conditions.

Two thermoelectric couples were tested in the apparatus during this program. The first couple, which was of the Configuration F type, underwent four thermal cycles before a hot-junction temperature of 1100 K was achieved. The difficulty in attaining

61
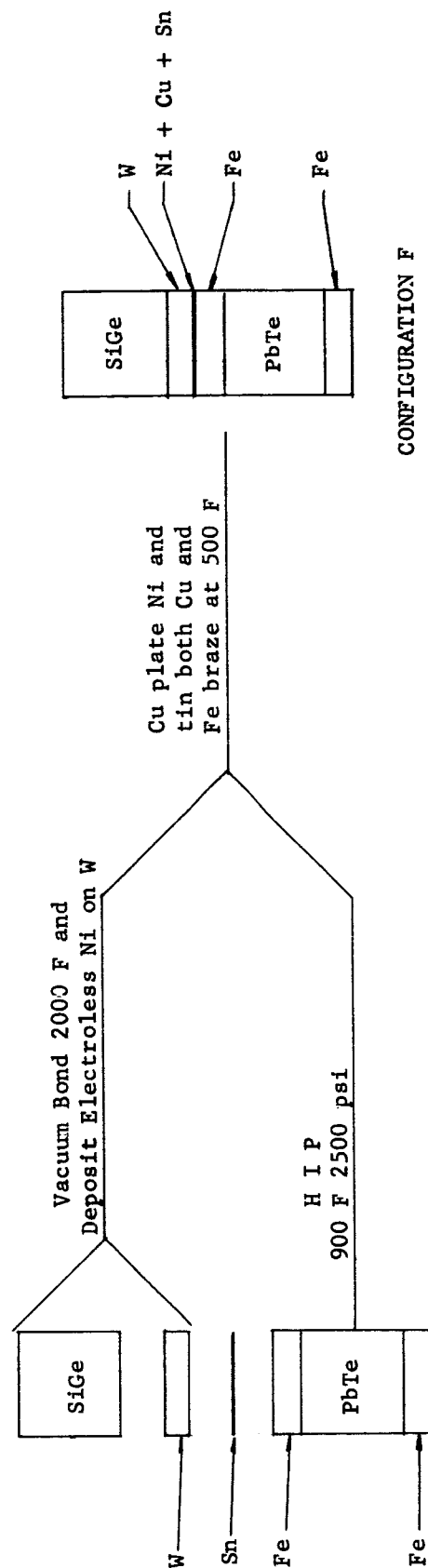
FIGURE 37. FABRICATION SCHEME F
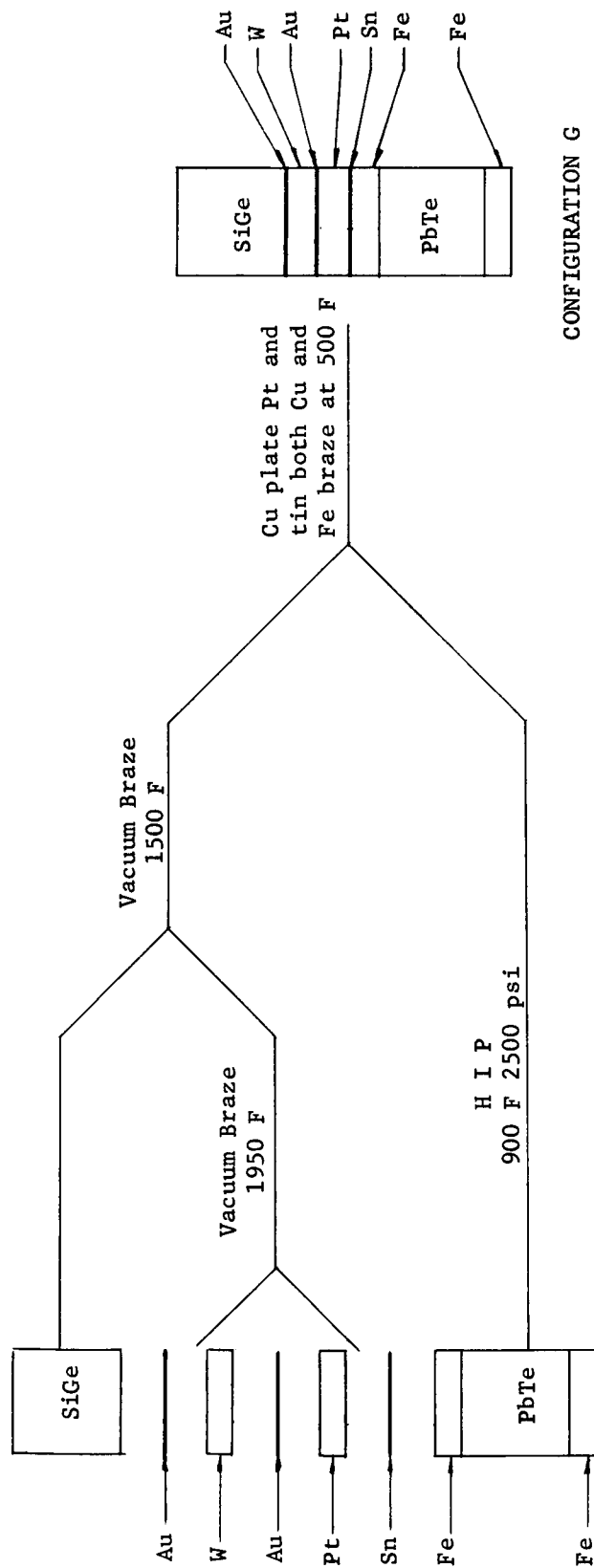
FIGURE 38. FABRICATION SCHEME G

the desired hot-junction temperature of 1200 K was caused by heater problems in the test equipment. Although this couple had been observed to possess severe cracks in the PbTe prior to startup of testing and experienced four thermal cycles, an output power of approximately 0.85 watt was attained. The open-circuit voltage was measured to be about 380×10^{-3} volts which is near the analytically determined value for this segmented configuration.

The second test couple, which was of Configuration G was placed on test and a limited hot-junction temperature of 1100 K was again achieved. The open-circuit voltage of this test couple at 1100 K was also measured to be about 380×10^{-3} volts. However, the output power was determined to be only about 0.596 watt. Upon removing this couple from test, it was found that the tungsten-platinum composite in both the n- and p-elements had separated from both the SiGe and the Fe shoe of the PbTe segment resulting in extremely poor electrical and thermal contact.

Summary

The development of segmented PbTe-SiGe thermoelements was performed by study of element shoe and transition material properties and applying fabrication processes or "schemes" devised to accomplish bonding between components without exceeding known limiting parameters. The prime objective of the segmenting activity was the development of sound thermoelectric elements capable of performing at their calculated level of efficiency. The studies conducted were not limited by selection and adherence to a single fabrication approach; hot isostatic pressing as well as hot die pressing and vacuum brazing were utilized in the development effort. Thermoelements were produced and tested to a limited extent in this program, but there remains a need for additional work aimed at achieving a fabrication process and an appropriate materials combination for production of thermoelements of greater reliability. Further testing and optimization of segment lengths is also required to achieve the desired high-performance thermoelectric elements expected from segmenting of SiGe and PbTe.

A study was made of potential materials combinations and processing conditions for producing transition members between SiGe and PbTe segments. A hot-isostatic-pressing process involving pressing at 1400 F and 10,000 psi was found potentially capable of producing n-type segmented elements with a transition layer consisting of tungsten, nickel, and iron. However, fabrication of p-type elements by these conditions was not possible because of the cracking and excessive fragility produced in the p-type PbTe segment.

Several fabrication schemes and materials combinations were explored which primarily involved combinations of braze and hot isostatic pressure bonding of the components. The major problem in achieving acceptable segmented elements was found to be caused by the differential thermal expansion and stressing of the SiGe-to-tungsten bond by the second material bonded to the tungsten. The various fabrication schemes were established primarily to overcome this difficulty by appropriate sequencing of the processing operations or selection of the method of material application.

Nickel used in the transition layer was found most readily applicable when used in powder-pressed form rather than wrought form. Wrought nickel because of its high strength caused warping of the tungsten member and consequent disruption of the

SiGe-to-tungsten bond. Powder-pressed nickel is weak as the result of low density and its use avoided these problems. Since fracture within the powder-pressed nickel randomly occurred, its use did not provide a valid solution to the transitioning problem. Platinum which was selected to replace nickel because of its lower expansion rate has exhibited improved performance over nickel when bonded to a tungsten shoe. Further evaluation of the use of platinum as a transitioning metal will be performed in the continuing program.

Gold or gold-nickel braze materials were found effective in joining SiGe, platinum, or nickel to tungsten. Bonding of SiGe to tungsten was found to be successfully accomplished by direct reaction bonding at 2000 F or by reaction bonding with gold in the range 1500 to 2000 F in vacuum. Attempts to react gold with SiGe at 1000 F in high vacuum or with the use of fluxing agents proved unsuccessful.

Studies of the electrical properties of PbTe consolidated by hot isostatic pressing showed Tegs 2p and Tegs 2n materials to possess acceptable electrical properties whether processed at 900 F or 1200 F. Tegs 2p PbTe were found superior to Tegs 3p PbTe on the basis of power-producing capability.

Hot isostatic pressing at 900 F was preferred over pressing at 1400 F on the basis of resistance studies of the junctions made with powder-product iron shoes. Tegs 2p PbTe was found to be more easily joined to iron shoes than Tegs 3p PbTe. A 900 F hot-isostatic-pressing schedule was selected for fabrication of the PbTe segments used in most of the segmenting studies.

A study of the compatibility of a candidate iron-tin alloy with both p-type and n-type PbTe by means of a seeding technique showed it to produce no adverse effects on either the Seebeck coefficient or resistivity.

TASK III. DEVELOPMENT OF A THERMAL INSULATION
AND SUPPORT STRUCTURE

TASK III. DEVELOPMENT OF A THERMAL INSULATION AND SUPPORT STRUCTURE

Objective

The objective of this task is to fabricate and test a selected grouping of heat-source support and thermal-insulation structures in order to obtain their thermal and mechanical properties. On the basis of these data, a correlation with analytical predictions will be made to define and extend the relations describing performance of the insulation.

Scope of Work

The scope of this development work includes the fabrication, thermal testing, structural testing, and performance correlation of a selected group of insulation structures. Fabrication of 18 selected insulation structures was accomplished by gas-pressure bonding after completion of experiments for optimization of the bonding process. The thermal conductance, compressive strength, and shear strength of the insulation structures were measured and compared with predicted values yielding analytical expressions for insulation performance. Performance curves, in terms of the insulation parameters, were evolved to allow rapid evaluation of the insulations' structural and thermal behavior.

Design of Insulation Structures

The insulation structure is pictured in Figure 39. The parameters are shown in Figure 40 where:
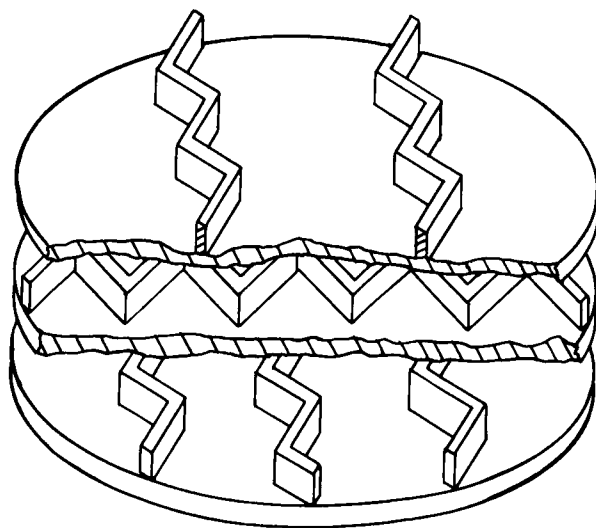
K747-277

FIGURE 39. METALLIC-INSULATION STRUCTURE
BATTELLE MEMORIAL INSTITUTE
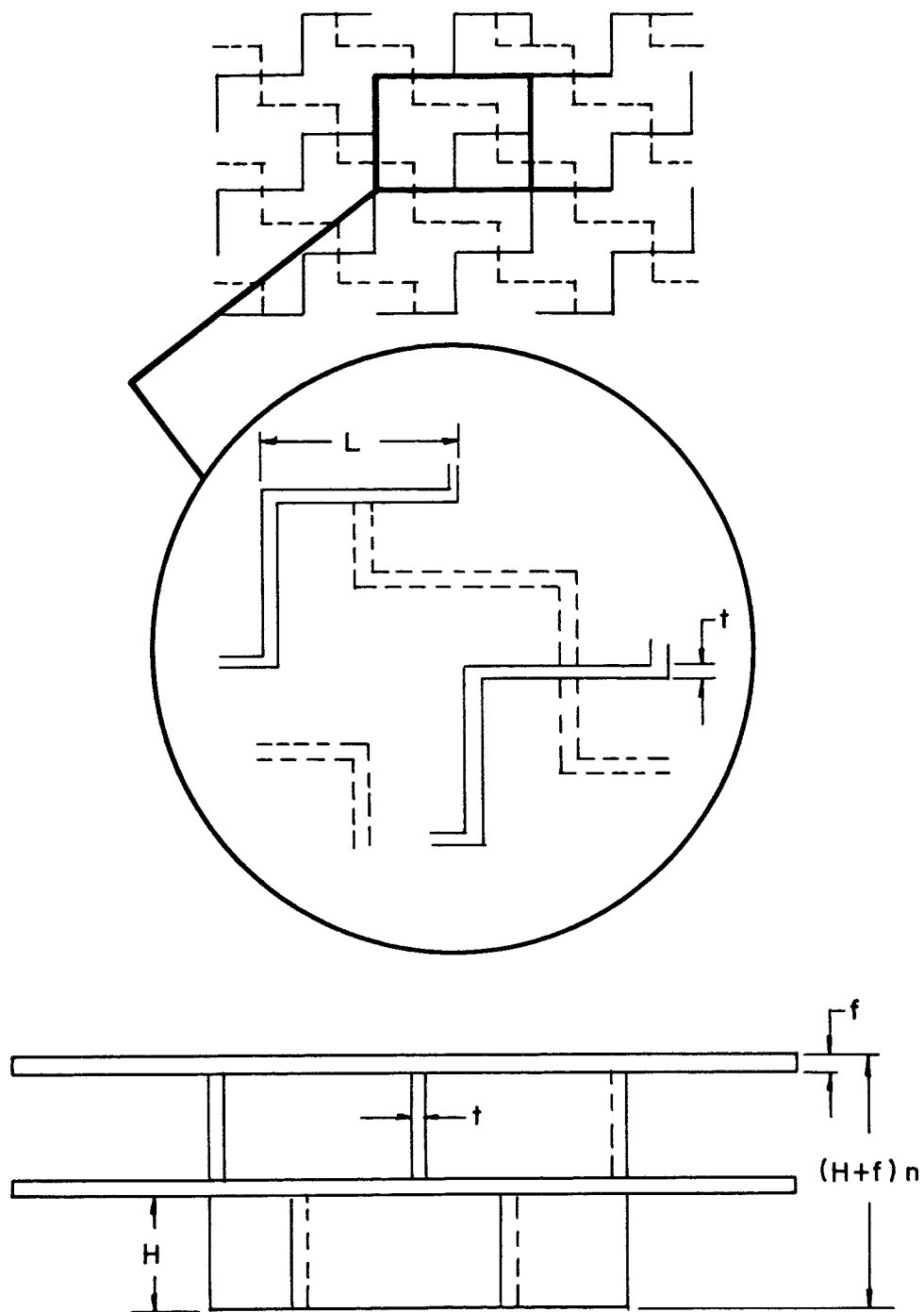
FIGURE 40.   REPEATING SECTION OF INSULATION STRUCTURE
SHOWING DIMENSIONAL PARAMETERS

L = web-bend length
H = web height
t = web thickness
f = foil thickness.

Two series of structures were fabricated, covering two ratios of web-bend length to web height. Within each series, structures were selected that combine three foil thicknesses and three web thicknesses. For Type 1 structures, the web-bend length is 1 centimeter and for Type 1/2 structures, the web bend length is 1/2 centimeter. For all specimens, the foil spacing, or web height is 0.05 in. These size combinations represent expected extremes of strength, weight, and thermal resistance. Nine structures of each type were produced, as shown in Table 3. The specimens consist of five web layers separated by four foils. Each structure has a 1/16-inch-thick end plate on both sides to facilitate testing procedures.

The sample structures were 3 inches in diameter. These were generated from 3-1/2-inch-square sections fabricated by diffusion bonding. In this process, the web and foil components of the structures are fabricated separately and then assembled with necessary spacer material (tooling) into complete unbonded structures. The unbonded structures are then compressed under vacuum, at high temperature, for an adequate time to effect diffusion bonding of all components. The filler tooling is then removed from the structures by selective acid leaching. Hastelloy C was chosen as a candidate material for the insulation structures because of its low thermal conductivity and high-temperature strength.

TABLE 3. COMPONENT DIMENSIONS FOR INSULATION STRUCTURES

Structure	Web Thickness, inch	Foil Thickness, inch
1		0.004
2	0.004	0.008
3		0.012
4		0.004
5	0.008	0.008
6		0.012
7		0.004
8	0.012	0.008
9		0.012

Fabrication of Insulation Structures

The fabrication of the insulation structures may be discussed in terms of four efforts: the bonding process optimization, the fabrication of the components, the subsequent assembly and bonding of these components into structures, and the final acid leaching and finishing operations.

Bonding-Process Optimization

Past experience at Battelle has demonstrated the feasibility of using the gas-pressure-bonding process to fabricate honeycomb and honeycomb-like structures from a wide variety of engineering materials. Predicting the optimum self-bonding parameters for most engineering materials in many cases would not be a difficult task. The quality of the bond is dependent on the selection of the gas-pressure-bonding parameters and the effects of interaction of the leachable tooling with Hastelloy C. A minimum of diffusion interaction between Hastelloy C and the tooling is necessary because the tooling is eventually acid leached from the Hastelloy C. A large reaction zone between Hastelloy C and the tooling would result in a rough Hastelloy C surface after leaching, increasing the emittance of the parallel foils in the final structure. Because the magnitude of these problems was unknown, an experimental program was initiated to generate data that could be used to aid in the selection of the bonding-process parameters and the tooling materials.

Initially, duplicate specimens were made of Configurations 1, 2, and 3 (Figure 41) for bonding at 2100 F and 10,000 psi for 3 hours. These initial bonding conditions were chosen because they had proved successful in bonding other iron- and nickel-base alloy systems. Nickel and iron were chosen as the tooling because they are relatively inexpensive, are stable at the expected bonding-temperature range, and are readily dissolvable in a variety of common acids that do not attack Hastelloy C.

The chrome plating in Configuration 2 and platinum foil in Configuration 3 were selected to serve as a diffusion barrier in the event that neither plain iron nor nickel in Configuration 1 proved to be suitable.

The Hastelloy C in Configurations 2 and 3 was prepared for bonding by dipping in a solution of 50 parts nitric acid, 10 parts hydrofluoric acid, and 40 parts water until the surface was etched to a light satin finish.

The nickel-plated Hastelloy C in Configuration 1 was prepared by dipping in a hot alkaline cleaning solution. After acid or alkaline cleaning, each piece was rinsed in distilled water and ethyl alcohol. The iron- and nickel-tooling pieces, as well as the tooling with chrome plate and platinum foil, were prepared by scrubbing in a hot alkaline solution, followed by rinses in distilled water and ethyl alcohol. During assembly the components were handled with gloves and tongs and/or tweezers.

The components were sealed in a stainless steel envelope by tungsten inert gas (TIG) welding. The final weld closure was made in an electron-beam welder. After gas pressure bonding at 2100 F and 10,000 psi for 3 hours, Configurations 1, 2, and 3 were evaluated by metallographic examination and leaching. Selected acids were used to leach the candidate tooling from the Hastelloy C. The surfaces of the Hastelloy C that had been next to the tooling were visually observed to determine corrosive effects on surface finish.

Metallographic examination of Configuration 1 specimens (Figure 42) indicated an extensive diffusion reaction between iron and Hastelloy C, while only moderate reaction was observed between nickel and Hastelloy C. Grain growth did not occur across the self-bond interface. Apparently the nickel plate on the Hastelloy C acted only to inhibit grain growth and not to promote bonding as originally expected.

Nickel

Hastelloy C --0.00005-inch nickel plate
at interface.

Armco Iron
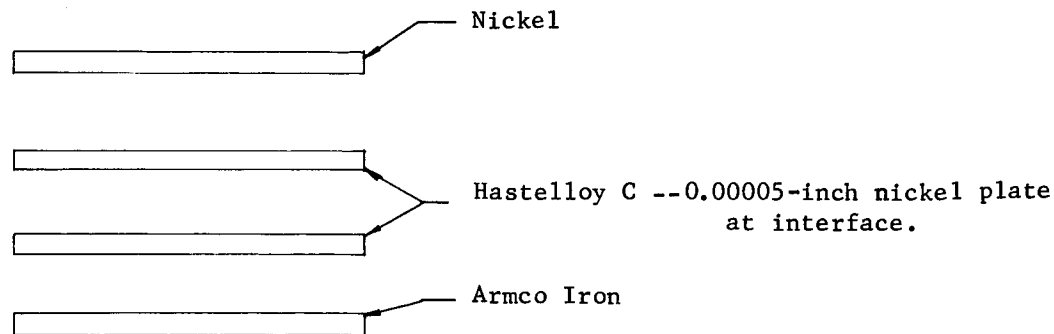
(a) Bonding Coupon Configuration 1

Purpose: Evaluation of Hastelloy C self-bond employing nickel plate
as a diffusion aid.
Evaluation of reaction between Hastelloy C and candidate
iron and nickel tooling.

Nickel

Chrome Plate

Hastelloy C

Chrome Plate

Armco Iron
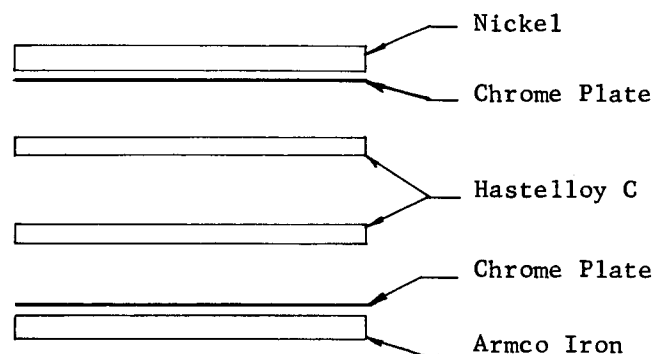
(b) Bonding Coupon Configuration 2

Purpose: Evaluation of Hastelloy C self-bond.
Evaluation of reaction between Hastelloy C and chrome-plated
iron and nickel tooling.

Nickel

Hastelloy C

Platinum Foil (0.002 in.)

Armco Iron
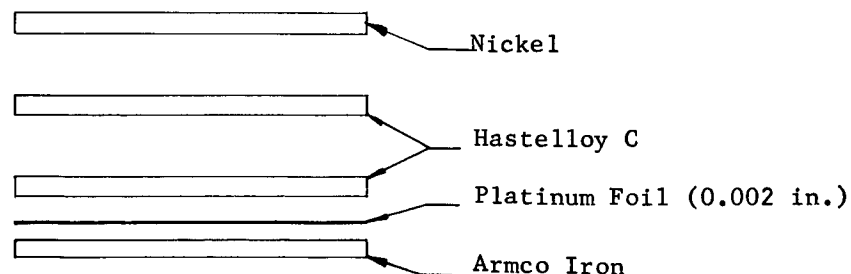
(c) Bonding Coupon Configuration 3

Purpose: Evaluation of Hastelloy C self-bond.
Evaluation of reaction between Hastelloy C and nickel and
iron with platinum foil diffusion barrier.

FIGURE 41. EXPERIMENTAL BONDING-COUPON CONFIGURATIONS

Bonding-process parameters: 2100 F, 10,000 psi, 3 hours.

BATTELLE   MEMORIAL   INSTITUTE

Metallographic examination of Configuration 2 specimens (Figure 43) revealed a broad reaction zone between the chromium-plated Armco iron and Hastelloy C. Apparently chromium had diffused quite deeply into both components. Only a moderate amount of reaction was observed between the chromium-plated nickel and Hastelloy C, although an intermediate phase had formed between the nickel and Hastelloy C. The Hastelloy C self-bond was excellent. No trace of the original interface is evident as grain growth has occurred across the interface along the entire length of the specimen. An additional picture of the bond at higher magnification is shown in Figure 44 to illustrate its appearance.

Examination of Configuration 3 specimens (Figure 45) indicates that a narrow reaction zone was formed between platinum and the adjacent materials, Hastelloy C and Armco iron. When the composite was leached in hot nitric acid, dissolving the Armco iron, the platinum-clad surface of the Hastelloy C had a black appearance. Examination of the Hastelloy C self-bond in the specimen revealed a bond which appeared to be of equal quality with the bond in Configuration 2 specimens shown in Figure 44.

From these results on the first series of specimens, the following observations were made:

(1) From the extent of diffusion penetration and the appearance of Hastelloy C surfaces after the tooling had been leached, nickel appears to be the most desirable material to have in contact with the Hastelloy C during pressure bonding.

(2) The Hastelloy C surfaces adjacent to the chromium-plated and platinum-covered nickel and iron tooling were badly discolored after removal of the tooling. It is thought that this condition would result in high emittance.

(3) Sulfuric acid does not dissolve either iron or nickel rapidly enough to be considered for the primary leaching solution.

(4) Below 180 F, Hastelloy C is not attacked by nitric acid of any concentration. The hot acid rapidly dissolves Armco iron. It attacks nickel at a moderate rate.

(5) Hastelloy C self-bonds were obtained at 2100 F and 10,000 psi for 3 hours.

Improvement of Surface Finish. Several experiments were performed to improve the surface finish of Hastelloy C. Specimens were immersed in a slurry of silicon carbide grit and water. The specimens were held stationary while the slurry was vibrated, first at a high frequency and low amplitude, and then at a high amplitude and low frequency. Microscopic examination of the metal surfaces was made at various time intervals during each vibratory exposure. Little or no improvement in surface polishing was achieved.

Another technique for improving the surface finish is to decrease the diffusion interaction between Hastelloy C and the tooling by lowering the bonding temperature. Specimens of Configurations 4 and 5, shown in Figure 46, were prepared and bonded at 2000 F instead of at 2100 F at 10,000 psi for 3 hours.

Nickel
diffusion
zone

Location of
original
interface

Diffusion
zone

Armco
iron

22714

100X
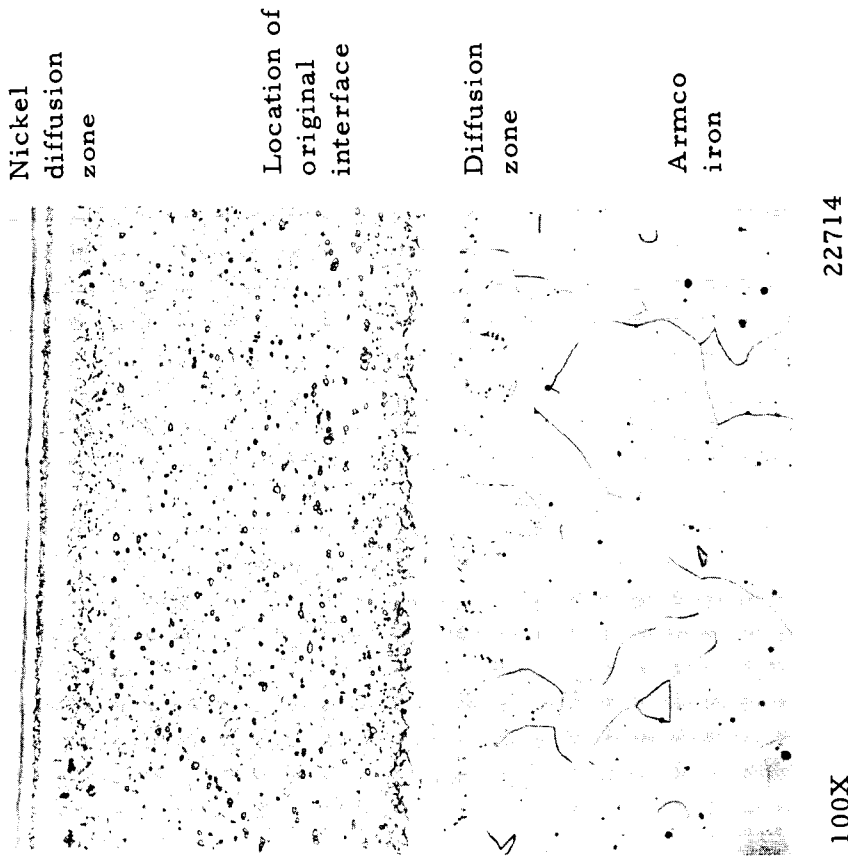
FIGURE 43. METALLOGRAPHIC SECTION OF
CONFIGURATION 2 SPECIMEN
GAS-PRESSURE BONDED AT
2100 F AND 10,000 PSI FOR 3 HOURS

Nickel

Diffusion
zone

Self-bond
interface

Diffusion
zone

Armco iron

22710

100X
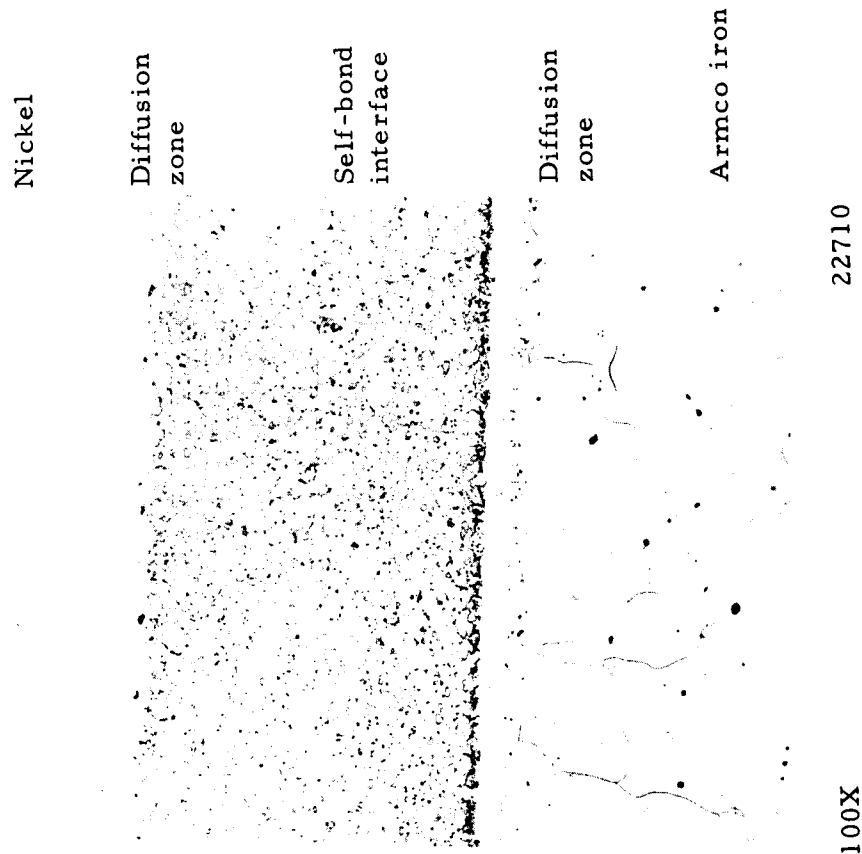
FIGURE 42. METALLOGRAPHIC SECTION OF
CONFIGURATION 1 SPECIMEN
GAS-PRESSURE BONDED AT 2100 F
AND 10,000 PSI FOR 3 HOURS

BATTELLE   MEMORIAL   INSTITUTE

73
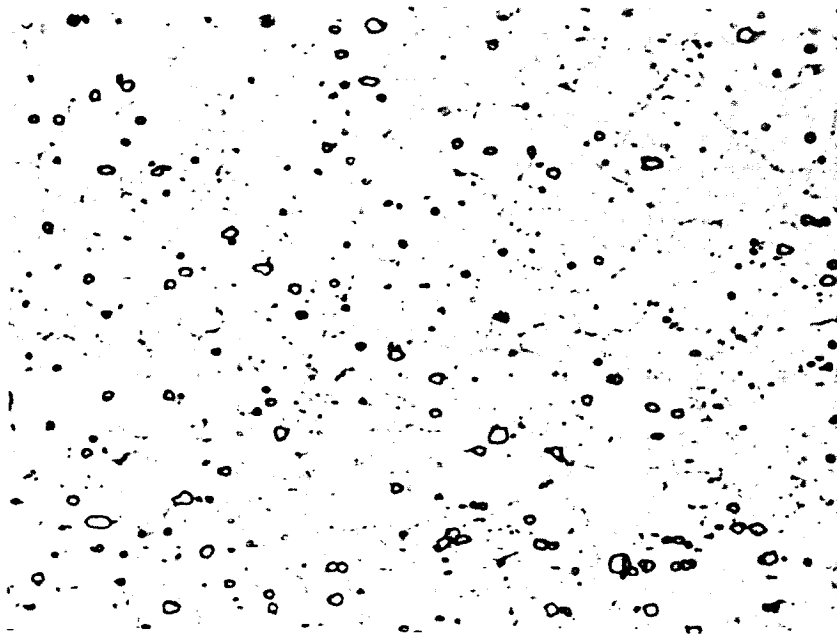
500X   22714B

FIGURE 44. HASTELLOY C SELF-BOND FOUND IN CONFIGURATION
            2 SPECIMENS GAS-PRESSURE BONDED AT 2100 F AND
            10,000 PSI FOR 3 HOURS
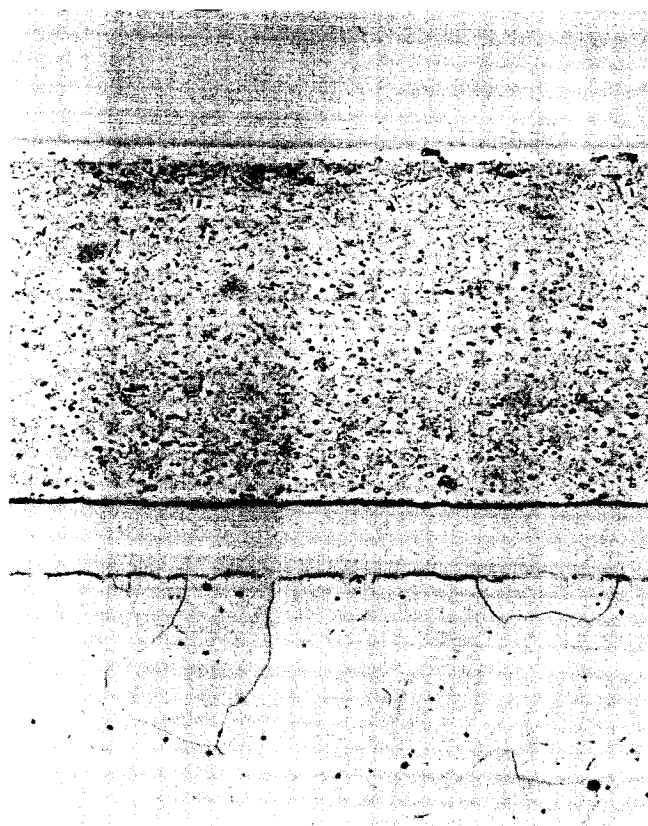
Nickel diffusion
zone

Location of original
interface

Platinum and diffusion
zone

Armco iron

100X   22712

FIGURE 45. METALLOGRAPHIC SECTION OF CONFIGURATION
            3 SPECIMEN GAS-PRESSURE BONDED AT 2100 F
            AND 10,000 PSI FOR 3 HOURS

BATTELLE   MEMORIAL   INSTITUTE

Nickel

Hastelloy C -- 0.00005-inch nickel plate
at interface.

Nickel Plate (0.003 inch)
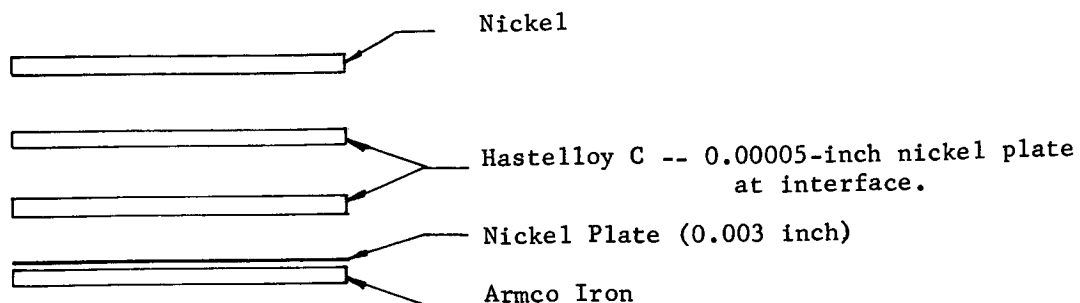
Armco Iron

(a) Bonding Coupon Configuration 4
Purpose: Evaluation of Hastelloy C self-bond employing nickel plate
as a diffusion aid.
Evaluation of reaction between Hastelloy C and nickel and
nickel-plated Armco iron.

Nickel

Hastelloy C

Nickel Plate (0.002 inch)
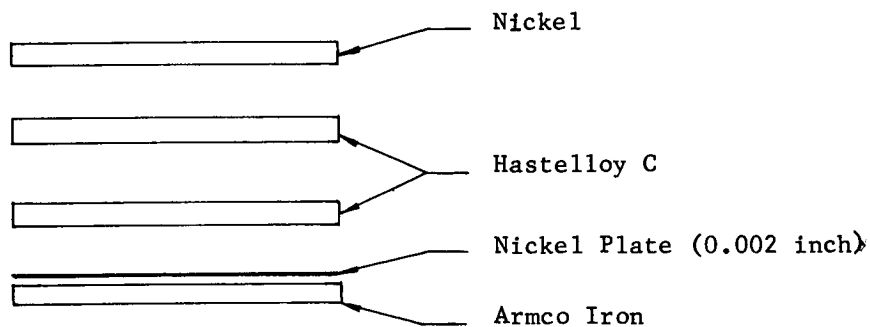
Armco Iron

(b) Bonding Coupon Configuration 5
Purpose: Evaluation of Hastelloy C self-bond.
Evaluation of reaction between Hastelloy C and nickel and
nickel-plated Armco iron.

FIGURE 46. EXPERIMENTAL BONDING-COUPON CONFIGURATIONS-BONDING-
PROCESS PARAMETERS: 2000 F, 10,000 PSI, 3 HOURS

After bonding, the specimen configurations were examined to evaluate the Hastelloy-tooling interface. At the tooling interfaces, Figures 47 and 48, the diffusion reaction between the Hastelloy C, nickel, and the nickel-plated Armco iron was considerably less than that observed when bonding was performed at 2100 F. After leaching in nitric acid, the surfaces of the Hastelloy C had a metallic luster and visually appeared improved over the surfaces obtained from the specimens bonded at 2100 F.

The Hastelloy surfaces adjacent to solid nickel appeared to be the most reflective. However both plating thicknesses on the Armco iron also gave good results, and the composite tooling was dissolved much more rapidly than solid nickel. The surfaces adjacent to the 0.003-inch-plate thickness appeared slightly more reflective than those adjacent to the 0.002-inch nickel plate; however, a significantly longer period of leaching was necessary to remove the 3-mil-plated tooling. A compromise was made by weighing the apparent surface quality and plating thickness with the time required to remove the tooling. It was judged that 2-1/2 mils of nickel plate on the tooling would produce the desired surface finish and still allow rapid removal of the tooling.

The self-bond interface of the Configuration 4 specimen, Figure 47, did not exhibit cross grain growth. This was also observed in the Configuration 1 specimen bonded at 2100 F. In both instances, the nickel plate acted to inhibit rather than promote self bonding. In the Configuration 5 specimen, grain growth had occurred across the self-bond interface, leaving little or no evidence of the original interface, especially when viewed at high magnification, Figure 48. Thus, the use of nickel plating is unnecessary to promote Hastelloy C self bonding. Referring to Figure 48, it is noted that shading discontinuity occurred at the interface. This is due to a varying degree of second-phase precipitation across the specimen. Second-phase precipitation is less at the original Hastelloy C alloy surfaces, probably because of alloy depletion from heating operations during the production of the sheet stock.

The last step in the evaluation of the surface-finish was conducted by making an emittance measurement on the most promising of the coupons bonded at 2000 F. This coupon (Configuration 4, Figure 41) was bonded with one face against solid nickel and the other face against Armco iron plated with 3 mils of nickel. Visibly, the latter side was slightly less reflective after leaching. Thus, the emittance measured is probably slightly higher than that which may be achieved with solid-nickel tooling. The measured values for the emittance are shown below:

Temperature, C	Hemispherical Total Emittance
229.0	0.18
252.9	0.18

This emittance value lies between the values given in the literature* for polished and shot-blasted nickel; thus, the surface-finish evaluation was concluded.

Selection of Optimized Bonding Process. On the basis of the results described above, the bonding parameters were established as 2000 F and 10,000 psi for 3 hours. Armco iron plated with 2-1/2 mils of nickel was chosen for the filler tooling. Nitric acid was selected as the tooling leachant.

*Wood, W. C., Deem, H. W., and Lucks, C. F., DMIC Report 177, Vols 1 and 2, November 15, 1962.
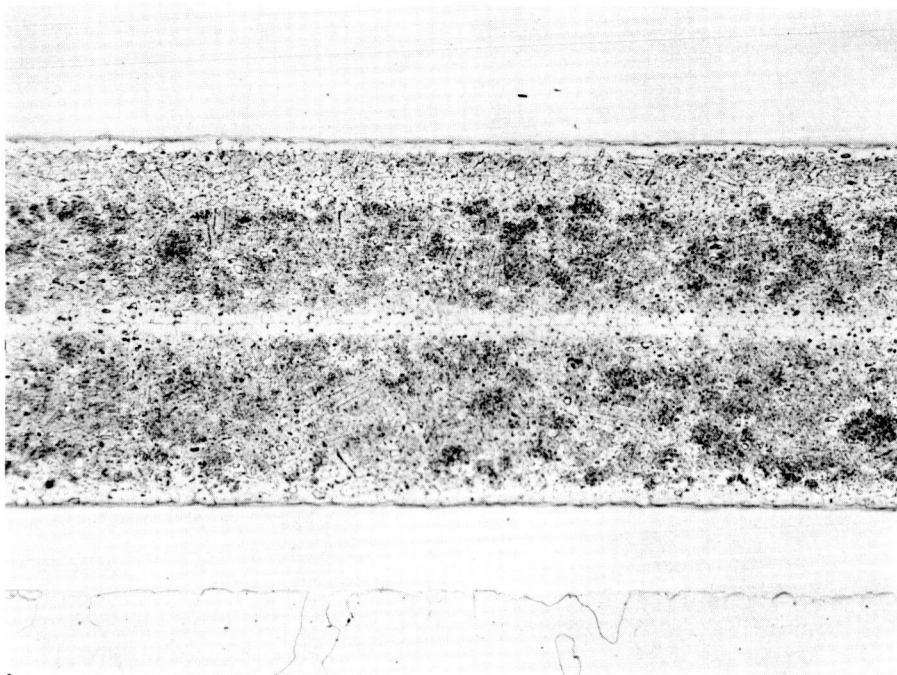
100X   23294

FIGURE 47.   METALLOGRAPHIC SECTION OF CONFIGURATION
              4 SPECIMEN GAS-PRESSURE BONDED AT 2000 F
              AND 10,000 PSI FOR 3 HOURS
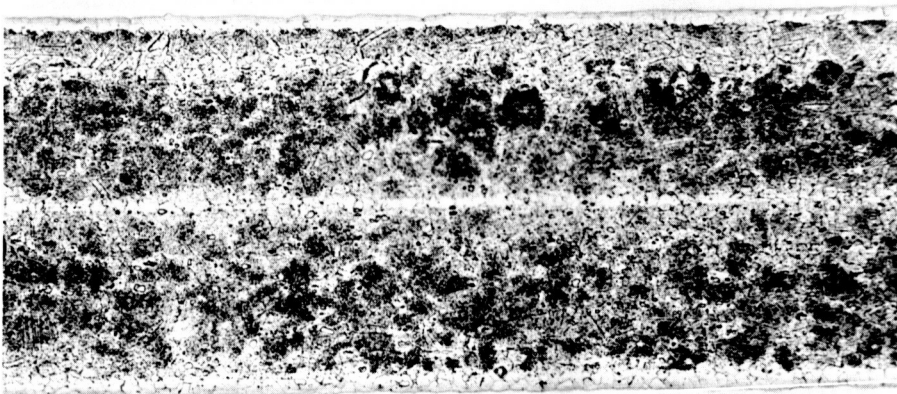
100X   23293

FIGURE 48.   METALLOGRAPHIC SECTION OF CONFIGURATION
              5 SPECIMEN GAS-PRESSURE BONDED AT 2000 F
              AND 10,000 PSI FOR 3 HOURS

Component Fabrication

This effort includes fabrication of the foils, webs, and filler tooling. Tooling is required to effect internal spacing of the structures during bonding. Because of the varying web thicknesses, the tooling pieces had to be custom designed to assure symmetric web intersections in adjacent layers. Four types of tooling pieces are required. These are shown in Figure 49, a and b. The tooling was machined from 0.045-inch Armco iron blanks which were sheared from rolled sheet and plated with 0.0025 inch of sulfate nickel.

Prior to fabrication of the structural webs, investigations were carried out to determine the simplest method for producing the webs. It was determined that webs of different thickness (4 mil, 8 mil, and 12 mil) may be corrugated with one die for each of the two proposed web-bend lengths. Thus, two web-corrugating dies were designed and fabricated. The die surfaces were 4340 steel. The dies are shown in Figure 50, a and b. The webs were sheared from annealed Hastelloy C foil and corrugated using the dies in an automatic press. Subsequent to corrugation, the webs were stacked together to be gound to the proper height, 0.052 inch, which is 2 mils greater than the plated tooling height to allow for upset in the bonding process. Corrugated webs may be seen in Figures 49 and 50.

Material for the foils was received in strip form and was sheared into 3-1/2-inch squares.

Assembly and Bonding

The corrugated webs, foils, plated tooling, and can components were separated into groups and cleaned in preparation for assembly and bonding. All Hastelloy C components were cleaned by degreasing in methyl-ethyl-ketone, pickled in acid for 2 to 5 minutes, rinsed in distilled water, dipped in ethyl alcohol, and dried under a heat lamp in a dust-free area. The acid solution consisted of 50 parts concentrated nitric acid, 10 parts concentrated hydrofluoric acid, and 40 parts distilled water. The nickel-plated tooling and steel-can components were cleaned in a strong alkaline solution, rinsed in distilled water, dipped in ethyl alcohol, and dried under a heat lamp in a dust-free area.

The components were assembled in an air-conditioned room where the air was filtered and maintained at a constant 68 degrees. Gloves and degreased tools were used during the assembly and handling of the components. Figure 51 is a view of the assembly table.

The insulation structures were assembled by placing the components into "picture-frame" cans. Figure 52 shows the picture-frame can on the right and the other components, shown from left to right, in the order in which they are placed in the can.

After the components were placed in the frame, a stainless steel cover plate was welded in place. The cans were sealed by electron-beam welding, leak checked, and gas-pressure bonded at 2000 F and 10,000 psi for 3 hours.
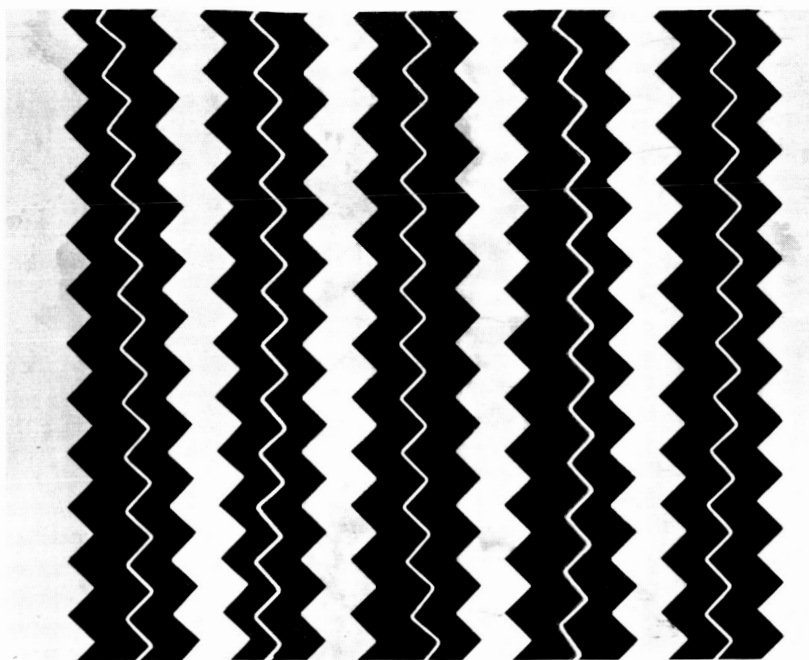
25920

a. 1/2-Centimeter Web-Bend Length
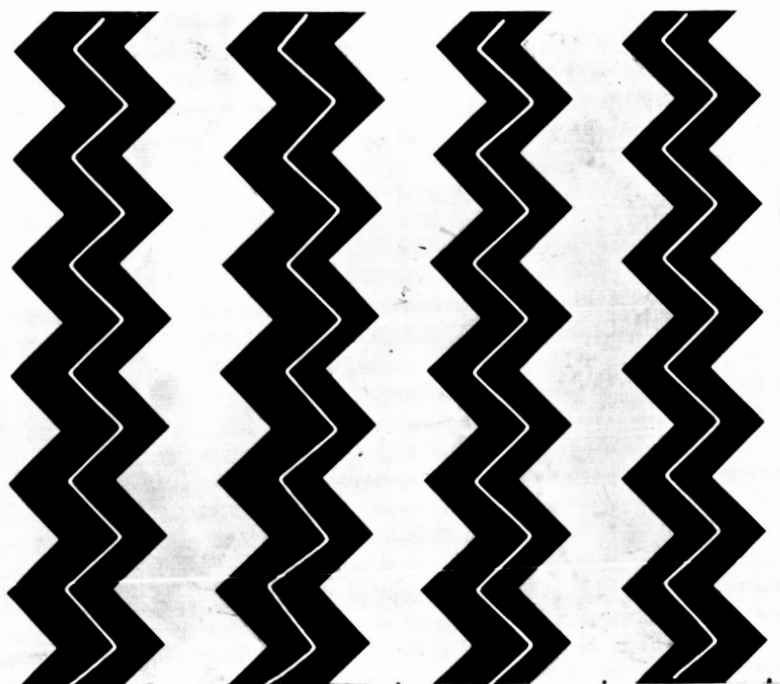
25919

b. 1-Centimeter Web-Bend Length

FIGURE 49. TYPES OF FILLER TOOLING AND WEBS SHOWING TWO
WEB-BEND LENGTHS
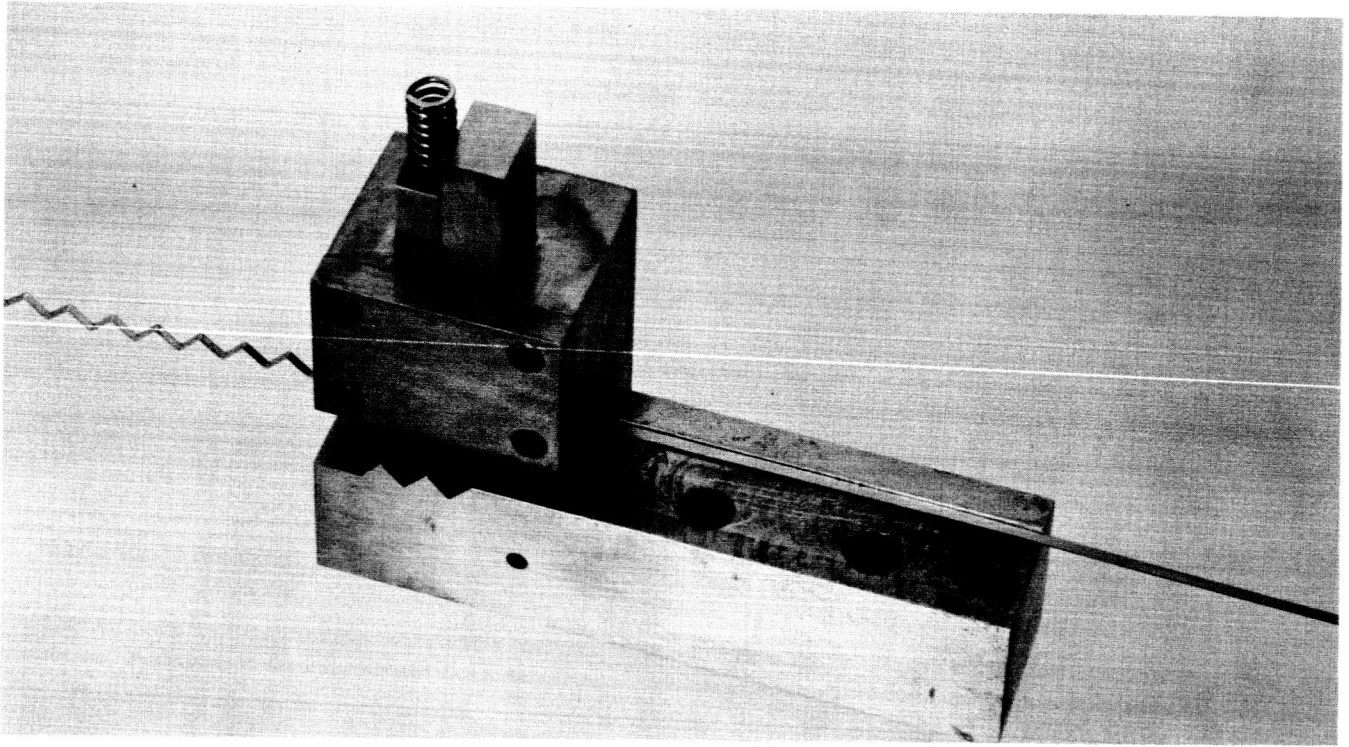
a. 1/2-Centimeter Web-Bend Length

25917
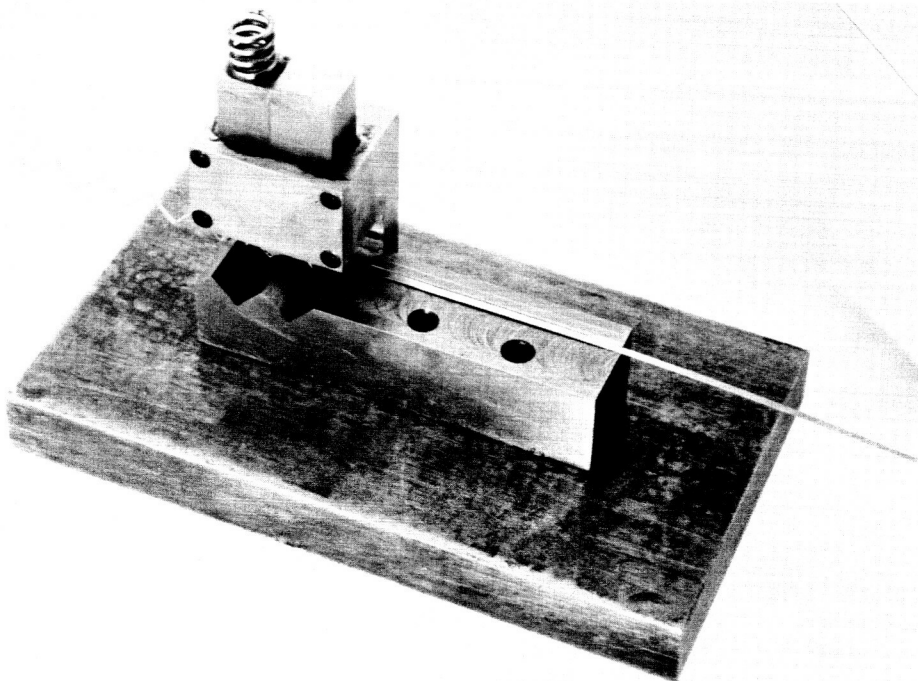
FIGURE 50. WEB-CORRUGATION DIES

25915
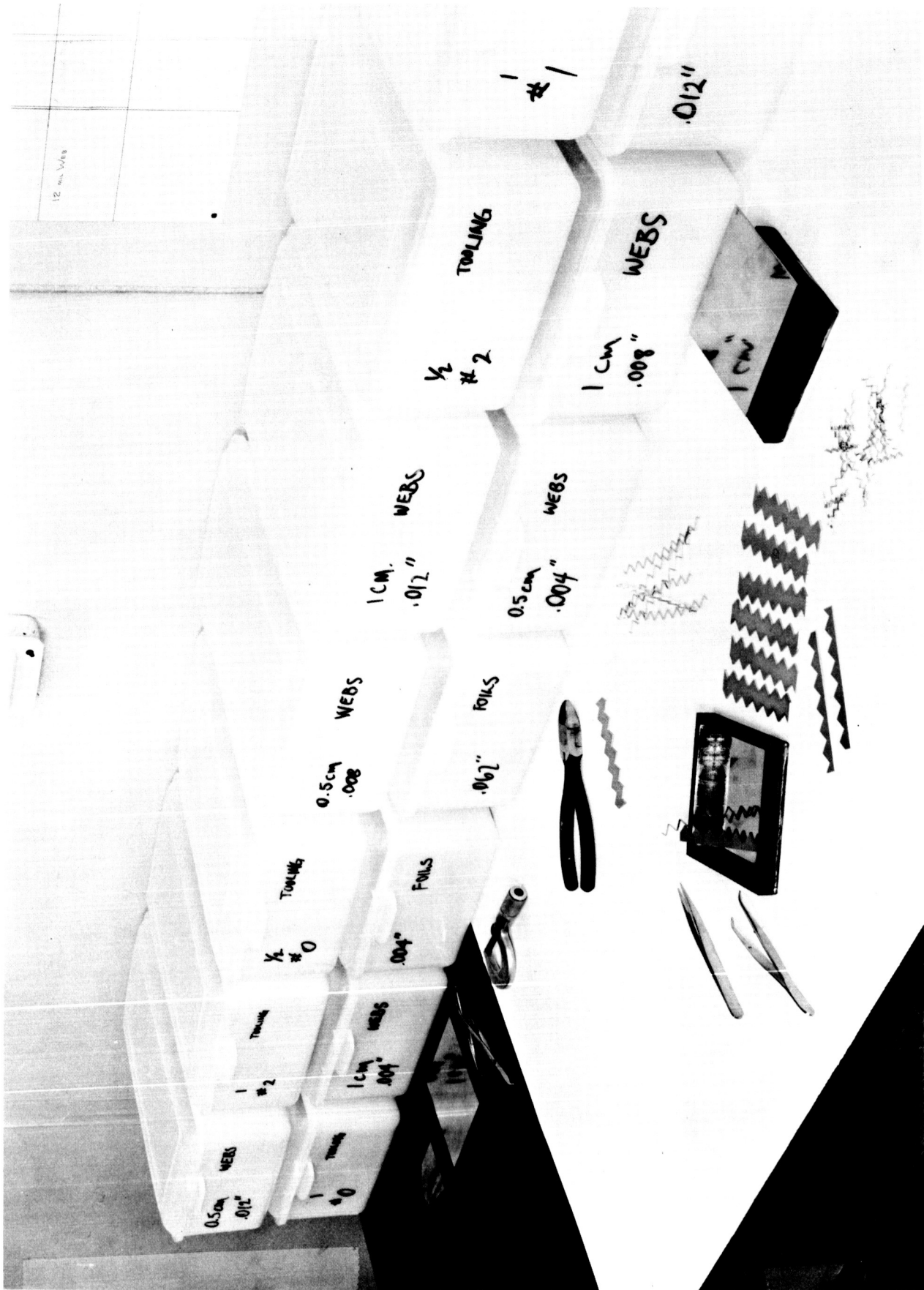
FIGURE 51. INSULATION ASSEMBLY TABLE
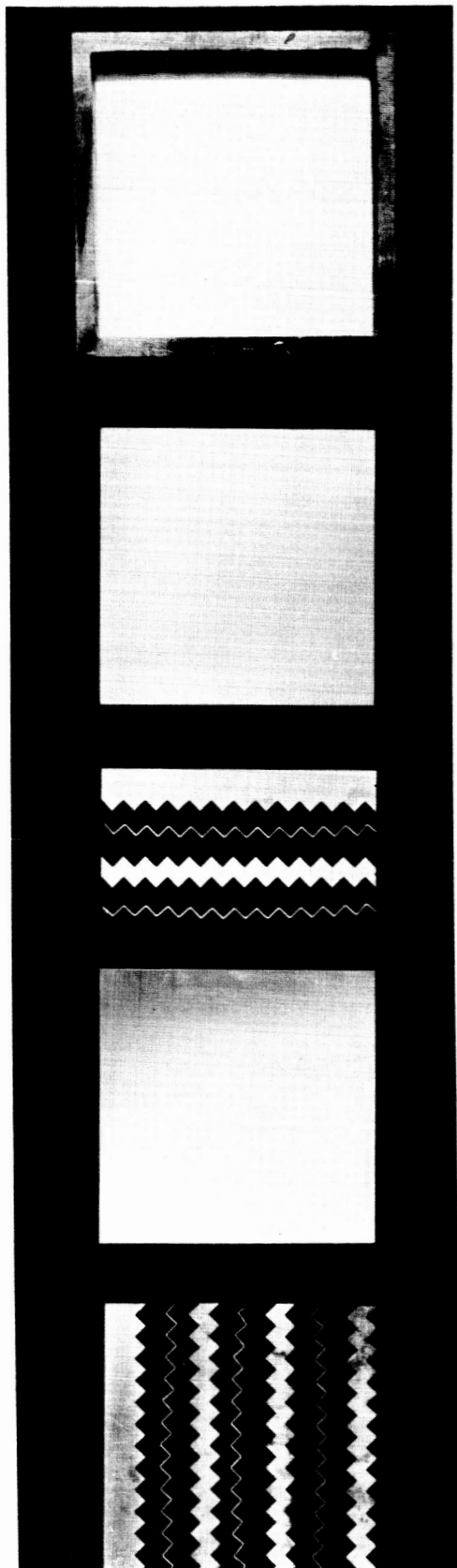
~1/2 size

25916

FIGURE 52. PICTURE-FRAME CAN AND INSULATION COMPONENTS IN THE SEQUENCE OF ASSEMBLY

Finishing Operations

After bonding, the corners were cut from the insulation structures, yielding additional insulation pieces which were used for metallurgical and surface finish evaluation. All structures were machined to a 3-in.-diameter disc, and faced on a lathe, with the filler tooling still in place. Thermocouple grooves, to be used later in thermal testing, were milled in the upper and lower 1/16-inch cover plates of each structure prior to the leaching operation.

Removal of the Filler Tooling. The nickel-plated iron tooling was removed from the Hastelloy C structures with a solution consisting of 50 parts nitric acid and 50 parts water, heated to 170 F. When required, the structures were depassivated in a dilute sulfuric acid-water solution to hasten the leaching operation. Notably, the small web-bend-length structures required more time in the acid than did the longer bend-length structures. The corner sections appeared more reflective than the disc structures because the corners were in the acid less than one hour during leaching, whereas the full-sized structures required from 3 to 6 days in the acid depending upon web-bend length.

Specimen Evaluation. Inspection of the finished structures revealed that the inner surfaces were moderately reflective. A typical insulation structure is pictured in Figure 53. The insulation structures were X-rayed before leaching. X-radiographs revealing the correct internal geometry are shown in Figure 54. It was noted that in some structures, primarily those with the shorter web-bend lengths, some of the webs in adjacent layers were not positioned over each other as designed. It was believed that the web shifting, which was at most only two web thicknesses, would not appreciably affect the results of either the structural or the thermal tests.

Metallurgical examination was made of the bond zones where the webs join the foils. As shown in the photomicrograph enlargement, Figure 55, some upsetting of the webs occurred as desired. Bonding was accomplished although some inclusions are evident at the bond interface. It is believed that these inclusions have no detrimental effect on the bond strength as discussed in the structural testing section below.

Testing of Insulation Structures

The test program was composed of two phases, thermal testing, and structural testing. The latter phase is divided into compression testing and shear testing. Table 4 is a tabulation of the test plan for the insulation structures as well as an identification chart for the insulation dimensions. In the case of structures undergoing both thermal and structural tests, the thermal tests were performed prior to the structural tests.

Structural Testing

Structural testing was conducted to determine the mechanical behavior of the insulation with regard to load-bearing capability, mode of deformation, and recoverability. Compression tests were conducted by loading the structures in a direction
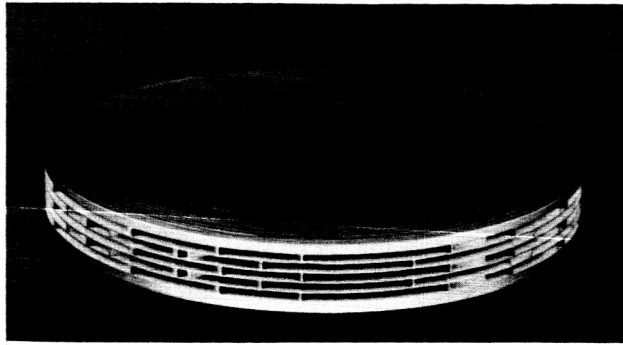
26239

FIGURE 53. STRUCTURAL INSULATION SPECIMEN
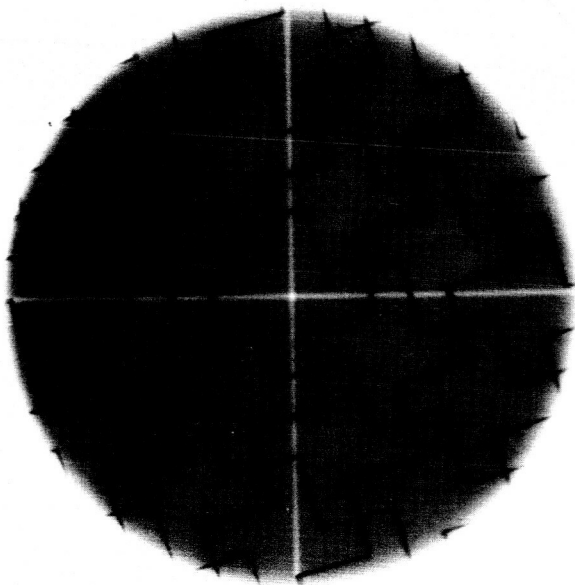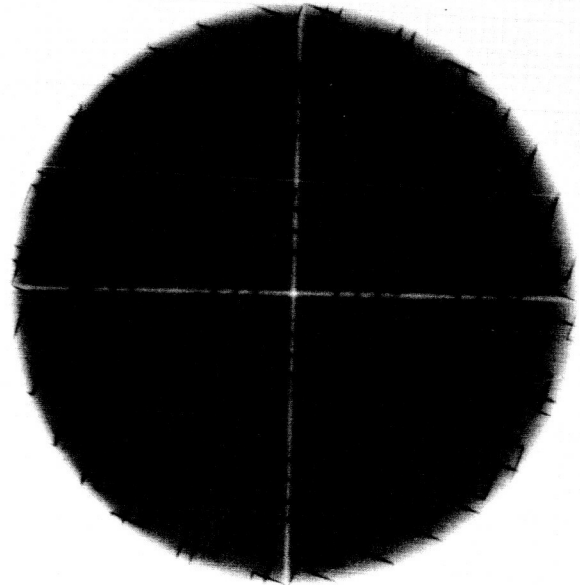
Specimen No. 1   Specimen No. 11

FIGURE 54. TYPICAL SPECIMEN X-RAYS

Web

Foil
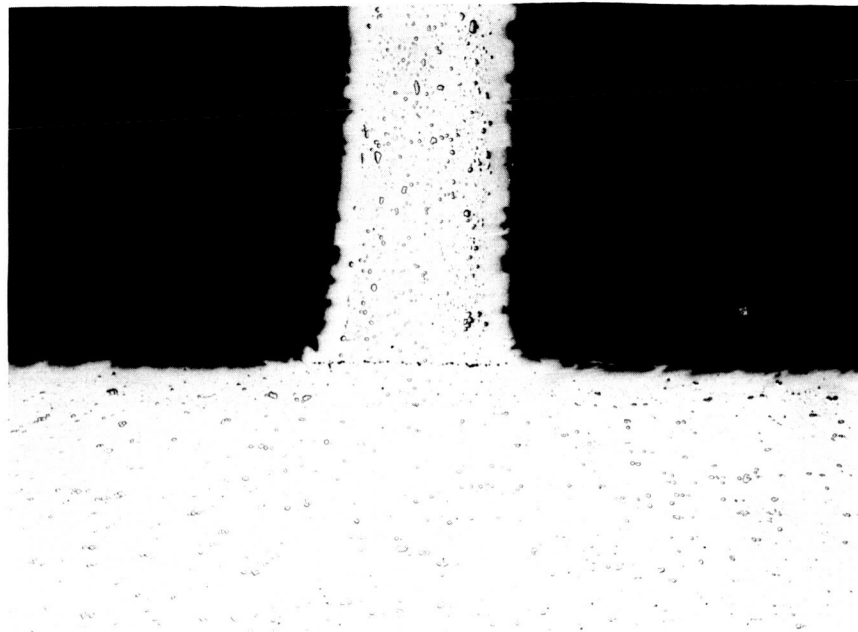
Rm45676

FIGURE 55. WEB-FOIL BOND

TABLE 4. TESTING PLAN

Thermal	Test Compression	Shear	Insulation Structure			
			Web+	Foil+	Type*	Number
	X		12	12		1
	X		12	8	1	2
	X		12	4		6
X	X		4	12		15
	X		12	12		7
	X		12	8	1/2	8
X	X		12	4		9
	X		4	12		13
X		X	8	8		4
X		X	4	4	1	17
		X	8	4		5
		X	4	8		16
X		X	8	8		11
X		X	4	4	1/2	18
		X	8	4		12
		X	4	8		14
			8	12	1	3
			8	12	1/2	10

+ Numbers denote thickness of member in mils.
* 1 denotes 1-cm web bend length.
   1/2 denotes 1/2-cm web bend length.

perpendicular to the plane of the foils. Shear tests were performed by forcing relative motion of the end plates in a direction parallel to the foils. All tests were conducted using an Instron Universal Testing Machine in a helium atmosphere at 1700 F. A constant loading speed of 0.005 inch per minute was used for both the compression and shear tests.

Control Samples. Before testing the insulation structures, tensile tests were conducted on "control" samples of Hastelloy C to determine the actual yield strength of the material. Four specimens of as-received material (AR) and four specimens of material subjected to the gas-pressure-bonding process (B) were pulled to failure at a constant rate of 0.005 in./min at 1700 F in a helium atmosphere. Load-time curves were recorded as each test was being conducted. The results are the following:

(1) For both AR and B, YS = 0.9 US*

(2) For AR, the average YS = 18 KSI

(3) For B, the average YS = 16 KSI.

At this temperature, Haynes Stellite literature presents a yield strength of 26 KSI (interpolated) for Hastelloy C sheet. Thus, the yield strength of the material is about 35 percent lower than that reported by the manufacturer. Apparently, the pressure-bonding process had no severe effect on the Hastelloy strength properties although both the yield strength and the ultimate strength of the pressure-bonded material were lower by approximately 10 percent than those of the as-received material. For use in the analysis presented below, 16 KSI was taken as the yield strength of Hastelloy C, in tension and compression, at the operating temperature of 1700 F (1200 K).

Compression Testing. The compression tests were performed by deforming the structures at a constant rate and measuring the force exerted by the structures. The compression grips are pictured in Figure 56. The behavior of the structure is characterized by an initial region where load is proportional to deformation followed by a yield point where deformation proceeds with little load increase. The Type 1/2 structures demonstrate a single yield point while the Type 1 structures have multiple yield points. This is illustrated qualitatively in Figure 57. Figure 58 is a photograph showing the deformation patterns common to both the Type 1 and Type 1/2 structures. Structure 13 was an exception to this mode of deformation. For this structure, all the 4-mil webs were completely folded (accordion style) leaving the foils relatively undeformed.

The yield load, P, shown in Figure 57 is of particular interest because below this load the structures recover elastically as proved by unloading cycles which were performed on Structures 7 and 13. Structure 7 was loaded to 350 pounds, completely in the elastic portion of the load curve, and showed complete recovery upon removal of the load. Specimen 13 was loaded to 1150 pounds, the region where yielding was imminent, and showed 95 percent recovery of load upon subsequent reloading to the yield point. The compressive deformation at the yield point was approximately 50 percent of the web height, H, for the Type 1/2 specimens. The experimental yield loads, P, are tabulated in Table 5.

---

*YS = yield stress; US = ultimate stress.

Water-cooled
upper grip

Specimen

Lower grip
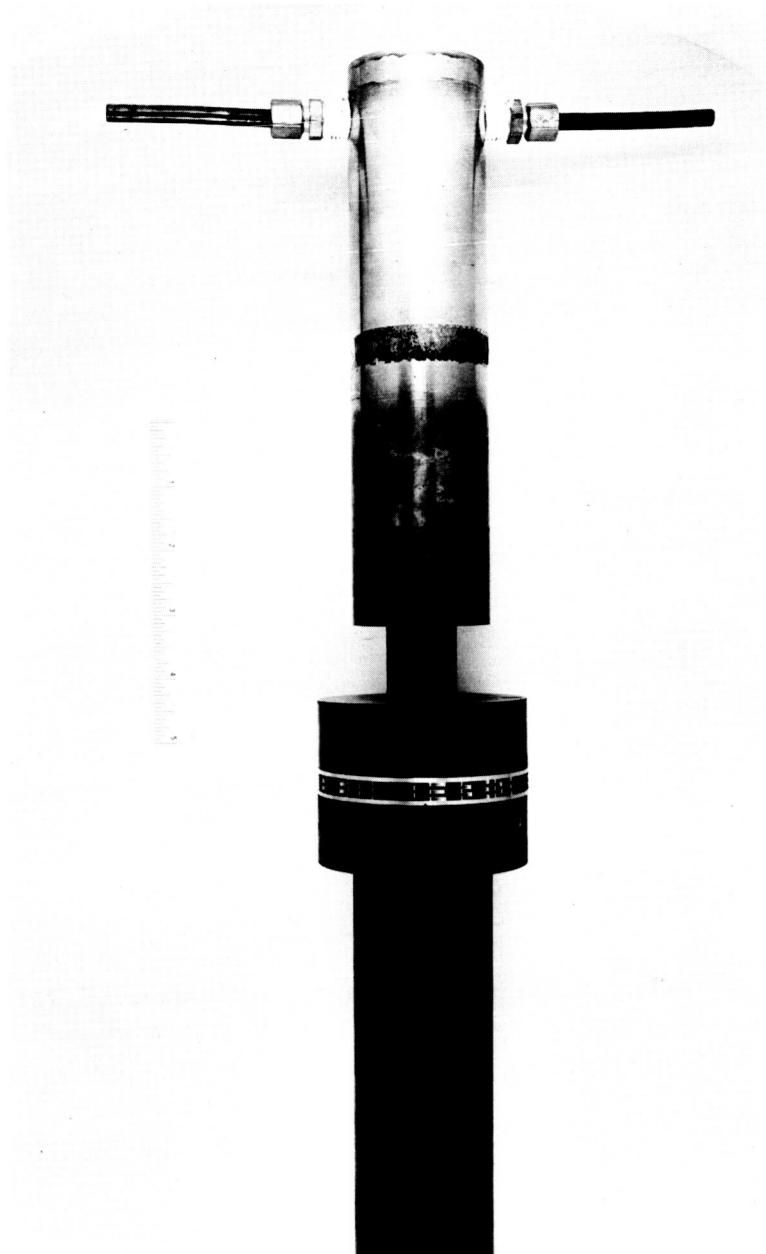
RM47106

FIGURE 56. COMPRESSION GRIPS
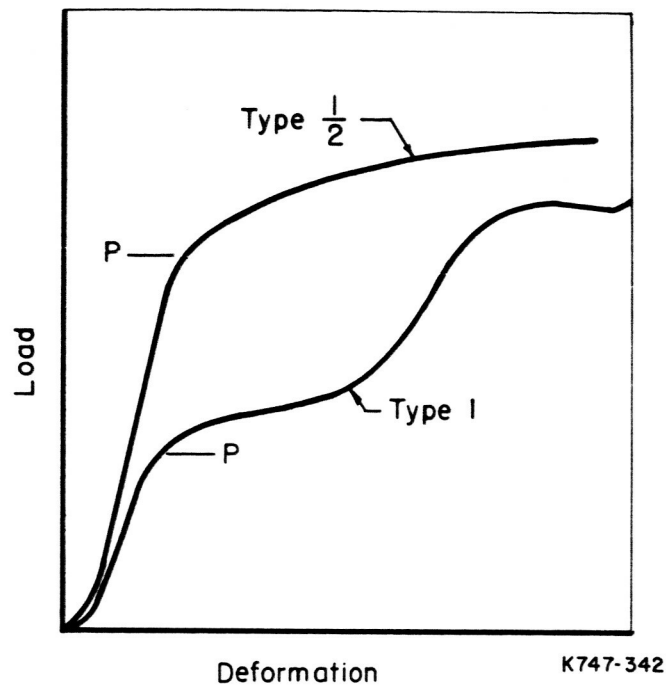
FIGURE 57. COMPRESSIVE LOADING CHARACTERISTICS
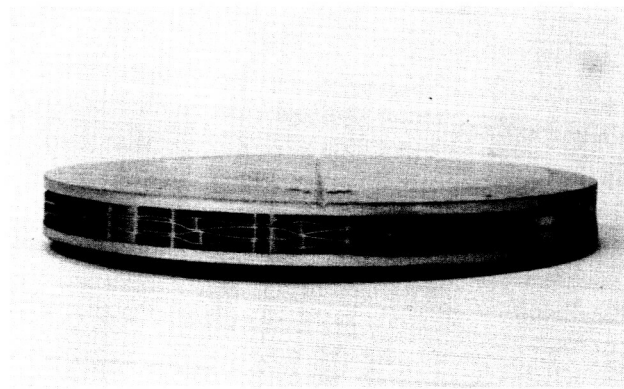
29855

TYPE 1   TYPE 1/2

FIGURE 58. DEFORMATION MODES IN COMPRESSION

TABLE 5. COMPRESSION TEST DATA*

Structure No.	Type	t, mil	f, mil	Measured Yield Load, lb
1	1	12	12	800
2	1	12	8	460
6	1	12	4	300
15	1	4	12	250
7	1/2	12	12	2500
8	1/2	12	8	1800
9	1/2	12	4	1250
13	1/2	4	12	1150

*1700 F helium atmosphere.

Conclusions which may be drawn from the results of the compression tests are the following:

(1) The Hastelloy C insulation structures are capable of supporting substantial compressive stresses at temperatures up to 1700 F. For example, the gross stress for Structure No. 7 was greater than 350 psi.

(2) The structures fail at a definite load by yielding. Some exhibit multiple yield points.

(3) When stressed below the yield load, the structures recover elastically with no permanent set if the load is removed.

(4) The deformation accumulated when the structures first start to yield is approximately 10 percent of the total insulation thickness.

Shear Testing. The shear tests were conducted under the same conditions as those stated above with the exception that the deformation rate of 0.005 in. per min. is now a relative shear motion in the plane of the end plates. The shear grips are shown in Figure 59 in both the assembled and the disassembled condition. The data for these tests are presented in Table 6. The load deflection curves for the shear structures show an almost linear increase of load with deformation up to a sharp yield point where load drops off suddenly. Elastic recovery was not investigated for the shear structures. The mode of deformation in the shear structures is dependent on the relative size of the webs and foils. For specimens with thin foils and webs, post-test examination revealed that the internal structure was completely deformed (see Figure 60a). This was not the case for structures with thick foils and webs where, subsequent to yielding, the mode of failure was severance of the bonds between the webs and foils, Figure 60b. The average relative displacement of the end plates at yielding was approximately 0.04 in. for the Type 1 specimens and 0.05 in. for the Type 1/2 specimens.
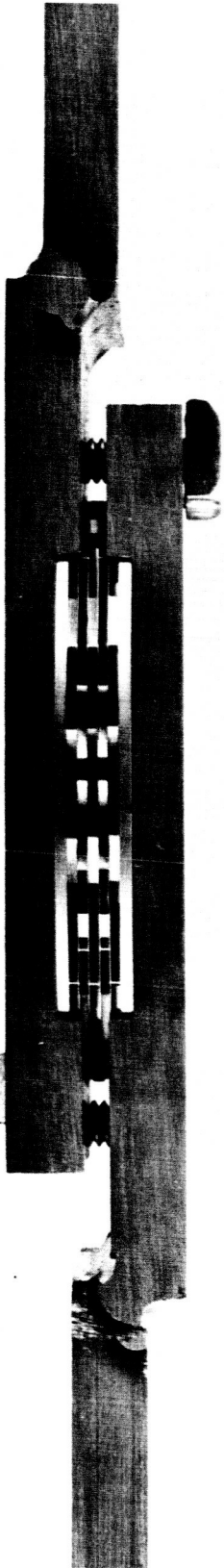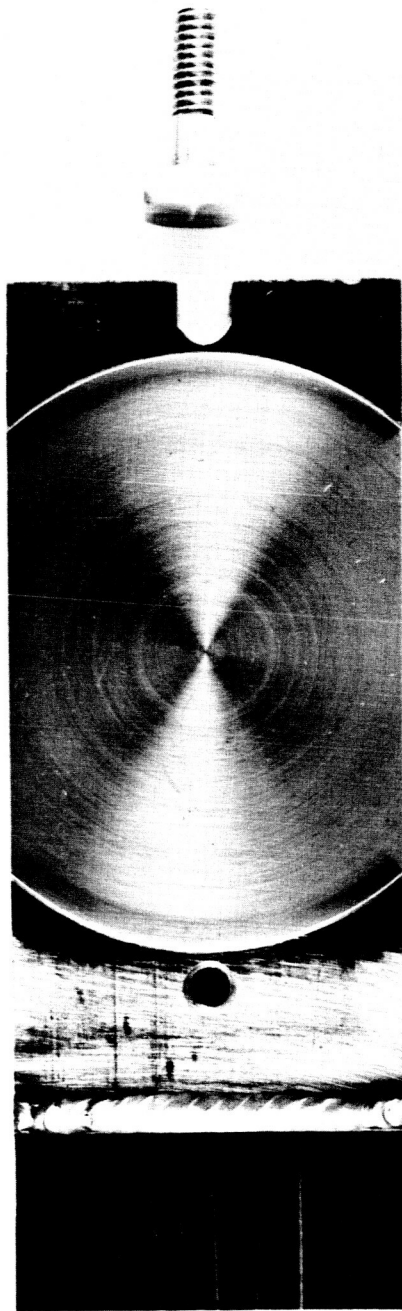
Assembled RM46665   Disassembled   RM46664
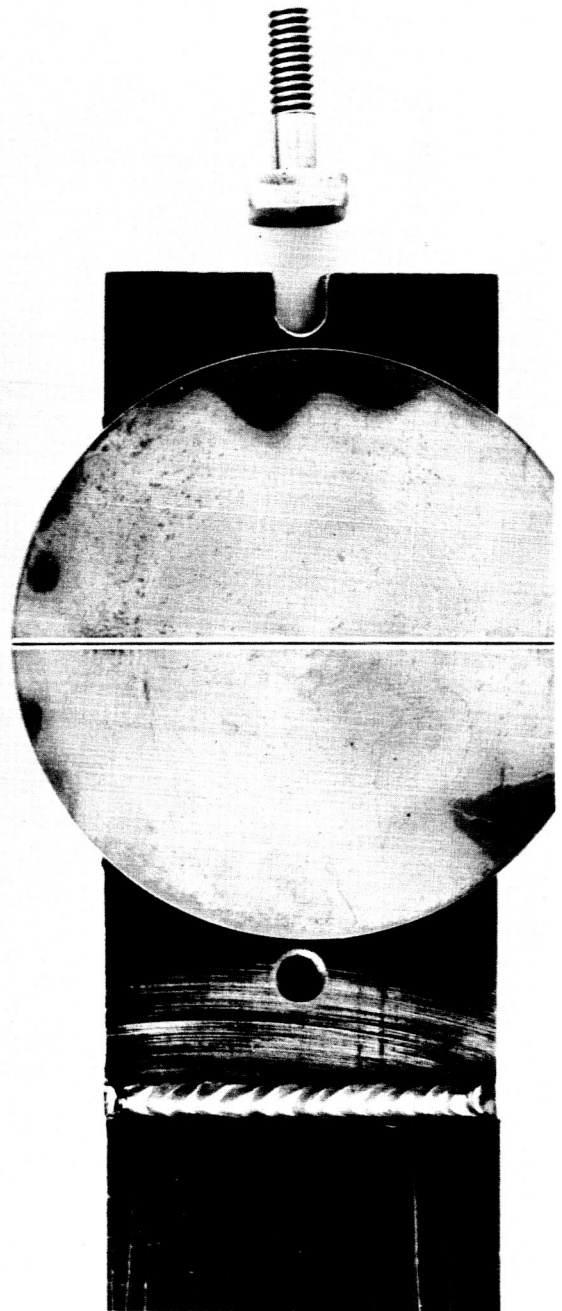
FIGURE 59. SHEAR GRIPS
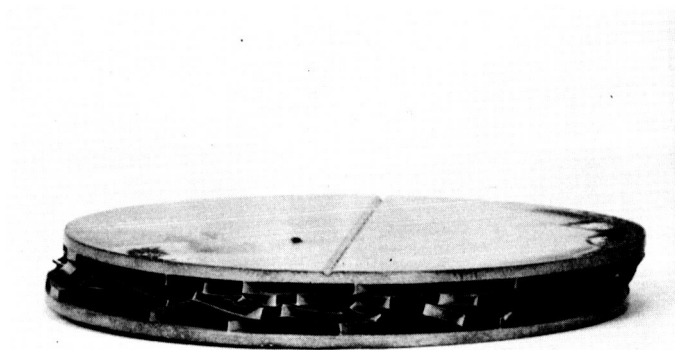
29856

(a) Light Structure – Thin Webs and Foils
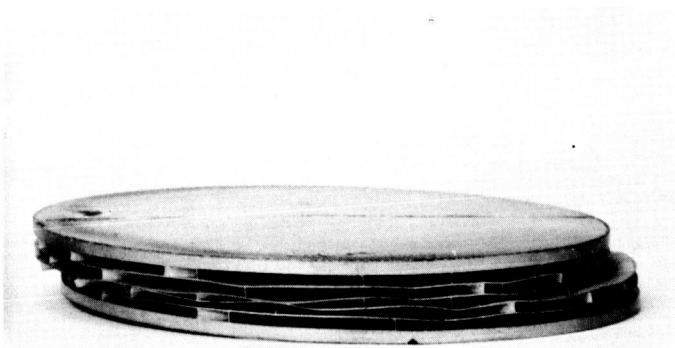
29856

(b) Heavy Structure – Thick Webs and Foils

FIGURE 60. DEFORMATION MODES IN SHEAR

TABLE 6. SHEAR TEST DATA*

Structure No.	Type	t, mil	f, mil	Measured Yield Load, lb
4	1	8	8	800
5	1	8	4	370
17	1	4	4	275
16	1	4	8	495
11	1/2	8	8	900
12	1/2	8	4	470
18	1/2	4	4	375
14	1/2	4	8	580

*1700 F helium atmosphere.

A bonding factor (BF) may be calculated based on the bond severance of Structures 11 and 14 immediately after yielding. If uniform loading is assumed over the entire web area,

$$\frac{\text{Imposed load}}{A_{gross}} = \frac{A_{webs}}{A_{gross}} \, \sigma_{shear\ bonds} \ .$$

From the repeating section,

$$\frac{A_{webs}}{A_{gross}} = \frac{4\ Lt}{4\ L^2} = \frac{t}{L} \ .$$

Thus, the shear stress at the bonds may be calculated if no stress concentration factors are considered. The bonding factor is defined as

$$BF = \frac{\sigma_{shear-bond}}{\sigma_{shear-material}} \ .$$

If the shear strength of the material is assumed to be half the tensile strength, the bonding factors calculated by this method are 0.4 and 0.5 for Structures 11 and 14, respectively. This indicates that a stress concentration factor of approximately 2 is present or that the bonds are only half as strong as the material. Due to the complex geometry, the presence of stress concentrations is inevitable. It is therefore concluded that stress concentration is the cause of bond severance and the actual bonding factor is close to 1.

Conclusions which may be drawn from the results of the shear tests are the following:

(1) The Hastelloy insulation structures are capable of supporting applied shear stresses of up to 125 psi at temperatures of 1700 F.

(2) The structures fail at a definite load, which is quite close to the ultimate load attainable by yielding.

(3) The lateral deformation accumulated when the structures first start to yield is of the order of the web height and is approximately 20 percent of the total insulation thickness.

(4) In structures characterized by thick webs and foils, loading beyond the yield point will produce bond failure due to stress concentration. The bonding factor calculated at this point is close to 1.

Thermal Testing

Thermal testing was performed by measuring the equilibrium heat flow through the insulation while subjecting the insulation to constant hot- and cold-side temperatures. For use in the analysis presented below, emittance measurements were also performed on sections of the insulation.

Thermal Tests. The thermal test equipment is schematically illustrated in Figure 61. The test apparatus essentially consists of an electrical heater (4), a heat meter of calibrated material (10), a vacuum chamber, associated foil insulation (2, 5, 6), guard cylinders (14), and temperature-measuring thermocouples. The heat generated by the heater passes through the specimen, then through the heat meter and out of the system via a cooling sink. Thermal guarding is afforded by the large specimen size and the guard cylinders. The imposed temperatures were measured with very fine gauge Chromel Alumel thermocouples flash welded to the center of the 1/16-inch end plates of the insulation structures.

When equilibrium was attained, the following measurements were recorded:

T_h — temperature on hot side of structure

T_c — temperature on cold side of structure

Q — heat flux at steady state through the central, self-guarded section of the insulation.

The thermal test data are presented in Table 7 in the sequence that the measurements were taken. More equilibria were taken on Structures 4 and 11 because these were the first structures to be tested of each type. A typical data plot, for Structure 11, is presented in Figure 62. In viewing the graph, one must keep in mind that the results are for insulation structures having five layers only. Furthermore, the ΔT across the structure at each data point in the figure is different, thus the points should not be expected to lie on a single curve. The data show a more than linear increase in Q with increasing temperature. This is due to the radiant heat-transfer contribution to heat flow through the insulation.

Negligible distortion of the structures due to internal thermal stresses could be detected. A vacuum of 10^{-5} torr was maintained during testing. Nevertheless, some of the initially shiny surfaces emerged darkened from the test apparatus. After Equilibrium 13, Structure 4 was removed from the test rig severely blackened. This is attributed to contamination within the apparatus. The structure was vacuum heat treated, restoring the initial bright surface and reinstalled for Equilibria 14 through 18.

1. Stainless steel container
2. Heat radiation shields
3. Water-cooled heater leads
4. Molybdenum sheet heater
5. Heat radiation shields
6. Stainless steel radiation pellets
7. Small control heater
8. Heat diffusion block
9. Specimen
10. No. 347 stainless steel standard heat meter
11. Heat sink
12. Thermocouples
13. Vacuum line
14. Guard cylinders
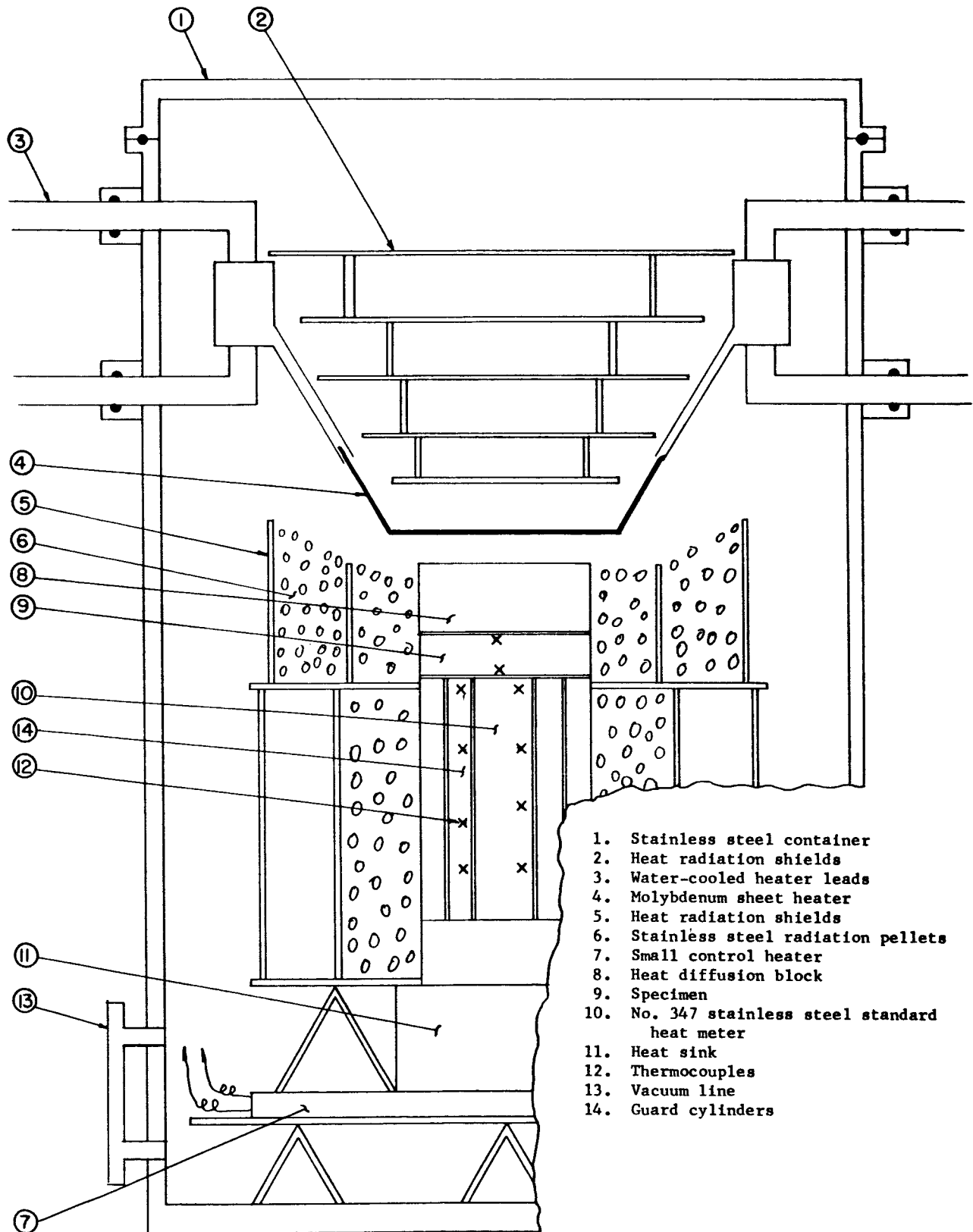
FIGURE 61. THERMAL TEST APPARATUS

TABLE 7. THERMAL TEST DATA

Insulation Structure No.	Equilibrium Designation	Temperature, K		Measured Heat Flux, Q watts/in.^{2}
		T_h	T_c	
4	1	523	497	0.417
	2	526	499	0.461
	3	726	671	1.190
	4	904	823	2.300
	5	555	526	0.466
	6	1042	928	3.500
	7	1167	1033	5.380
	8	1285	1112	7.400
	9	577	536	0.850
	10	673	615	1.370
	11	550	490	0.917
	12	437	401	0.453
	13	598	527	1.130
	14	804	739	1.040
	15	815	773	0.797
	16	1200	1094	4.450
	17	1206	1043	4.070
	18	829	745	1.780
11	1	526	512	0.433
	2	665	642	0.905
	3	793	757	1.324
	4	957	897	2.955
	5	880	830	2.272
	6	1042	967	3.928
	7	1033	965	3.804
	8	1253	1135	7.570
	9	822	784	1.693
	10	837	809	0.933
	11	1196	1116	4.734
	12	1197	1072	7.237
17	1	822	701	0.916
	2	826	748	0.719
	3	1194	1061	3.540
	4	1193	979	4.569
18	1	818	755	1.308
	2	831	789	0.786
	3	1207	1090	3.624
	4	1185	1017	5.421
9	1	824	777	1.602
	2	823	784	1.160
	3	1200	1116	4.474
	4	1197	1075	7.561
15	1	822	712	1.207
	2	816	759	0.587
	3	1207	1096	5.420
	4	1215	1017	5.811
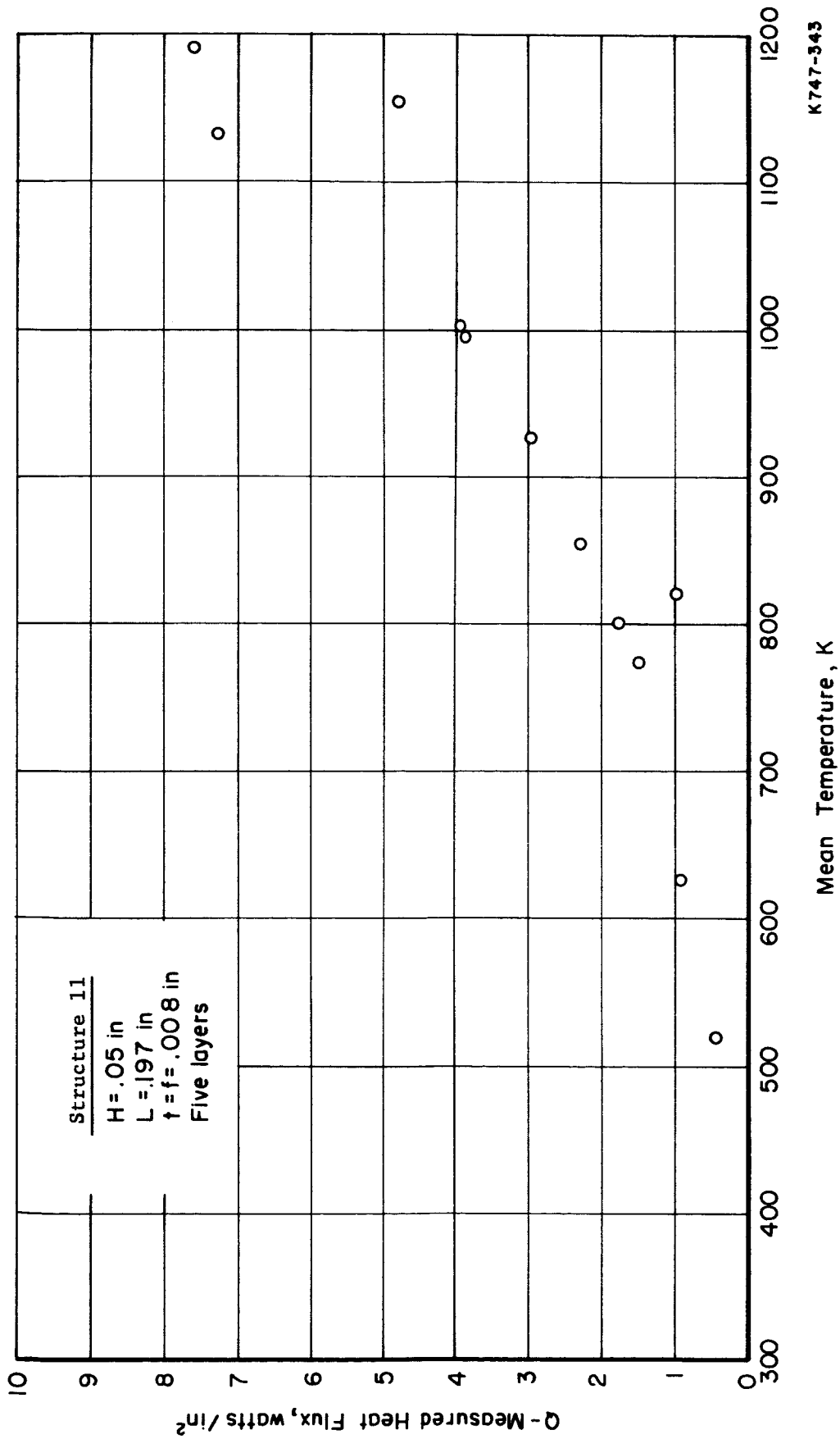
FIGURE 62. MEASURED HEAT FLOW VS TEMPERATURE

K747-343

After testing, the structure again emerged darkened. Structures 11 and 18 emerged clean while the remaining structures showed various degrees of tinting or darkening when examined after testing.

Emittance Tests. The hemispherical total emittance was measured as a function of temperature for pieces of foil removed from three different corner sections of the insulation and two strips of acid-leached as-received material. One strip of as-received material was acid soaked for three days, the other for six days, corresponding to the leaching times for the long web-bend length (Type 1) and the short web-bend length (Type 1/2) insulation structures, respectively.

The test results indicate there is a variance in data for both the foil pieces and strips; however, all the foil pieces demonstrate higher emittance values than the as-received material. If the data at significant temperatures are averaged, a trend indicating increasing emittance with temperature is revealed. This is shown in Figure 63. The roughness of the foil sections (RMS microinches) is a factor of four higher than that of the strip material as indicated on the figure. In general, higher surface roughness is associated with higher emittance values in the range of RMS values indicated. Therefore, the actual foil emittance should be considered higher than that of the strip material because of the higher RMS values. However, the true emittance of the foils will be lower than the measured values because removal from the corner sections damaged areas on the foils. These damaged areas show up as thermally black regions.

For use in the analysis presented below, the insulation surface emittance is taken as a linear variation from 0.27 at 500 K to 0.355 at 1200 K as shown by the solid line in the figure. From the previous description of the structures after thermal testing, these emittance values obviously are not representative of actual surface conditions during testing; however, these values will be used for initial comparison purposes in the following section.

Correlation and Analysis of Data

This section describes the correlation of experimentally obtained information with analytical predictions.* The purpose of the correlation is to revise the analytical expressions, where necessary, to achieve accurate description of insulation performance.

Structural

Revised expressions describing the insulation structural performance are presented in Equations 3 and 6. These expressions replace Equations 1 and 4 in that the effect of varying the foil thickness is accounted for. The material properties have been extracted and the constants remaining in the expressions are only a function of the unique geometry of the structures and the web height.

---

*Final Report of NASA Contract NAS5-3697 classified Confidential, Restricted Data, Report No. BAT-5-3697-2.
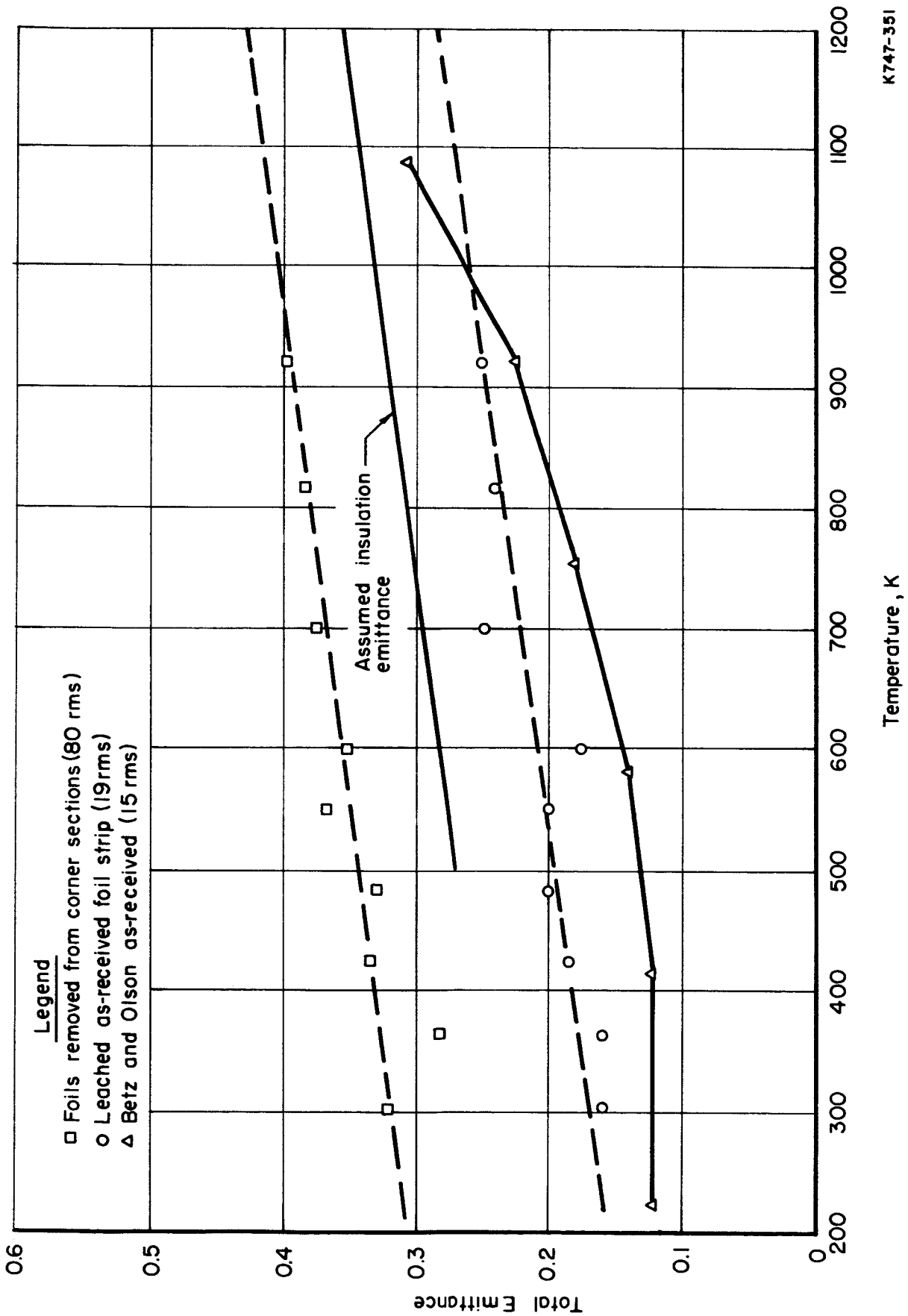
FIGURE 63. HEMISPHERICAL TOTAL EMITTANCE

Legend
□ Foils removed from corner sections (80 rms)
○ Leached as-received foil strip (19 rms)
△ Betz and Olson as-received (15 rms)

Assumed insulation emittance

Total Emittance

Temperature, K

K747-351

Compression. The analytical expression* for predicting the sustainable compressive yield load (P_c) for an insulation structure is

$$P_c = \frac{(AREA)\, \sigma_{M-C}}{L/t} \qquad (1)$$

where

σ_{M-C} = the yield strength in compression of Hastelloy C at the appropriate temperature

L/t = the web-bend length to web-thickness ratio.

The ratio of web thickness to web height is assumed to be such that buckling of the webs will not occur before direct yielding. The test results substantiate this assumption, for gross buckling did not occur before local yielding. Equation 1 is optimistic in that uniform load distribution is assumed for the webs in any given layer. Thus, the foils are considered rigid and the foil thickness, f, does not appear in the expression. Using Equation 1, the experimental yield loads are compared with the calculated yield loads, P_c in Table 8. From the significant difference between the values, one may readily conclude that the load distribution is far from uniform. Furthermore, the foil thickness directly affects the strength. This is illustrated by the experimental data for Structures 1, 2, and 6. The web thickness is a significant parameter as seen from the tests of Structures 7 and 13, where the sustained yield load was halved by decreasing the web thickness by a factor of 3. The Type 1/2 series, small L structures, are substantially stronger by comparison to the Type 1 structures.

TABLE 8. COMPRESSION TEST LOAD COMPARISON

Insulation Structure	Type	Web+	Foil+	Yield Load, lb	
				Measured, P	Calculated, P_c*
1	1	12	12	800	3450
2	1	12	8	460	3450
6	1	12	4	300	3450
15	1	4	12	250	1150
7	1/2	12	12	2500	8900
8	1/2	12	8	1800	8900
9	1/2	12	4	1250	8900
13	1/2	4	12	1150	2300

+ Numbers denote thickness of member in mils.

*σ_{M-C} = 16 KSI.

The yield load can be most conveniently expressed by the function of the insulation parameters shown in Figure 64. The yield load varies linearly with the quantity $t^{1.05} f^{0.95}/L^{1.25}$ for the two L values studied. If a linear variation of the ordinate intercept with L is assumed, the equation describing the compressive yielding of the insulation structures is

*Final Report of NASA Contract NAS5-3697 classified Confidential, Restricted Data, Report No. BAT-5-3697-2.
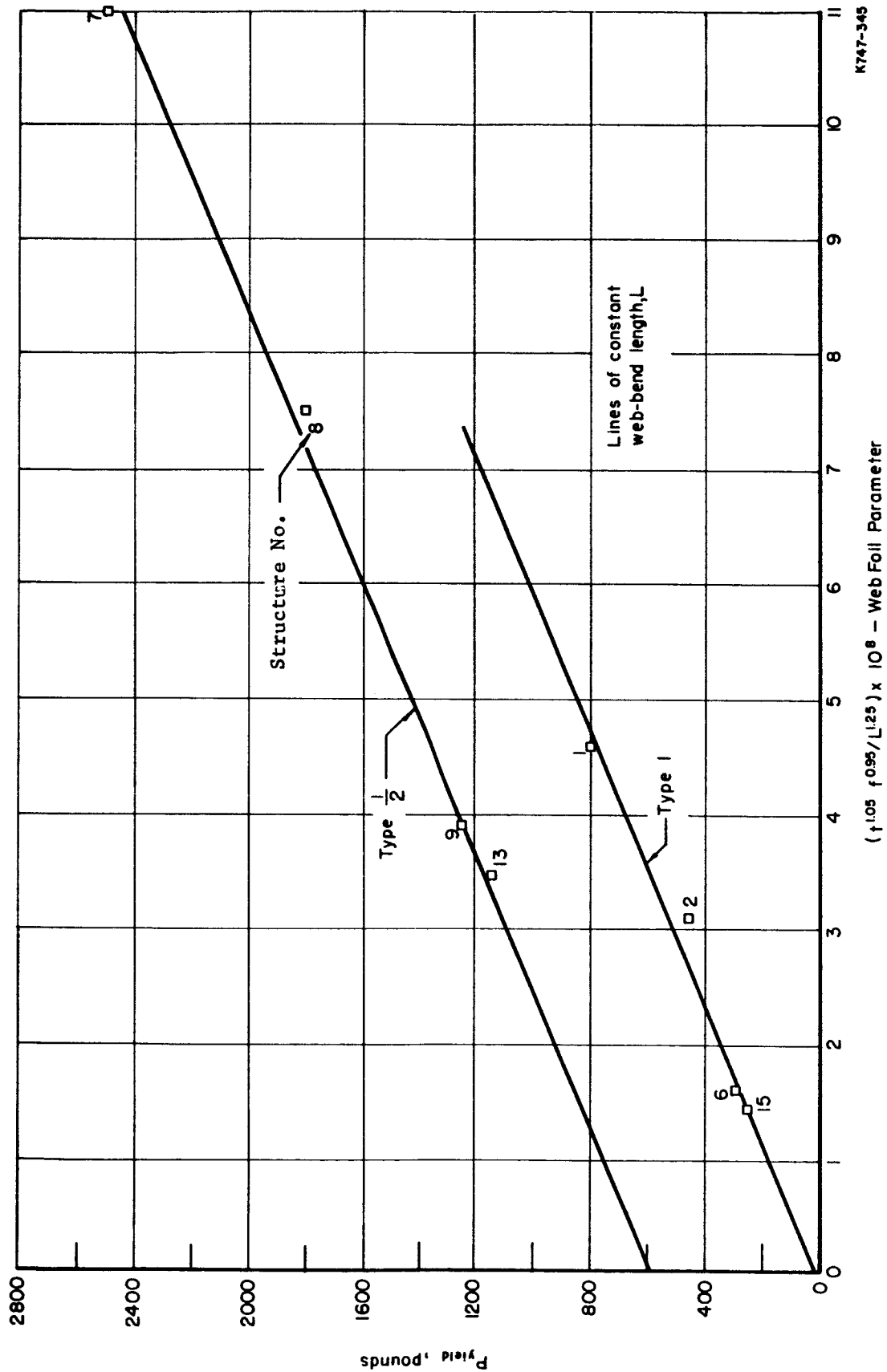
FIGURE 64. COMPRESSION-LOADING PERFORMANCE FUNCTION

K747-345

BATTELLE   MEMORIAL   INSTITUTE

$$P_c = (1200 - 3047\,L) + (171.4 \times 10^8)\, t^{1.05} f^{0.95} / L^{1.25} \quad , \qquad (2)$$

where

P_c = yield load, lb

t, f, and L are given in inches

Specimen area = 7.07 in.^{2} .

The constants in the expression have dimensional units because the web height, H, the specimen area, and the materials properties are inherent in the expression. Since the relation describes only the yield load and not structural deformation, the expression will not include the elastic modulus of the material. Since the load supported will be directly proportional to the gross specimen area and the material strength, the expression may be divided by the product of the structure area and the Hastelloy C yield strength (7.06 in.^{2} x 16,000 lb/in.^{2}). This gives

$$\frac{\sigma_I}{\sigma_{M-C}} = 0.0107 - 0.0272\,L + (15.29)\, t^{1.05} f^{0.95} / L^{1.25} \quad . \qquad (3)$$

where

σ_I / σ_{M-C} = ratio of the compressive yield strength of the structural insulation to the yield strength of the insulation material is compression.

It should be noted that the expression breaks down for values of L, t, or f approaching zero or infinity. Physically the insulation would lose its configuration if this were the case. In choosing values for the insulation dimensions, for use in Equation 3, care must be taken to preserve the insulation geometry with regard to ratios of the parameters H/L, L/t, and t/H. These ratios varied within the ranges listed below for the structures evaluated in this program.

Ratio	Maximum Value	Minimum Value
H/L	0.25	0.125
L/t	100	17
t/H	0.24	0.08

Shear. The analytical expression* for predicting the sustainable yield load, P_s, for an insulation structure is

$$P_s = \frac{(AREA)\,(BF)\, \sigma_{M-S}}{2\,L/t} \quad , \qquad (4)$$

where

σ_{M-S} = the yield strength in shear of Hastelloy C at the appropriate temperature

---

*BAT-5-3697-2.

BF = the bonding factor or the efficiency of the bond between the webs and foils

L/t = the web-bend length to web-thickness ratio.

The expression is independent of the direction of the applied shear load with respect to the direction of the web bends. This is accounted for by the 2 in the denominator which renders only half the actual web area effective in resisting shear loads. The assumption of uniform stress distribution to the webs in any given layer is also implied.

Table 9 shows the measured yield load and the yield load calculated from Equation 4. The results are similar to compression test data in that it is observed that the foil thickness and web-bend length are important parameters. For both the shear and compressive modes of loading, smaller web-bend lengths result in stronger structures. The effect is twofold. Firstly, the net-web area is increased if L is decreased for the same web thickness and foil thickness. Secondly, by decreasing L, the total number of web bends and intersections is increased, thus tending to make the structure more rigid.

TABLE 9. SHEAR TEST LOAD COMPARISON

Insulation Structure	Type	Web+	Foil+	Yield Load, lb	
				Measured, P	Calculated, P_s*
4	1	8	8	800	572
5	1	8	4	370	572
17	1	4	4	275	286
16	1	4	8	495	286
11	1/2	8	8	900	1044
12	1/2	8	4	470	1044
18	1/2	4	4	375	572
14	1/2	4	8	580	572

+ Numbers denote thickness of member in mils.

* σ_{M-S} = 8 KSI; BF = 1.

As described for the compression tests, the yield load may be related to the insulation parameters by a suitable combination function. This functional relation is shown in Figure 65. The yield load varies linearly with the parameter combination $(t^{0.75} f^{1.25})$ for the two values of L considered. If again a linear variation of ordinate intercept with L is assumed, the equation describing the shear yielding of the insulation structures is

$$P_s = (300 - 507.6 \text{ L}) + (10.94 \times 10^6) \, t^{0.75} f^{1.25} \quad , \qquad (5)$$

where

P_s = yield load, lb

t, f, and L are given in inches

Structure area = 7.06 in.^{2}.
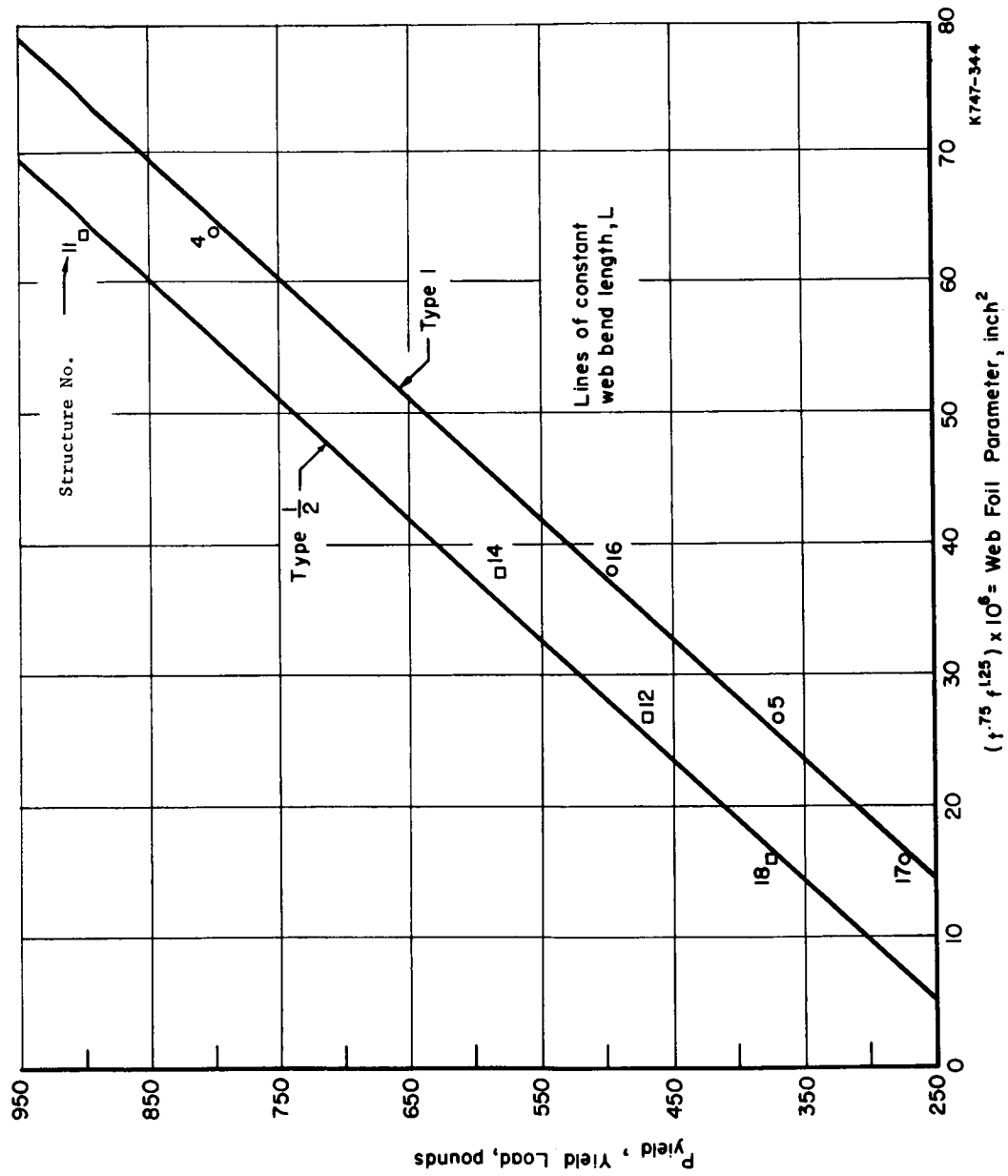
FIGURE 65. SHEAR-LOADING PERFORMANCE FUNCTION

Again, this may be reduced to a general expression by extracting the area and material shear strength. If the shear strength is taken to be half the measured tensile strength, the relation for the shear strength becomes

$$\frac{\sigma_I}{\sigma_{M-S}} = 0.00536 - 0.00907 \, L + 195.4 \, (t^{0.75} f^{1.25}) \ . \tag{6}$$

where

σ_I/σ_{M-S} = the ratio of the shear yield strength of the structural insulation to the yield strength of the insulation material in shear.

The remarks regarding the choice of insulation dimensions for Equation 3 are equally applicable to Equation 6.

Thermal

A first approximation to calculate the heat flux through the insulation, for given materials properties and temperature conditions, is to linearly sum the conductive and radiative contributions. From previous work*, the proposed relation is:

$$q = \frac{1}{n} \left[\frac{k_{eff} \, (T_h - T_c)}{H + f} + S \, F(T_h^4 - T_c^4) \right] \ . \tag{7}$$

where

q = the calculated heat flux per unit area,

n = the number of web layers,

$$k_{eff} = k \left[\frac{H + f}{\dfrac{L^2}{3f} + \dfrac{L(H + f)}{t}} \right] , \tag{8}**$$

where

S = Stephan-Boltzmann's constant,

F = radiation factor, taken as $\dfrac{\epsilon}{2 - \epsilon}$ for infinite parallel plates,

and

ϵ = hemispherical total emittance of the Hastelloy C

k = the material thermal conductivity, that of Hastelloy C.

The first term within the bracket of Equation 7 represents the contribution to heat flow by conduction through the webs and foils. The complex conduction path is expressed in terms of an effective thermal conductivity, k_{eff}, which allows the insulation to be treated as a homogeneous material. It is seen from Equation 7 that the total heat flow varies inversely with n. This is because the web height is a constant and adding layers increases the thickness of the insulation while at the same time introducing additional radiation shields.

---

*BAT-5-3697-2.

**The omission of a 2 above the 3 in Equation 8 is a correction of Equation 20, p 60, as given in BAT-5-3697-2.

If the conductivity and emittance of the Hastelloy C are known as a function of temperature, predicted values of q may be calculated for each equilibrium test point. The thermal conductivity of as-received Hastelloy C, a solution-quenched alloy, is presented in Figure 66. Above 850 K there is a steep rise in conductivity due to precipitation within the material. Values along the curve are not valid with decreasing temperature when the precipitation temperature has been exceeded. In the pressure-bonding operation, the insulation structures were slow cooled from a temperature of 1360 K and precipitation did occur (see Figure 55). Therefore, a curve such as A-B was assumed for the variation of the Hastelloy conductivity with temperature. Without extensive testing, the actual slope or shape of the curve is not precisely known, however, it is believed that the conductivity values given by Curve A-B (drawn parallel to C-D) are sufficiently correct to allow meaningful evaluation of thermal test data.

Using the values of emittance given in Figure 63 and the assumed thermal conductivity variation given by Line A-B, Figure 66, calculated values for heat flux may be compared with the measured values. This comparison is presented in Table 10 where the measured data are denoted by Q and the calculated by q. The percent difference between the two values is also presented.

From the comparison, it is seen that for each structure at least one equilibrium exists where the percent difference exceeds 20 percent. For Structure 4, the majority of differences exceed this value. From previous discussion relating to post-test specimen appearance and emittance measurements, it is known that the emittance, ϵ, used in Equation 7 is subject to variation. Such variations of surface radiative properties during testing are not uncommon, as discussed by J. C. Richmond* of the National Bureau of Standards. An example is cited where oxide films, formed upon heating a specimen of Inconel in a good laboratory vacuum (about 10^{-5} torr), markedly affected the total hemispherical emittance. Variations in emittance from 0.46 to 0.75 were readily obtained with temperature cycling conducted below 1200 K. With this in mind, Euqation 7 was used to calculate an effective operating emittance, ϵ_{eff}, by substituting the actual value, Q, for the heat flux in the equation. Thus, ϵ_{eff} as tabulated in Table 10, represents the insulation-operating emittance for perfect correlation between measured heat flow and calculated heat flow. Extreme values of emittance, 1.00 or 0.0, shown in the table may be excused by recalling that the Hastelloy thermal conductivity values are not precise.

From the results of the calculations, the following observations regarding ϵ_{eff} may be made:

> Structure 4 – emittance very high
> Structure 11 – emittance correct as assumed
> Remaining structures – emittance initially low and increases to
> relatively high values.

The sequence of testing and the discussion of post-test structure appearance indicate that the above variance of ϵ_{eff} is certainly to be expected.

---

*Richmond, Joseph, C. , "Importance of Surface Films".
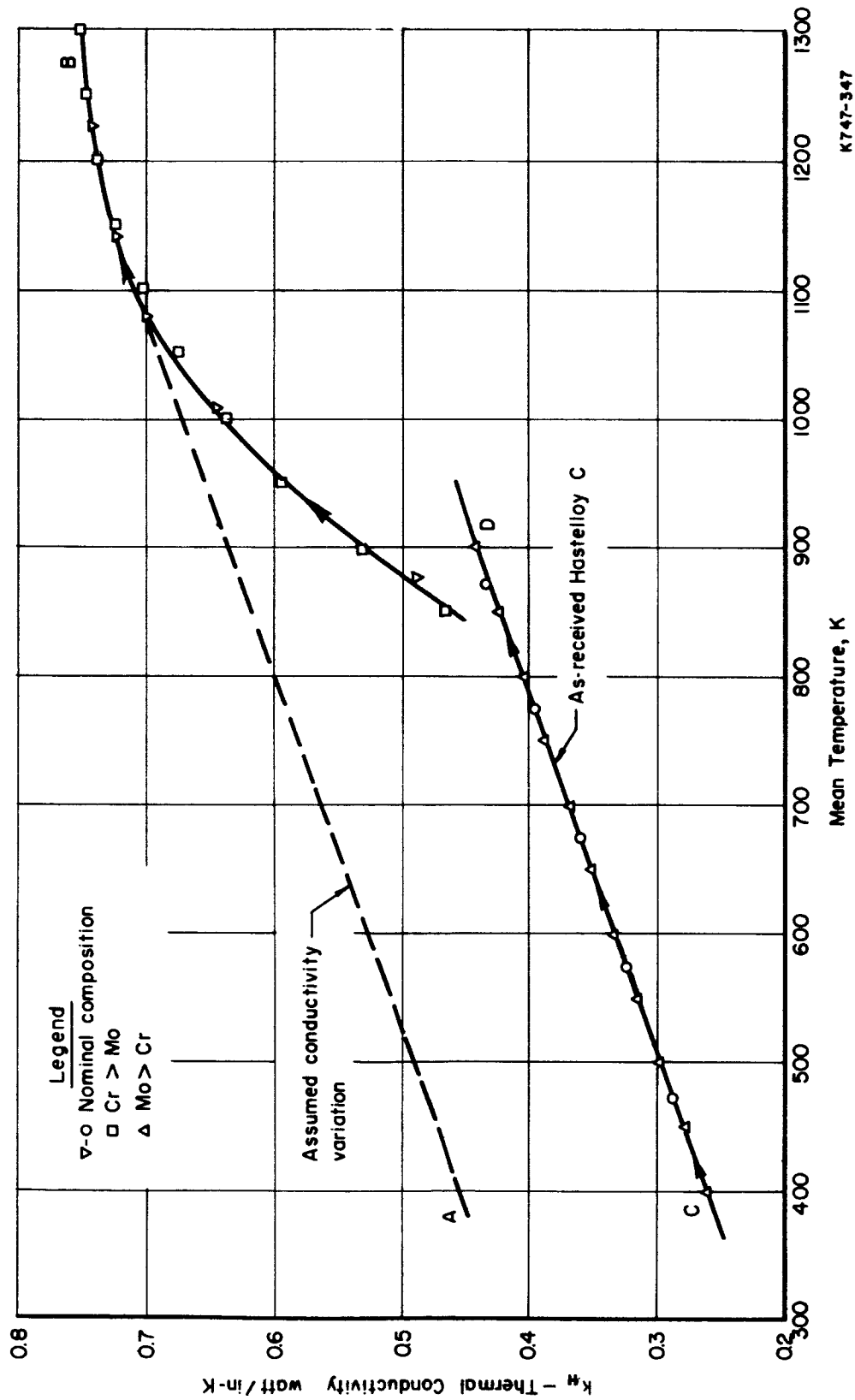
FIGURE 66. THERMAL CONDUCTIVITY OF HASTELLOY C VS TEMPERATURE

K747-347

TABLE 10. HEAT FLOW COMPARISON

Insulation Structure No.	Equilibrium Designation	Heat Flux – Watts/in.^{2}		Percent Difference	ϵ_{eff}
		Measured, Q	Calculated, q		
4	1	0.42	0.29	30	1.00
	2	0.46	0.30	34	1.00
	3	1.19	0.76	36	0.98
	4	2.30	1.37	40	0.88
	5	0.47	0.35	26	1.00
	6	3.50	2.70	23	0.62
	7	5.38	3.13	42	0.78
	8	7.40	4.66	37	0.68
	9	0.85	0.49	43	1.00
	10	1.37	0.75	45	1.00
	11	0.92	0.68	26	1.00
	12	0.45	0.37	19	1.00
	13	1.13	0.84	26	0.97
	14	1.04	0.98	6	0.43
	15	0.80	0.65	18	0.59
	16	4.45	2.65	40	0.74
	17	4.07	4.06	0	0.35
	18	1.78	1.30	27	0.74
11	1	0.43	0.43	0	Correct as
	2	0.91	0.85	6	assumed,
	3	1.32	1.46	11	Figure 63
	4	2.96	2.80	6	
	5	2.27	2.18	4	
	6	3.93	3.73	5	
	7	3.80	3.37	12	
	8	7.57	6.97	9	
	9	1.69	1.58	7	
	10	0.93	0.78	28	
	11	4.73	4.58	3	
	12	7.24	7.01	3	
17	1	0.92	1.04	13	0.18
	2	0.72	0.70	3	0.30
	3	3.54	2.21	38	0.61
	4	4.57	3.29	28	0.53
18	1	1.31	1.41	8	0.13
	2	0.79	0.96	22	0.00
	3	3.62	3.90	8	0.32
	4	5.42	5.36	1	0.36
9	1	1.60	1.46	9	0.52
	2	1.16	1.22	5	0.13
	3	4.47	3.75	17	0.57
	4	7.56	5.32	29	0.78
15	1	1.21	1.47	32	0.00
	2	0.59	0.83	21	0.00
	3	5.42	2.68	50	0.86
	4	5.81	4.57	21	0.52

In the case of the first measurement, insulation Structure No. 4, the test apparatus was severely contaminated as mentioned in the "Thermal Testing" section above. This is consistent with the values of ϵ_{eff} (see Table 10). The structure was heat treated following Equilibrium 13. For Equilibrium 14, the "clean" structure resulted in only 6 percent difference in heat flows with the accompanying lower value of ϵ_{eff} of 0.43. It is seen that upon continued exposure in the test rig, the percent differences and effective emittance values began to rise in Equilibria 15, 16, and 17. The structure was again observed to be blackened upon removal from the rig.

Following the test of Structure 4, the rig was recleaned and baked out. For the succeeding structure, 11, there is excellent agreement between measured values and calculated values. Here the emittance values were identical with those given in Figure 63. At the conclusion of the test, Structure 11 emerged unblackened.

After testing Structures 4 and 11, attempts were made to achieve higher temperature differences across the insulation structures by lowering the contact resistance at the heat sink. It is assumed that the test apparatus was again contaminated since the remaining structures were blackened.

Because of the consistent and predictable variation of surface emittance in structures other than No. 11 and the excellent prediction of heat flow throughout the 500 K to 1200 K temperature range for Structure 11, it appears that Equation 7 is valid for calculating the heat flux through the insulation.

Parametric Display of Performance Data

The equations presented in the "Correlation and Analysis" section together with an expression for describing insulation weight may be graphically displayed in terms of the insulation parameters and material properties. The three factors of interest are weight, strength, and heat flow.

Weight

The total thickness of the insulation is the product of the number of layers and the thickness of each layer. Thus,

$$\text{Thickness} = n(H + f) \ . \tag{9}$$

The weight may be expressed in terms of an effective density of the structure, ρ_{eff}, defined by

$$\rho_{eff} = \rho \left[\frac{\text{Volume of Metal}}{\substack{\text{Unit Volume of} \\ \text{Insulation Structure}}} \right] = \rho \left[\frac{Lf + Ht}{L(H+f)} \right] \tag{10}$$

where ρ is the actual material density. The weight per unit area of n layers is then

$$W = n(H + f) \rho_{eff} = \rho n \left[f + \frac{Ht}{L} \right]$$

or

$$\frac{W}{\rho n} = f + H(t/L), \quad \frac{lb/in.^2}{layer - lb/in.^3} \qquad (11)$$

The equation is plotted in Figure 67. The curve may be used to conveniently obtain insulation weight when the material density, number of layers, and internal dimensions are known.

Strength

Equations 3 and 6 express the ratio of insulation compressive and shear strength to material strength. These equations in terms of the insulation internal dimensions are plotted in Figures 68 and 69, respectively. The resultant nomographs are to be used as indicated by the heavy lines where values of web thickness, foil thickness, web-bend length, and the ratio of insulation yield strength to material yield strength are related. In Figure 68, a horizontal transfer from the first family of L curves to the second family is required. The horizontal transfer can occur either to the left or to the right.

Thermal

Equation 7, describing the heat flow through the insulation, may be rewritten as follows.

$$Q_{TOTAL} = \frac{a \ k \ \Delta T}{n} \left[\frac{1}{\frac{1}{2} \left(\frac{L^2}{f} \right) + \left(\frac{L}{t} \right) H + \left(\frac{L}{t} \right) f} \right] + \frac{a}{n} \left(\frac{\epsilon}{2 - \epsilon} \right) S \left(T_h^4 - T_c^4 \right) \quad (12)$$

where $\Delta T = T_h - T_c$ and a is the insulation area.

A heat conduction parameter, H_c, and a heat radiation parameter, H_r, may be defined as follows.

$$H_r \equiv \left(\frac{\epsilon}{2 - \epsilon} \right) S \left[\frac{T_h^4 - T_c^4}{T_h - T_c} \right] . \qquad (13)$$

$$H_c \equiv \frac{1}{\frac{1}{2} \left(\frac{L^2}{f} \right) + \frac{L}{t}(H) + \frac{L}{t}(f)} . \qquad (14)$$

From Equation 14, let

$$A \equiv \frac{1}{2} \frac{L^2}{f}$$
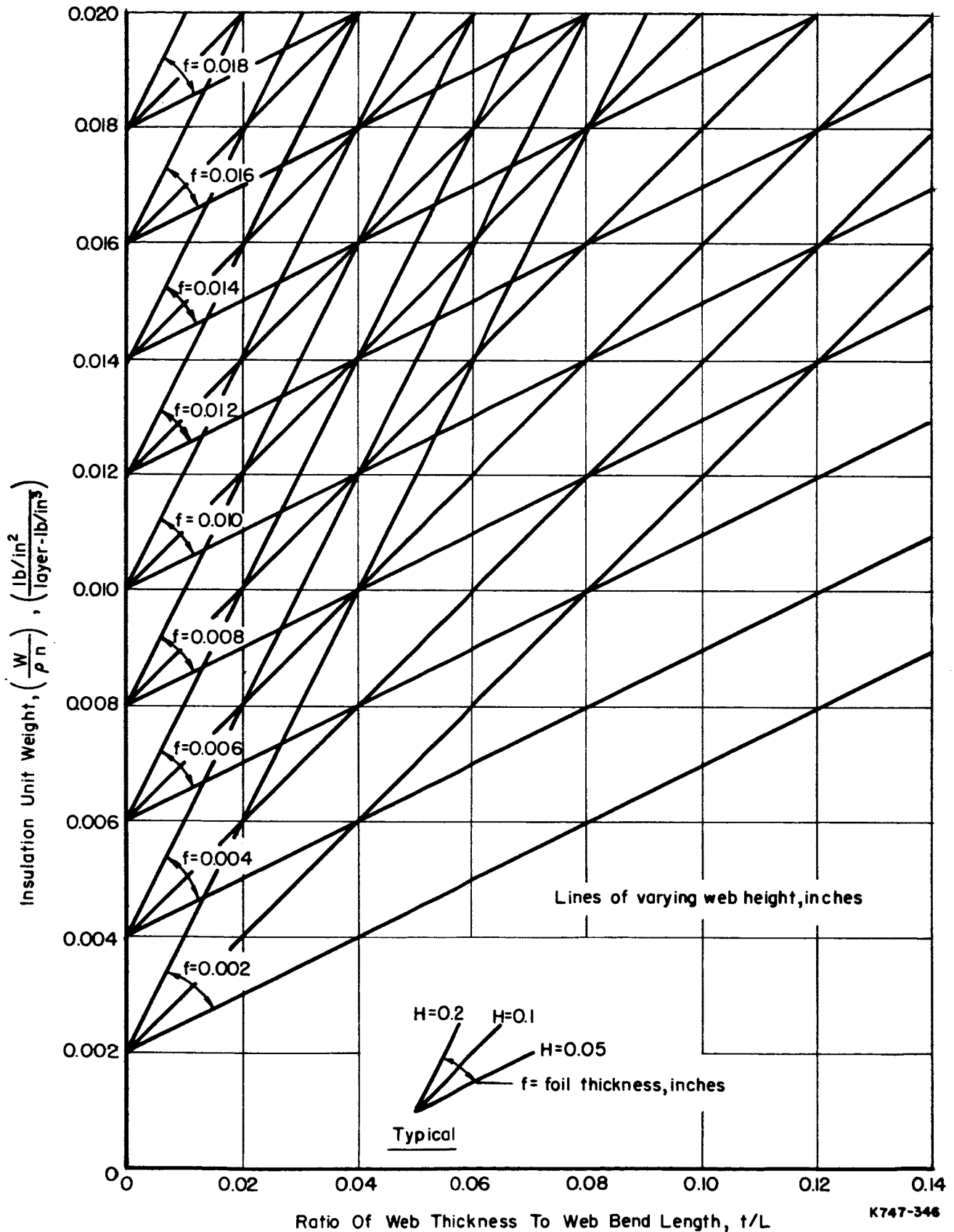
FIGURE 67. INSULATION UNIT WEIGHT

BATTELLE MEMORIAL INSTITUTE
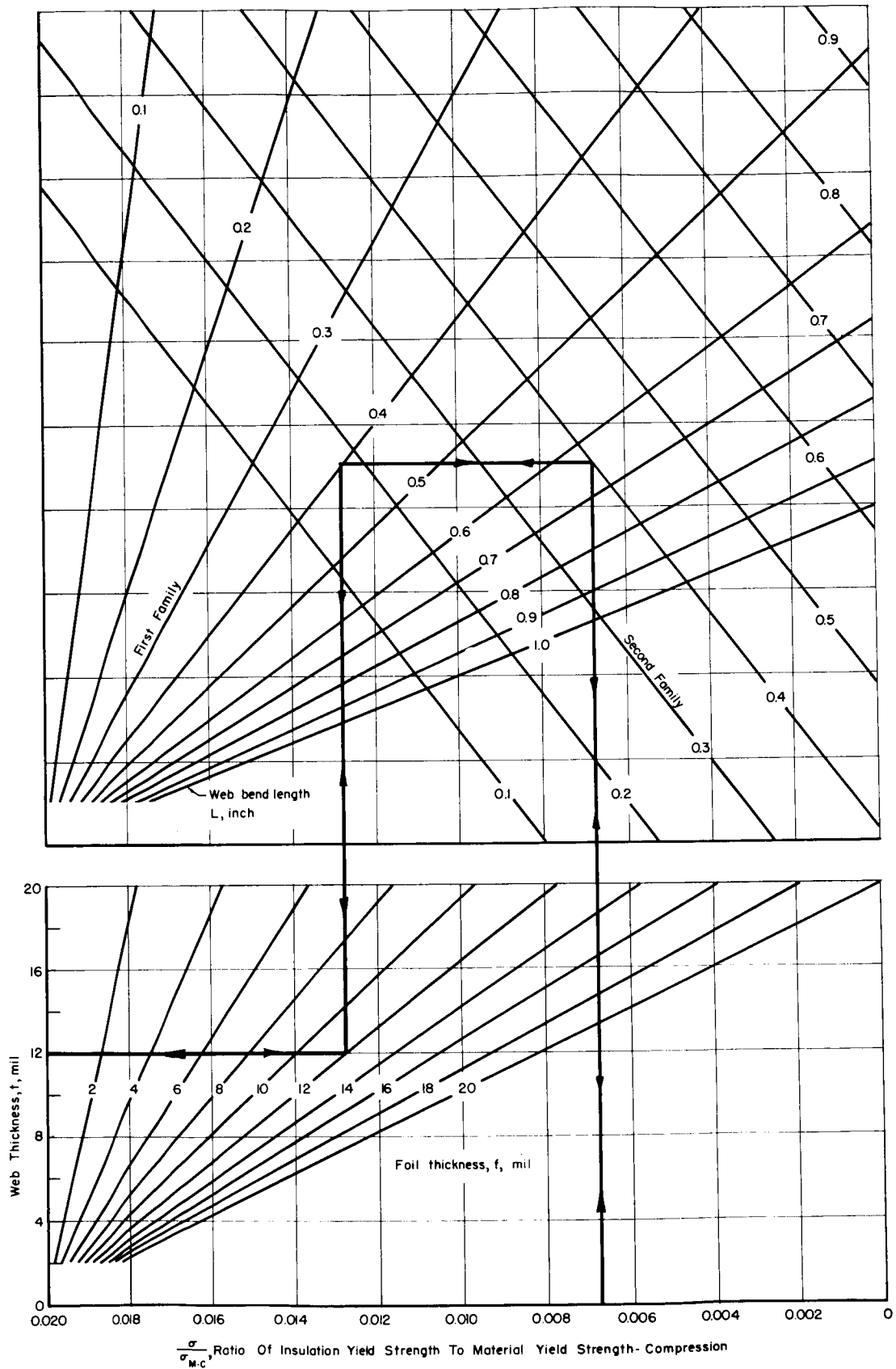
FIGURE 68. STRUCTURAL INSULATION COMPRESSIVE STRENGTH
BATTELLE   MEMORIAL   INSTITUTE
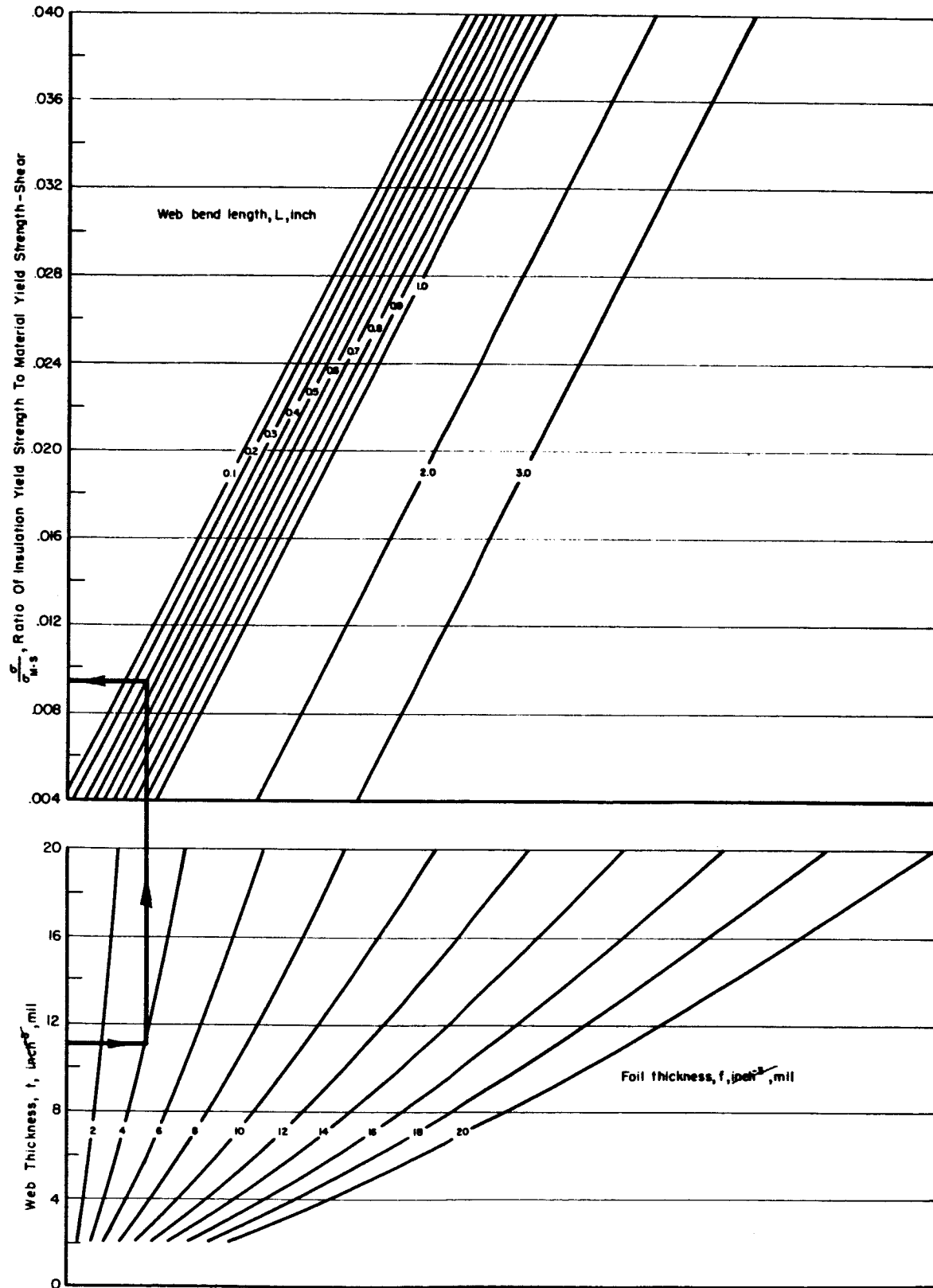
FIGURE 69. STRUCTURAL INSULATION SHEAR STRENGTH

$$B \equiv \frac{L}{t}(H)$$

$$C \equiv \frac{L}{t}(f)$$

$I \equiv A+B+C.$ Then

$$H_c = \frac{1}{I} . \tag{15}$$

Substituting the expressions for H_c and H_r in Equation 12 and rearranging gives

$$q_{TOT} = \frac{\Delta T}{n}\left[k\, H_c + H_r\right] . \tag{16}$$

where q_{TOT} is the total heat flow per unit area.

To calculate the heat flow through the insulation, Equation 16 is used once the heat-transfer parameters, H_c and H_r, are determined. The parameter H_c is only a function of the insulation internal dimensions. Figure 70 is used to obtain H_c once A+B+C, defined as I, is known. The quantity A is found from Figure 71. Both B and C may be determined from Figure 72 by using the ratio L/t and either the web height, H, to get values of B or the foil thickness, f, to get values for C. The parameter H_r, a function of emittance and operating temperatures of the insulation, is obtained using Figure 73 as indicated by the heavy line. For comparison purposes, an over-all effective conductivity, K, may be deduced from Equation 16.

$$q_{TOT} = \frac{K\,\Delta T}{thickness} = \frac{K\,\Delta T}{n(H+f)} . \tag{17}$$

Substituting Equation 16 in Equation 17 gives K in terms of H_c and H_r.

$$K = (H+f)\left[k\, H_c + H_r\right] . \tag{18}$$

Values of K calculated from Equation 18 have the same meaning as thermal conductivity for homogeneous materials.

Evaluation

Evaluation of insulation performance may be made by computing the effective thermal conductivity, strength, and the weight of selected insulation structures using the equations and design curves developed in the preceding section. Table 11 presents these computations for Structures 17, 7, 4, and 11. Structures 17 and 7 represent extremes of strength, weight, and thermal losses for the configurations tested. Structures 4 and 11 represent mid-range performance. Hastelloy C properties used in the computation are consistent with observed test results in this program where:

Emittance ≈ 0.3

Density ≈ 555 lb/ft^3
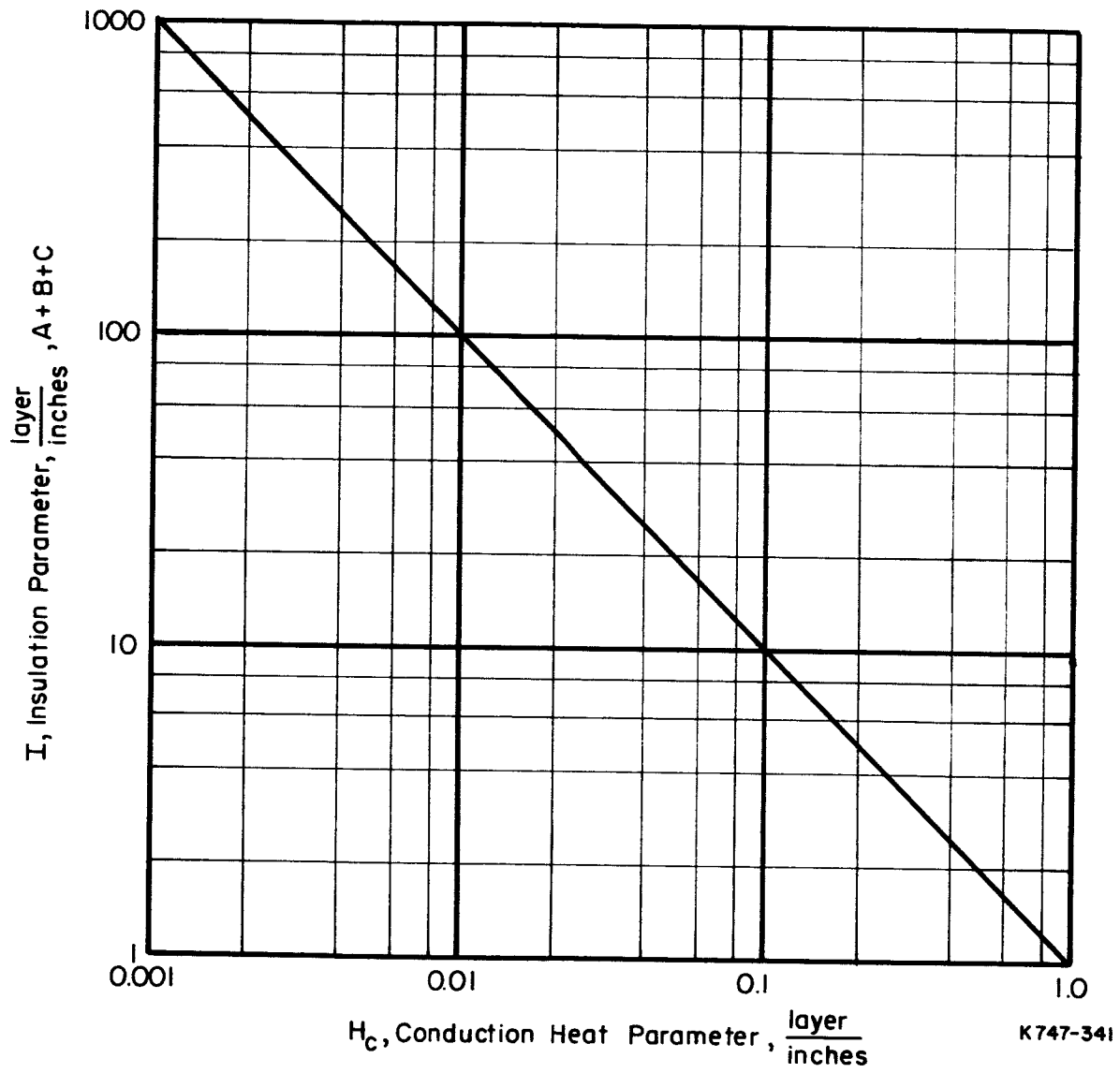
FIGURE 70. CONDUCTION HEAT PARAMETER
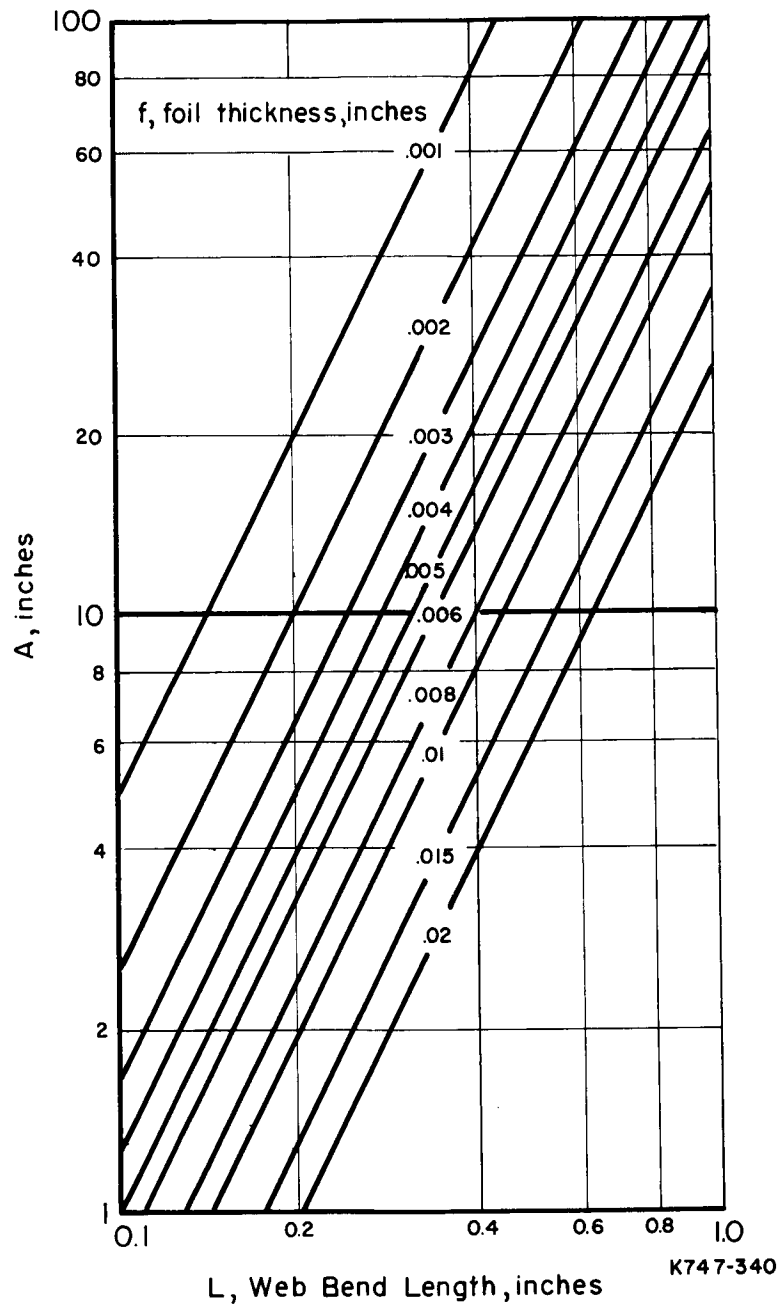
FIGURE 71. GEOMETRIC PARAMETER A
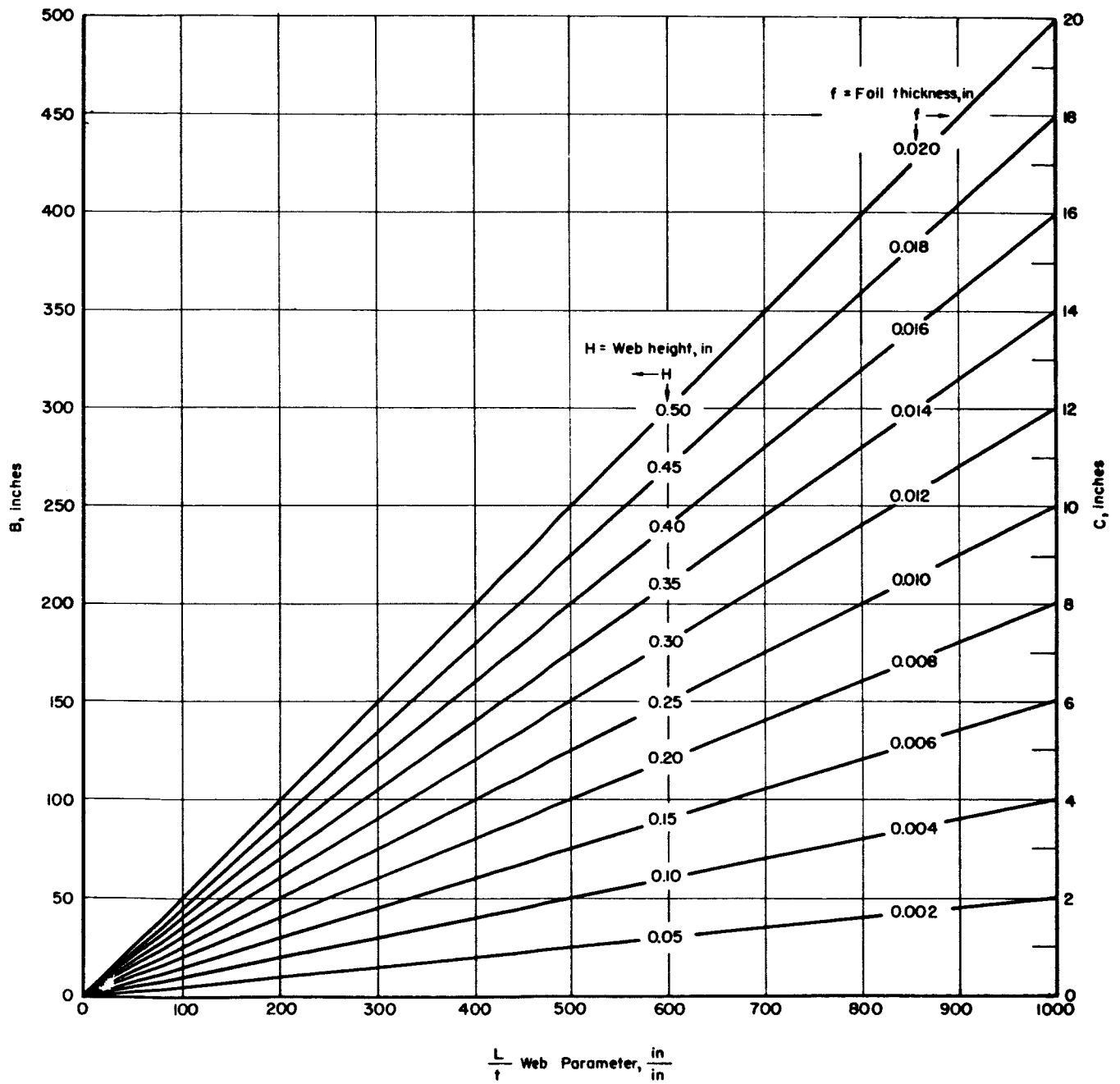
FIGURE 72. GEOMETRIC PARAMETERS B AND C
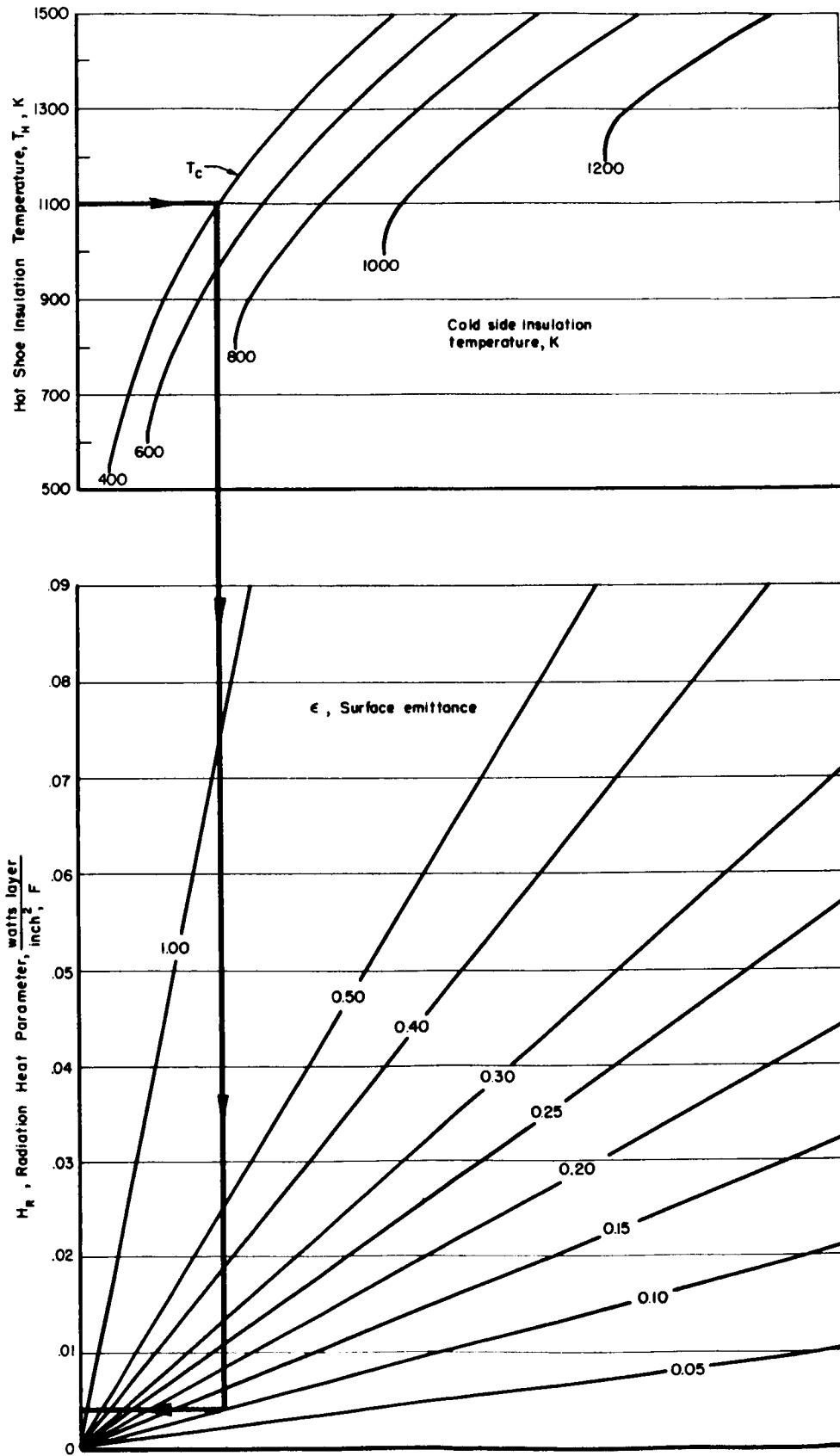
FIGURE 73.   RADIATION HEAT PARAMETER, H_r

BATTELLE   MEMORIAL   INSTITUTE

Thermal conductivity ≈ 0.6 watt/in-K

Yield strength in compression at 1200 K (twice that in shear)
$\approx 16,000$ psi.

TABLE 11. SUMMARY OF INSULATION PERFORMANCE

Insulation Structure*	Type	Web Thickness and Foil Thickness, mils	Effective Thermal Conductivity, Watts/in. K x 10⁴		Yield Strength at 1200 F		Gross Density, lb/ft³
			500-800 K	500-1200 K	Compression	Shear	
17	1	4	16	23	16	36	46
7	1/2	12	135	147	360	250	135
4	1	8	37	47	45	110	86
11	1/2	8	88	97	210	130	96

*Web height (H) is 0.05 in. in all cases.

Two temperature ranges are considered, corresponding to operating temperatures of high- and low-temperature thermoelectric conversion materials.

Thermal

It is seen from the table (Column 4) that the insulation structures can exhibit effective conductivities lower than that of the Hastelloy C by a factor of more than 350. Thus the structures do serve as thermal insulation. For the operating temperatures specified, the thermal conductivities of most commercial fibrous board and block insulations range from 30 to 50 x 10⁻⁴ watts/in-K. MinK-2000, a product of Johns-Manville, and multilayered insulations such as Linde Super-Insulation, under slight compressive loading, exhibit conductivities in the range of 5 x 10⁻⁴ watts/in-K and 1 x 10⁻⁴ watt/in-K, respectively. Table 11 shows that the insulating properties of the insulation structures can, by design, be made superior to those of conventional fibrous insulations.

Structural

An important feature of the insulation structure is the ability to afford usable strength at elevated operating temperatures. The insulation is capable of supporting substantial loads in both shear and compression. The strengths range from 16 to 360 psi in compression and from 36 to 250 psi in shear for the structures considered. The rupture strengths of commercially available fibrous insulations range from 100 to 200 psi in compression. These strengths usually refer to maximum crumbling loads which if exceeded, result in complete structural and thermal breakdown of the insulation. As discussed in the "Testing Section" above, the yield strengths tabulated for the insulation structures represent only limiting values of elastic behavior and not ultimate loads. Furthermore, very few commercial insulations offer any strength in shear. The multilayered insulations have little or no mechanical strength. For extremely high-temperature applications, metallic foils are commonly used in place of fibrous insulations. In such applications the foils themselves must be supported and can offer no mechanical strength. Thus, the insulation structures studied in this program have a clear advantage in high-temperature structural applications.

Weight

From a weight standpoint, the density of the structural insulation will be greater than that of conventional insulations in most applications. The densities of conventional fibrous insulations range from 20-40 lb/ft^3. The density of multilayered insulations under slight compression falls in the middle of this range. From Table 11 it is seen that the structural insulation density can vary from about one to four times that of conventional insulations. It should be noted, however, that any weight penalty may be more than offset by other advantages present in the metallic insulation. These include cleanliness, inertness, chemical stability, and the fact that the structural deformations associated with the loading are elastic, allowing for preloading the insulation.

In general, the stronger structures are heavier and exhibit poorer thermal performance, therefore for actual applications, the structures should be custom designed and an optimization be made between strength, heat loss, and weight.

Conclusions

Fabrication

The thermal insulation and support structures were fabricated of Hastelloy C by gas-pressure bonding. This fabrication technique allowed the complex geometry to be accurately produced with web and foil thicknesses ranging from 4 to 12 mils. The bonded structures were easily machined to 3-inch diameter discs prior to the removal of the filler tooling, demonstrating that it is entirely feasible to generate complex shapes of the insulation.

Testing

The test program included structural testing and thermal testing of the insulation structures. In both shear and compression, the tests revealed an almost linear increase of load with deformation up to a definite yield point. When stressed below the yield load in compression, the structures recover elastically with no permanent set if the load is removed. The deformation accumulated when the structures first start to yield is approximately 10 percent of the total insulation thickness. The lateral deformation accumulated when the structures first start to yield in shear is of the order of a web height.

Thermal testing was performed by measuring the equilibrium heat flow through the insulation while subjecting the structures to constant hot- and cold-side temperatures. The results demonstrate that the insulation concept is valid and that the effective thermal conductivity of the insulation is less than that of the Hastelloy C by more than two orders of magnitude and for selected structures, is superior to most commercially available fibrous insulations.

Correlation of Analysis and Test Results

From the results of the structural testing, empirical equations were derived to describe the insulation strength. These relations include the effect of varying the web

and foil thickness and the web-bend length. These expressions replace originally proposed relations which did not include foil thickness. It was found that the insulation yield strength is a direct function of the material strength. A parametric display of the equations, giving the ratio of the insulation yield strengths to the strengths of the material of construction has been developed.

The thermal tests showed that the measured heat flow was greater than that predicted analytically. By accounting for the effects of thermal conductivity variations in Hastelloy C and surface contamination acquired during testing, the analytical predictions for heat flow were brought into excellent agreement with the measured heat flow values. The equation describing the heat losses through the insulation for given operating conditions and geometric parameters was displayed parametrically.

The resulting equations which describe the structural insulation weight, strength, and heat loss are given in terms of the operating conditions, the insulation geometry, and the properties of the material of construction. The expressions are general and allow for the substitution of properties for any material desired. In the case of insulation weight and strength, the materials properties of density and strength are extracted as multiplying factors. For the thermal performance, the material thermal conductivity and surface emittance are multiplying factors for the conductive and radiative heat flows, respectively.

Summary

In thermoelectric energy conversion devices, the requirements for heat source support and thermal insulation are diametrically opposed. Generally, strong heat source support mechanisms increase heat losses, while super-insulations are subject to mechanical failure. The need, then, is for a structural insulation that has high-temperature capability and stable thermal properties, that is low in thermal conductivity, and that has the compressive and shear strengths to support loads created by generator design and mission requirements.

The salient factors which contrast the insulation concept studied under this program with available insulations are the following: (1) its operating temperature is limited only by the available selection of metals of construction; (2) it is flexible in design and can be optimized with respect to weight, strength, and thermal performance; and (3) intrinsically, it is clean and reliable because of its all-metallic construction.

The thermal insulation and support structure development effort in this program is summarized by the following statements.

(1) Insulation structures were fabricated in a range of sizes.

(2) The insulation was tested mechanically and thermally.

(3) Equations describing the thermal and mechanical performance were established and correlated with previous analytical predictions.

(4) The results show that any reasonable degree of thermal resistance and strength can be designed into the structure by choice of materials and dimensional parameters.

(5) The structural and thermal performance of structures designed for maximum strength and structures designed for maximum thermal resistance is superior to most commercially available fibrous insulations.

Areas for Further Development and Improvement of Insulation Performance

For this experimental investigation, Hastelloy C was chosen as a representative high-temperature nickel-base alloy. It enabled the insulation structures to be fabricated and tested. For actual application perhaps a more suitable choice of material could be made, for the alloy shows a sharp increase in thermal conductivity above 850 K and exhibits an unexpectedly low tensile strength at temperature.

One of the areas for further development is the study and selection of higher strength materials for construction. Using a higher strength material will result in lighter structures accompanied by improved thermal performance.

Further improvement of the fabrication process as it affects surface finish and emittance is also desirable. For high-temperature applications, the radiant heat-transfer component will contribute more than half the thermal losses of the insulation and therefore lowering surface emittance directly improves insulation performance.

The benefits from improvements in insulation performance as a function of material strength and surface finish may be illustrated quantitatively by considering the following example. If the Hastelloy is replaced by a material with the same density and thermal conductivity but twice the strength and half the surface emittance, a performance comparison may be made using the relationships developed in this program. The structures of Table 11 have been resized, holding constant their respective web-bend lengths, web heights, and compressive strengths. Table 12 illustrates the improvement in insulation performance. It is seen that the strongest structure is now approximately six-tenths its former gross density and all other structures exhibit excellent insulating characteristics. It is interesting to note that Structures C and D offer the same thermal insulating capability while each offers a different strength advantage. This observation illustrates the desirability of optimizing the geometric parameters and materials selection. Design development of insulation structures should be extended to include the study of shaped insulation sections, incorporation of attachment brackets, and investigation of structures composed of more than one material. Further advantage may be obtained by employing more than one material of construction where applications over wide temperature ranges are encountered.

TABLE 12. IMPROVEMENT OF INSULATION PERFORMANCE

New Structure	Web Thickness and Foil Thickness	Reference Structure in Table 11	Effective Thermal Conductivity, Watts/in-K x 10^4		Yield Strength at 1200 K		Gross Density, lb/ft^3
			500-800 K	500-1200 K	Compression	Shear	
A	3	17	11	15	16	56	35
B	7	7	75	84	360	200	86
C	5.5	4	19	24	45	130	62
D	3	11	20	24	210	88	39

APPENDIX A

SPACE GENERATOR COMPUTER PROGRAM
OPERATION MANUAL

APPENDIX A

SPACE GENERATOR COMPUTER PROGRAM
OPERATION MANUAL

Introduction

The computer program is operated by providing inputs for the terms listed in the Input Data Form in Part II of this Appendix. The input terms are defined in the Glossary of Computer Program Terms given in Part I. Certain inputs are referenced in Part II to provide additional information and to aid in the data compilation. The input data form combined with the glossary of computer program terms and the referenced input data are all that is required for the data compilation. The terms of the compilation, after being identified in sequence on input cards, handle intrinsically the placement of input data, the selection of the desired computational options, and the method for data print out. For example, the following print-out options can be selected by assigning values to the input terms as follows:

(1) Print out all calculated data for each generator case considered. This is accomplished by setting $ZEP = 1$, $ZI = 1$, $ZBP = 1$, $ZPL\phi T = 0$.

(2) Print out only the data associated with the minimum weight generator. This is accomplished by setting $ZEP = 0$, $ZI = -1$, $ZBP = 0$, $ZPL\phi T = 0$.

(3) Plot data directly onto an X-Y plotter by means of array storage of the pertinent data. This is accomplished by setting $ZPL\phi T = 1$.

A list of recommended values for epsilon and delta functions, which have been estimated on the basis of trial cases of 50, 100, 150, and 250-watt(e) generators is given in Part III of this Appendix. The Glossary of Diagnostics, Part IV, contains corrective measures that are printed out literally in the event of an incorrect tolerance or iterative step function.

I - Read Input
O - Print Output
U - Uncommon Read Input
R - Computer Reserved Words

Part I. Glossary of Computer Program Terms

The glossary is a listing of the input and output computer language containing both the definition and the physical units of the terms. The uncommon inputs refer to the tolerances, iterative step functions, and iteration index number limits and are given in Part III of this Appendix. These inputs may remain unchanged in most cases. The computer reserved words are definitions of terms used in the Fortran portion of the program but not printed out because they are only a portion of a complete analytical expression.

O	1	AEZ	Area available on ends for support, cm^2
O	2	AERQDZ	Area required for end bearing area, cm^2
O	3	ARRQDZ	Area required for radial bearing area, cm^2
I	4	AESF	Absolute end support function:

      (1) AESF = 1 Allow some of the weight to be distributed onto the radial portion

      (2) AESF $\approx$ 0 Do not consider any support by the radial portion

O	5	AMDL	Area of module perpendicular to heat flow, cm^2
O	6	ARZ	Area available radially for support, cm^2
I	7	ARSF	Absolute radial support function:

      ARSF = 1 Allow some of the weight to be distributed onto the ends

      ARSF = 0 Do not allow some of the weight to be distributed onto the ends

O	8	BX	Overall generator length (also radiator length, cm
R	9	BF	Computation factor for instructing computer whether this is initial B value or not
I	10	BFIN	Final overall generator length, cm
I	11	BINCC	Large increment of generator length, cm
I	12	BINCS	Small increment of generator length, cm

I	13	BINCN	Normal increment of generator length, cm
I	14	BINT	Initial overall generator length, cm
I	15	CLEPS	Epsilon function for cladding cubic equation
I,O	16	CLINO	Number of cladding iterations
I	17	CLINOM	Maximum number of allowed cladding iterations
I	18	CLMTL	Fuel-form cladding material
I	19	CNNO	Number of modules
R	20	COEF	Coefficients A, B, and C for cladding cubic equation solution
O	21	CPLNO	Total number of couples in generator
O	22	CPLPCN	Number of couples per module
O	23	DFF	Diameter of fuel form, cm
O	24	DFP	Diameter of fuel pin, cm
O	25	DGS	Diameter of generator shell, cm
O	26	DHS	Diameter of heat source, cm
O	27	DNEL	Breadth of n-type element (projected breadth if round), cm
O	28	DPEL	Breadth of p-type element (projected breadth if round), cm
O	29	DPHMDL	Length of module in direction of heat flow, cm
O	30	DRFBAE	Deflection of heat source as a result of bearing area available on ends, cm
O	31	DRFBAR	Deflection of heat source as a result of bearing area available radially, cm
O	32	DRSI	Inside diameter of generator radiator shell, cm
I	33	ECE	Elastic modulus (compression) of end heat-source support, lb/cm^2
I	34	ECR	Elastic modulus (compression) of radial heat-source support, lb/cm^2
O	35	EECALC	Engineering efficiency calculated by heat balance (decimal)

O	36	EECF	Engineering efficiency correction factor

0 - Assumed engineering efficiency
+1 - Assumed engineering efficiency too large
-1 - Assumed engineering efficiency too small

I	37	EEASMD	Assumed engineering effi~ ~ncy (decimal form)
U	38	EEDEL	Delta function for engineering efficiency (increment) (decimal form)
U	39	EEDELS	Small delta function for engineering efficiency (increment) (decimal form)
U	40	EEEPS	Epsilon function for engineering efficiency (tolerance) (decimal form)
O	41	EEINϕ	Engineering efficiency iteration number
I	42	EEINϕM	Maximum allowed number of engineering efficiency iterations
O	43	EHSD	Effective heat-source diameter, cm
O	44	EIINϕ	End-insulation iteration number
I	45	EIINϕM	Maximum allowed number of end-insulation iterations
U	46	EIT	Delta function for insulation on ends (increment), cm
R	47	EITF	End-insulation-thickness factor:

0 - should iterate by increasing QXE
1 - should iterate by decreasing QXE

I	48	EL	Element length assumed, cm
O	49	ELX	Element length, cm
U	50	ELDEL	Delta function for element length (increment), cm
R	51	ELF	Element length iteration determination factor
O	52	ELINϕ	Number of iterations performed on EL
I	53	ELINϕM	Maximum number of iterations allowed upon EL
I	54	ELMAX	Maximum element length to be considered by generator, cm
R	55	ELMAXF	Element-length maximum function:

0 - maximum has been reached
1 - maximum has not been reached

I	56	ELMIN	Minimum element length to be considered by generator, cm
R	57	ELMINF	Element-length minimum function:

0 - minimum has been reached
1 - minimum has not been reached

O	58	ELNO	Number of thermoelectric elements
I	59	ENϕEW	Even number of elements in module width option:

(1) ENOEW = 0 can be even or odd
(2) ENOEW = must be even number

I	60	ESE	Elastic modulus (shear) of end heat-source support, lb/cm^2
I	61	ESR	Elastic modulus (shear) of radial heat-source support, lb/cm^2
U,O	62	FFDEL	Delta function for fuel-form length (increment), cm
U,O	63	FFEPS	Epsilon function for fuel-form length (tolerance), cm
O	64	FFLINϕ	Fuel-form-length iteration number
I	65	FFLINM	Maximum number of iterations allowed
I	66	FFPD	Fuel-form power density, watts/cc
I	67	FHDC	Fin-thickness parameter
I	68	FNO	Number of fins
I	69	FPA	Fuel-pin array

(1) FPA = 0   Locus of all fuel pin centers is a circle
(2) FPA = 1   Close packing of fuel pins

O	70	FPCS	Fuel-pin center separation, cm
I	71	FPD	Fuel-pin density in matrix (decimal)
I	72	FPEF	Fuel-pin-effectiveness factor (decimal)
I	73	FPFTS	Fuel pin-fuel tube separation, cm
I	74	FPS	Fuel-pin separation (minimum), cm
I	75	FPNO	Number of fuel pins

I	75.1	FWP	Fin-weight parameter
I	76	GA	g -loading axially (dimensionless)
I	77	GPL	Generator power level, watts
I	78	GR	g -loading radially (dimensionless)
O	79	HDBE	Heat dumped by ends
I	80	HDBEPC	Percent of total heat-dump capability of generator ends (decimal form)
O	81	HLACN	Heat-loss area for module periphery, cm^2
O	82	HLACSE	Heat-loss area for end heat-source support, cm^2
O	83	HLACSR	Heat-loss area for radial heat-source support, cm^2
O	84	HLAEI	Heat-loss area for module electrical and thermal insulation, cm^2
O	85	HLAMC	Heat-loss area for end insulation, cm^2
O	86	HLARI	Heat-loss area for generator radial insulation, cm^2
O	87	HLCN	Heat loss through module periphery cross section, watts
O	87.1	HLCNR	Heat loss through module periphery by radiative heat transfer, watts
O	88	HLCNW	Heat loss through module-wedge insulation, watts
O	89	HLCSE	Heat loss through heat-source-support cross section (ends), watts
O	90	HLCSR	Heat loss through heat-source-support cross section (radially), watts
O	91	HLEI	Heat loss through generator end insulation, watts
O	92	HLETI	Heat loss through module electrical and thermal insulation, watts
O	93	HLRI	Heat loss through generator radial insulation, watts
O	94	HLTOT	Heat losses through all media except elements, watts
O	95	HRF	Height of radiator fin, cm

R	96	HSSASF	Heat-source-support-area shortage factor:

(1) HSSASF = -1 Not enough bearing area on ends
(2) HSSASF = 0 No shortage
(3) HSSASF = 1 Not enough bearing area radially

R	97	HSSC	Heat-source-shortage conflict:

0 - no conflict
1 - area required by T/E's in conflict with area required by heat-source support

I	98	HSSEDN	Heat-source-support-end deflection neglection:

(1) HSSEDN = 0 Permits end deflection to control B
(2) HSSEDN = 1 Allows B to be independent of end deflection

I	98.1	HSSFSE	Heat-source-support foil separation on end support, cm
I	98.2	HSSFSR	Heat-source-support foil separation on radial support, cm
I	99	HSSPD	"Effective" surface-power-density available for module, watts/cm^2
I	100	HTM	Heat-transfer mode:

HTM = 1 Conductive
HTM = 2 Radiative

I	101	HWTC	Hardware thickness (that space between heat source and inside of shell that is occupied by T/E connecting hardware in conductive mode), cm
I	102	HWTR	Hardware thickness and radiation gap (space occupied by T/E connecting hardware for radiation mode), cm
O	103	NEW	Number of elements in module width
O	104	QIN	Heat that must be supplied by fuel form, watts
R	105	QINFP	Heat that must be supplied by fuel pin, watts
O	106	QOUT	Heat that must be dumped by radiator, watts
O	107	QXE	Separation between heat source and shell (ends), cm
O	108	QXR	Separation between heat source and shell (radially), cm

I	109	RDELL	Radiator delta function (large), cm
I	110	RDELS	Radiator delta function (small), cm
I	111	REPS	Epsilon function for radiator analysis, cm
I	112	RFEMIS	Radiator-fin emissivity
I	113	RFISR	Radiator-fin incident radiation from space
I	114	RFSF	Radiator-fin shape factor
I	115	RG	Radiation gap, cm
I	115.1	RHOA	Density of ablator, lb/cc
I	116	RHOCL	Density of the fuel-form cladding, lb/cc
I	117	RHOCN	Density of periphery material, lb/cc
I	118	RHOCNE	Density of Phase I n-type segment (cold end), lb/cc
I	119	RHOCPE	Density of the Phase I p-type segment, lb/cc
I	120	RHOFB	Density of fuel block, lb/cc
I	121	RHOFF	Density of the fuel form, lb/cc
I	122	RHOFFV	Impact velocity of heat source, cm/sec
I	123	RHOFP	Density of the fuel pin, lb/cc
I	124	RHOFT	Density of the fuel tube, lb/cc
I	125	RHOH	Density of T/E hardware (end plates, shoes, insulation, etc.), lb/cc
I	126	RHOHNE	Density of the Phase III n-type segment, lb/cc
I	127	RHOHPE	Density of the Phase III p-type segment, lb/cc
I	128	RHOHSE	Density of the end heat source support, lb/cc
I	129	RHOHSR	Density of the radial heat-source support, lb/cc
I	130	RHOINE	Density of end insulation, lb/cc
I	131	RHOINR	Density of radial insulation, lb/cc
I	132	RHOIC	Density of inner cladding, lb/cc
I	133	RHOMNE	Density of Phase II n-type segment, lb/cc
I	134	RHOMPE	Density of Phase II p-type segment, lb/cc

I	135	RHOOSC	Density of outer cladding, lb/cc
I	136	RHOR	Density of radiator, lb/cc
I	137	RHOS	Density of shell, lb/cc
I	137.1	RHOSHO	Density of shoe material, lb/cc
I	138	RHOTEI	Density of thermal and electrical insulation between elements, lb/cc
O	139	RINØL	Number of large iterations for radiator
I	140	RINØM	Maximum total iteration number for radiator
I	141	RINØLM	Maximum large iteration number for radiator
O	142	RINØS	Number of small iterations for radiator
I	143	RINØSM	Maximum small iteration number
O	144	RLTDFF	Ratio of length to diameter of fuel form
I	145	RMTL	Radiator material
O	146	RSPD	Surface-power-density required by module, watts/cm^2
I	148	SEGNO	Number of thermoelectric element segments (1,2,3)

        (1) SEGNO = 1 Single phase
        (2) SEGNO = 2 Two-phase, segmented
        (3) SEGNO = 3 Three-phase, segmented

I	148.1	SHOETK	Thickness of element shoes, cm
I	149	SIGCL	Toughness parameter of cladding
I	150	SMTL	Shell material
O	151	SNFF	Number of fuel-form segments
I	154	TC	Temperature of thermoelement cold junction, K
I	155	TCI	Temperature at cold end of insulation, K
I	156	TEI	Thermoelectric current, amp
I	157	TEMTL	Thermoelectric material
I	158	TH	Temperature at hot end of the thermoelectrics, K
I	159	THI	Temperature at hot end of the insulation, K

I	160	THSS	Temperature at heat-source surface (that surface which is adjacent to module), K
I	160.1	TKAE	Thickness of ablator on end, cm
I	160.2	TKAR	Thickness of ablator on radial portion, cm
I	161	TKASMD	Thickness of fuel-form cladding assumed, cm
I	162	TKCAN	Thickness of module periphery material, cm
O	163	TKCL	Thickness of fuel-form cladding, cm
I	164	TKCLIS	Thickness of inner cladding (liner for cladding), cm
I	165	TKCLOS	Thickness of outer shell cladding (overcladding), cm
I	167	TKFT	Thickness of fuel tube, cm
I	167.1	TKPRG	Thickness of module peripheral gap for radiation-loss analysis, cm
O	168	TKRS	Thickness of radiator shell, cm
O	169	TKRFB	Thickness of radiator fin at base, cm
I	170	TKTEII	Thickness of thermal and electrical insulation between elements, cm
R	171	TL	Lower limit of cladding thickness
U	172	TINDEL	Delta function for end insulation (increment), cm
I	173	TMDE	Maximum tolerable deflection of end heat-source support, cm
I	174	TMDR	Maximum tolerable deflection of radial heat-source support, cm
I	175	TR	Temperature of radiator, K
I	176	TU	Upper limit of cladding thickness for use in cubic equation, cm
O	177	VFF	Volume of fuel form, cm^3
O	178	VFP	Volume of fuel pin, cm^3
I	179	VTPCPL	Voltage per couple output of the thermoelectrics, volts
O	180	WCL	Weight of fuel-form cladding, lb

O	181	WCLI	Weight of inner cladding or liner, lb
O	182	WCLS	Weight of outer cladding, lb
R	183	WCKBC	Check-weight to test large iterations on generator length
R	184	WCKBS	Check-weight to test small iterations on generator length
R	185	WCKE	Check-weight to test iterations on element length
R	186	WCKI	Check-weight to test iterations on end-insulation thickness
O	187	WCN	Weight of module periphery, lb
O	188	WDMDL	Module width, cm
O	189	WEI	Weight of generator end insulation, lb
U	190	WEPSB	Epsilon function for weight in generator-length trade-off (tolerance), lb
U	191	WEPSEI	Epsilon function for weight in end-insulation tradeoff (tolerance), lb
U	192	WEPSIE	Epsilon function for weight in thermoelectric-length tradeoff (tolerance), lb
O	193	WFB	Weight of fuel block, lb
O	194	WFF	Weight of fuel form, lb
O	195	WFP	Weight of fuel pin, lb
O	196	WFT	Weight of fuel tube, lb
O	197	WHS	Weight of heat source, lb
O	198	WHSE	Weight of end heat-source support, lb
O	199	WHSR	Weight of radial heat-source support, lb
O	200	WMDL	Weight of module (thermoelements and can), lb
O	201	WNEL	Width of n-type element (projected width if round), cm
O	202	WPEL	Width of p-type element (projected width if round), cm
O	202.1	WRA	Weight of radiative ablator, lb
O	203	WRF	Weight of radiator fins, lb

O	204	WRI	Weight of generator radial insulation, lb
O	205	WRS	Weight of generator shell, lb
O	206	WSFF	Weight of sub-fuel form, lb
O	207	WSFP	Weight of sub-fuel pin, lb
O	208	WTE	Weight of thermoelectric materials, lb
O	209	WTEHW	Weight of thermoelectric hardware (shoes, module contact mechanism, heat collector, etc.), lb
O	210	WTOT	Total weight of the generator, lb
R	211	WTOTR	Total weight of generator reserved for comparison, lb
O	212	XCL	Number of couples in length of module
O	213	XEW	Number of elements in width of module
I	214	XKHSE	Thermal conductivity of end heat-source support, watts/(cm)(C)
I	215	XKHSR	Thermal conductivity of radial heat-source support, watts/(cm)(C)
I	215.1	XIFSE	End-insulation-foil separation, cm
I	215.2	XIFSR	Radial-insulation-foil separation, cm
I	216	XKINE	Thermal conductivity of end insulation, watts/(cm)(C)
I	217	XKINR	Thermal conductivity of radial insulation, watts/(cm)(C)
I	218	XKMPE	Effective thermal conductivity of module periphery, watts/(cm)(C)
I	219	XKR	Thermal conductivity of radiator, watts/(cm)(C)
I	220	XKS	Thermal conductivity of shell, watts/(cm)(C)
I	221	XKTAEI	Effective thermal conductivity of thermal and electrical insulation, watts/(cm)(C)
I	222	XLACN	Length-to-area ratio of Phase I n-element
I	223	XLACP	Length-to-area ratio of Phase I p-element
I	224	XLAHN	Length-to-area ratio of Phase III n-element
I	225	XLAHP	Length-to-area ratio of Phase III p-element

I	226	XLAMDA	Fin-length parameter
I	227	XLAMN	Length-to-area ratio of Phase II n-element
I	228	XLAMP	Length-to-area ratio of Phase II p-element
I	229	XLARFF	Limiting-aspect ratio of fuel form
I	230	XLARFP	Limiting-aspect ratio of fuel pin
I	231	XLARGE	Limiting-aspect ratio of generator envelope
I	232	XLARGS	Limiting-aspect ratio of generator shell
O	233	XLCNE	Length of Stage I n-type segment, cm
O	234	XLCPE	Length of Stage I p-type segment, cm
O	235	XLFF	Length of fuel form, cm
O	236	XLSFF	Length of segmented fuel form, cm
O	237	XLHNE	Length of Stage III n-type segment, cm
O	238	XLHPE	Length of Stage III p-type segment, cm
O	239	XLHS	Length of heat source, cm
O	240	XLSHS	Length of segmented heat source, cm
O	241	XLMDL	Module dimension parallel to generator axis, cm
O	242	XLMNE	Length of Stage II n-type segment, cm
O	243	XLMPE	Length of Stage II p-type segment, cm
I	246	XMLINM	Maximum number of iterations for adjustment of module size
I	247	XMRFHS	Heat-source length minus module width (limit), cm
I	248	XMRFWH	Heat-source width minus module width (limit), cm
I	249	XNTEEL	End of life thermoelectric efficiency (decimal)

| I | 250 | ZA | Choice of array computational sequence |

  (1) ZA = 1   Limited by heat-source diameter
                (within preset tolerance)
  (2) ZA = 2   Limited by heat-source length
                (within preset tolerances)
  (3) ZA = 3   Investigates Cases 1 and 2

       (Geometry of module based on beometry of
        heat source.)

| I | 251 | ZB | Choice of generator-length computational sequence |

  (1) ZB = 0   Iterate using normal increments

  (2) ZB = 1   Iterate using large increments and
                then small increments

| I | 252 | ZE | Choice of element-length computation sequence: |

  (1) ZE = 0   Element length is fixed

  (2) ZE = -1   Element length is varied with EL as
                maximum in order to trade off T/E
                weight vs other generator compo-
                nents (viz. , heat source, insula-
                tion, shell, etc.)

| I | 253 | ZELP | Print-out option for element insulation: |

  ZELP = -1   Print out after element length is opti-
               mized for a given generator length
               and array
  ZELP = 0   Print out only after generator length
               and array have been optimized

| I | 254 | ZEP | Print-out option for element-length iteration |

  (1) ZEP = 0   Do not print out until minimum is
                 reached
  (2) ZEP = 1   Print out after each iteration

| I | 255 | ZF | Choice of fuel form: |

  (1) ZF = 0   Right-cylinder geometry for single
                fuel form
  (2) ZF = 1   Right-cylinder geometry for sub-fuel
                form or fuel pins and overall right-
                cylinder geometry for fuel block

I	256	ZHSS	Heat-source-support computation option:

    (1) ZHSS = -1   Maximum support by ends

    (2) ZHSS = 0   Support by both end and radial portions

    (3) ZHSS = 1   Maximum support by radial portion

I	257	ZI	End-insulation computation option:

    (1) ZI = 0   Insulation thickness is fixed, not optimized on

    (2) ZI = -1   Trade off against other generator components but do not print out until minimum weight combination is reached

    (3) ZI = +1   Trade off and print out each value

I	258	ZIAS	Insulation and heat-source-support option:

    (1) ZIAS = 0   Solid-type insulation and support

    (2) ZIAS = 1   Foil- and Honeycomb-type insulation and support

I	259	ZP	Generator-length print option

    (1) ZP = 0   Print out after each iteration

    (2) ZP = -1   Do not print out until minimum is reached

    (3) ZP = +1   Do not print out until array is optimized

I	260	ZPGD	Generated-data print-out option

    (1) ZPGD = 0   Do not print out all generated data, only B, ZA, W, TOT, EL, QXE

    (2) ZPGD = 1   Do print out all generated data

I	262	ZPRI	Print out of read in data option

    (1) ZPRI = 0   Do not print out read in data

    (2) ZPRI = 1   Do print out read in data

I	263	ZSETNO	Identifying number for set of parameters considered

I	264	ZZSI	Insulation - heat source support material option

    (1) ZZSI = 0   Treat insulation and heat-source support as independent components

    (2) ZZSI = 1   Assume insulation and heat-source are same and calculate deflection of support material on the basis of total bearing area available.

Part II. Input Data Form

This form is a list of program inputs. A particular input value is designated by the input card number and the input field. These input terms are defined in the Glossary of Computer Program Terms. Several of the inputs are discussed in Input Data Reference to aid in the data compilation. The column provided under "Value" should be used for data entries.

RUN: _____

ZSETNO: _____

Number	Term	Input Card No.	Input Field	Reference	Units	Value
1	AESF	1	1-7		None	
2	ARSF	1	8-14		None	
3	BFIN	1	15-21		Cm	
4	BINCC	1	22-28		Cm	
5	BINCS	1	29-35		Cm	
6	BINCN	1	36-42		Cm	
7	BINT	1	43-49		Cm	
8	CLEPS	1	50-56		Cm	
9	CLINO	1	57-63		None	
10	CLINOM	1	64-70		None	
11	CLMTL	2	1-7	A	None	
12	CNNO	2	8-14	B	None	
13	ECE	2	15-21	D	Lb/cm^2	
14	ECR	2	22-28	D	Lb/cm^2	
15	EEASMD	2	29-35	E	None	
16	EEDEL	2	36-42		None	
17	EEDELS	2	43-49		None	
18	EEEPS	2	50-56		None	
19	EEINOM	2	57-63		None	
20	EINOM	2	64-70		None	
21	EL	3	1-7		Cm	
22	ELDEL	3	8-14		Cm	
23	ELINOM	3	15-21		None	
24	ELMAX	3	22-28	F	Cm	
25	ELMIN	3	29-35	F	Cm	
26	ENOEW	3	36-42	G	None	
27	ESE	3	43-49	D	Lb/cm^2	
28	ESR	3	50-56	D	Lb/cm^2	
29	FFDEL	3	57-63	C	Cm	
30	FFEPS	3	64-70	C	Cm	
31	FFLINM	4	1-7		None	
32	FFPD	4	8-14	H	Watts/cc	
33	FHDC	4	15-21		None	
34	FNO	4	22-28		None	

Number	Term	Input Card No.	Input Field	Reference	Units	Value
35	FPA	4	29-35		None	
36	FPEF	4	36-42	J	None	
37	FPFTS	4	43-49	K	Cm	
38	FPNO	4	50-56		None	
39	FPS	4	57-63	K	Cm	
40	GA	4	64-70		None	
41	GPL	5	1-7		Watts	
42	GR	5	8-14		None	
43	HDBEPC	5	15-21	L	None	
44	HSSEDN	5	22-28	M	None	
45	HTM	5	29-35		None	
46	HWTC	5	36-42	N	Cm	
47	HWTR	5	43-49	N	Cm	
48	RDELL	5	50-56		Cm	
49	RDELS	5	57-63		Cm	
50	REPS	5	64-70		Cm	
51	RFISR	6	1-7	C	None	
52	RFSF	6	8-14	C	None	
53	RG	6	15-21	N	Cm	
54	RHOCL	6	22-28		Lb/cc	
55	RHOCN	6	29-35		Lb/cc	
56	RHOCNE	6	36-42		Lb/cc	
57	RHOCPE	6	43-49		Lb/cc	
58	RHOFB	6	50-56		Lb/cc	
59	RHOFF	6	57-63	O	Lb/cc	
60	RHOFFV	6	64-70	Q	M/sec	
61	RHOFP	7	1-7		Lb/cc	
62	RHOFT	7	8-14		Lb/cc	
63	RHOH	7	15-21		Lb/cc	
64	RHOHNE	7	22-28		Lb/cc	
65	RHOHPE	7	29-35		Lb/cc	
66	RHOHSE	7	36-42		Lb/cc	
67	RHOHSR	7	43-49		Lb/cc	
68	RHOINE	7	50-56		Lb/cc	
69	RHOINR	7	57-63		Lb/cc	
70	RHOIC	7	64-70		Lb/cc	
71	RHOMNE	8	1-7		Lb/cc	
72	RHOMPE	8	8-14		Lb/cc	
73	RHOOSC	8	15-21		Lb/cc	
74	RHOR	8	22-28		Lb/cc	
75	RHOS	8	29-35		Lb/cc	
76	RHOTEI	8	36-42		Lb/cc	
77	RINOM	8	43-49		None	
78	RINOLM	8	50-56		None	
79	RINOSM	8	57-63		None	
80	RMTL	8	64-70		None	
81	SPDEPS	9	1-7		Watts/cm^2	
82	TC	9	8-14	S	°K	

Number	Term	Input Card No.	Input Field	Reference	Units	Value
83	TCI	9	15-21	S	°K	
84	TEI	9	22-28	R	Amp	
85	TEMTL	9	29-35	A	None	
86	TH	9	36-42	S	°K	
87	THI	9	43-49	S	°K	
88	THSS	9	50-56	S	°K	
89	TKASMD	9	57-63	T	Cm	
90	TKCAN	9	64-70		Cm	
91	TKCLIS	10	1-7		Cm	
92	TKCLOS	10	8-14		Cm	
93	TKPRG	10	15-21		Cm	
94	TKFT	10	22-28		Cm	
95	TKTEII	10	29-35		Cm	
96	TINDEL	10	36-42		Cm	
97	TMDE	10	43-49	P	Cm	
98	TMDR	10	50-56	P	Cm	
99	TR	10	57-63	S	°K	
100	TU	10	64-70	T	Cm	
101	SEGNO	11	1-7		None	
102	SIGCL	11	8-14	Q	Lb/cm^2	
103	SMTL	11	15-21	A	None	
104	VTPCPL	11	22-28	R	Volts	
105	WEPSB	11	29-35	U	Pounds	
106	WEPSEI	11	36-42	U	Pounds	
107	WEPSIE	11	43-49	U	Pounds	
108	XKHSE	11	50-56		Watts/(cm)(K)	
109	XKHSR	11	57-63		Watts/(cm)(K)	
110	XKINE	11	64-70		Watts/(cm)(K)	
111	XKINR	12	1-7		Watts/(cm)(K)	
112	XKMPE	12	8-14		Watts/(cm)(K)	
113	XKR	12	15-21		Watts/(cm)(K)	
114	XKS	12	22-28		Watts/(cm)(K)	
115	XKTAEI	12	29-35		Watts/(cm)(K)	
116	XLACN	12	36-42	R	Cm^{-1}	
117	XLACP	12	43-49		Cm^{-1}	
118	XLAHN	12	50-56		Cm^{-1}	
119	XLAHP	12	57-63		Cm^{-1}	
120	XLAMDA	12	64-70	C	None	
121	XLAMN	13	1-7		Cm^{-1}	
122	XLAMP	13	8-14		Cm^{-1}	
123	XLARFF	13	15-21		None	
124	XLARFP	13	22-28		None	
125	XLARGE	13	29-35		None	
126	XLARGS	13	36-42		None	
127	XMLINM	13	43-49		None	
128	XMRFHS	13	50-56		Cm	
129	XMRFWH	13	57-63		Cm	
130	XNTEEL	13	64-70		None	

Number	Term	Input Card No.	Input Field	Reference	Units	Value
131	ZA	14	1-7		None	
132	ZB	14	8-14		None	
133	ZE	14	15-21		None	
134	ZEP	14	22-28		None	
135	ZF	14	29-35		None	
136	ZHSS	14	36-42		None	
137	ZI	14	43-49		None	
138	ZPGD	14	50-56		None	
139	ZPRI	14	57-63		None	
140	ZSETNO	14	64-70		None	
141	TKRS	15	1-7		Cm	
142	RFEMIS	15	8-14	C	None	
143	FPD	15	15-21	J	Units/cm^2	
144	HSSPD	15	22-28	X	None	
145	FWP	15	29-35		None	
146	ZELP	15	36-42		None	
147	SHOETK	15	43-49		Cm	
148	RHOSHO	15	50-56		Lb/cc	
149	ZZSI	15	57-63		None	
150	TKAE	15	64-70		Cm	
151	TKAR	16	1-7		Cm	
152	RHOA	16	8-14		Lb/cc	
153	ZP	16	15-21		None	
154	ZIAS	16	22-28		None	
155	HSSFSE	16	29-35		Cm	
156	HSSFSR	16	36-42		Cm	
157	XIFSE	16	50-56		Cm	
158	XIFSR	16	57-63		Cm	

Input Data Reference

A. Material Designation

All materials used in the generalized code will be identified by their atomic numbers. The designation of compounds as alloys will be made by two atomic numbers separated by a decimal point. However, three-phase materials may be expressed with only a single decimal point in order to satisfy print-out requirements. For example, Ge-Si would appear as 32.14 but Ge-Bi-Te would be given by 32.8352.

B. Selection of Module Number

The selection of the number of modules is a tradeoff between module peripheral losses and desired number of fins. For maximum utilization of radiator fins, the number of modules should match the number and position of the fins. Therefore, this selection will be subject to the selection of the number of fins discussed.

C. Selection of Radiator Parameters

FHDC	-	Ψ
FNO	-	N
RFISR	-	θ
RFSF	-	τ
RHOR	-	ρ
XKR	-	k
XLAMDA	-	ϕ
RFEMIS	-	ϵ

The optimum number of fins can be found from the minimum value "Fin-Weight Parameter Column" given in Tables C-1 through C-10 in Reference (1). After selecting a fin number with an appropriate emissivity, the corresponding fin-height parameter, ϕ, and fin-thickness parameter, Ψ, can be found in these tables. The values of τ and θ may be selected arbitrarily and k and ρ are dependent upon the radiator material. The above parameters are also discussed on pages 25-40 of Reference (1).

D. Modulus of Elasticity for Heat-Source Support

The compressive- and shear-modulus inputs are necessary for the determination of heat-source support required for a maximum allowed deflection. The values will often be supplied with homogeneous materials. However, for more complex support structures, such as honeycomb, special data reports must be consulted. Since

heat-source support is a basic necessity, the support medium may have to be designed for a required modulus.

E. Initial Assumption of Engineering Efficiency

This program is designed to construct mathematically a generator based on as-sumed thermoelectric and engineering efficiencies. Therefore, the operator must se-lect a practical value of engineering efficiency for the program. The program will ana-lyze and iterate on engineering efficiency until a heat balance is achieved. Thus, the proper selection of this parameter will greatly reduce the computer run time.

F. Element-Length Limits

These limits are imposed to avoid impractical element shapes and sizes due to the element-length iterations taking place in the program. The limits may be based on fabricability or insulation capability, since insulation thickness and heat-source-support thickness follows the element length.

G. Thermoelectric-Array Option

The choice of module-width array is affected by the requirements imposed by equipment used in the vicinity of the generator. For example, for magnetometers, extraneous fields produced by current-carrying wires must be arranged so that they are self-cancelling. This is achieved by an array with equal numbers of n and p ele-ments across the width of the module, and this can be introduced into the program by means of the ENOEW number.

H. Fuel-Form Power Density

This power density is usually found in the properties table of a candidate fuel form. However, when fission gas must be accommodated by void space, the fuel-form power density is reduced to an effective power density. This power density is used to determine the volume the fuel form will occupy, including the void volume.

J. Fuel-Pin Effectiveness

This parameter defines the packing density of the fuel pins in the fuel-block matrix. The maximum packing fraction is about 70 percent and will have to be deter-mined prior to the computer run. This number, when divided into the total cross-sectional area of the fuel pins, will give the total cross-sectional area of the fuel-form cross section. The value is used when an undefined array is specified.

K. Separation Between the Fuel Pin-Fuel Tube
     and Between Fuel Pins

This input permits the operator to choose the fuel-block thickness between a fuel pin and the fuel tube which supports the fuel block plus fuel pins. This only applies to

the symmetric fuel-pin array which is selected by the input value for FPA, the fuel-pin-array option.

The separation between fuel pins along a line connecting the fuel-pin centers allows the packing density to be controlled. Note that the fuel block is optional in the case of radiation heat transfer. In this case, the fuel pins would be supported by a frame whose weight would be included under the heading of the fuel block. See Section II for discussion of fuel-pin options.

L. Heat Dissipation by Generator Ends

The particular mission of a generator may allow all, part, or none of the end area of the generator shell to dissipate heat. This may be introduced into the program by specifying the percentage of the total dissipative capability available for heat dump.

M. Heat-Source-Support End-Deflection Neglection

This option permits the code to consider or ignore longer generators when a deficiency of end-support bearing area exists. Longer generators are attended by decreasing end areas, which serves to increase the bearing-area deficiency.

N. See definition in Glossary

O. Fuel-Form Density

The fuel-form density may be expressed as an effective value if void volumes are incorporated into the fuel form. For example, if a fuel requires an additional 100 percent void volume due to fission-gas release, then the effective fuel-form density, RHOFF, would be one-half the actual fuel-form density for the weight calculation.

P. Maximum Tolerable Deflections

The module, heat source, or support may be limited in deflection because of preservation of electrical or thermal contacts of the thermoelectrics, excessive shear forces on thermoelectrics or heat-source support, or increase in heat transfer through heat-source support or insulation due to reduction in heat path.

Q. Toughness Parameter and Impact Velocity

This parameter is used in the cladding analyses subroutine of the program. The selection of this term is discussed on Pages 75 to 80 of Reference (1). Also in this reference appears a discussion of the impact velocity and how the cladding analyses establish a cladding thickness sufficient for intact impact with an unyielding surface.

R. Thermoelectric Current and Voltage

The selection of the operating current establishes the shape factor of the thermoelectric elements. The current may be selected on the basis of power level, voltage level, or shape-factor preference. The voltage per couple and shape factor may be obtained from the thermoelectric-input analysis.

S. Generator Profile Temperatures

The temperatures of the cold junction of the thermoelectrics, cold junction of the insulation, and the radiator surface may all be specified independently to accommodate the temperature differentials present in the heat path for the thermoelectric cold junction to the radiator surface. The same procedure is used at the hot junction.

T. Cladding Upper Limit

This value is used in the cladding-analysis subroutine to determine an upper limit for the calculation procedure. If this value is too small or the cladding tolerance is too large, the code will print a diagnostic of the form: "cladding tolerance too small". In this case, both possibilities would be checked and corrected by the operator.

U. Weight-Tolerance Functions

The choice of the tolerances for the weight tradeoffs of the generator length, element length, and end-insulation thickness are especially important because their value will instruct the computer to either continue iteration to reduce the weight or to terminate iteration since the weight savings is negligible. For example, if the system was approximately 100 pounds total and the operator did not want to consider a weight iteration unless it yielded a 5 percent weight reduction or more, he would read-in a weight epsilon function of 5 pounds. This tolerance then may bypass the element-length or end-insulation-thickness iterations altogether, or may terminate the generator length at some point in the run.

X. Heat-Source-Surface Power Density

The heat-source-surface power density is selected on the basis of maximum-power-density capability. This value is found from two-dimensional heat-flow considerations of the fuel form, fuel block, cladding, and fuel-tube composite. The term is then used in the computer to determine whether the designed thermoelectric module requires a surface power density greater than that practical for a particular heat-source design. A surface-power-density deficiency will result in an escalation of the heat-source surface temperature which will increase parasitic heat losses through the insulation and heat-source support.

Part III. Recommended Inputs

This list contains suggested epsilon and delta functions for use as a starting point in a particular programmed analysis. These particular inputs have been estimated on the basis of trial cases of 50-watt(e) and 250-watt(e) generators.

	Function	Value	Units
1.	CLEPS	0. 10	Cm
2.	CLINOM	100	
3.	EEDEL	0. 05	Decimal form
4.	EEDELS	0. 005	Decimal form
5.	EEEPS	0. 001	Decimal form
6.	EEINOM	50	
7.	EINOM	50	
8.	ELDEL	0. 10	Cm
9.	ELINOM	35	
10.	FFDEL	0. 03	Cm
11.	FFEPS	0. 03	Cm
12.	FFLINM	300	
13.	RDELL	0. 5	Cm
14.	RDELS	0. 01	Cm
15.	REPS	0. 01	Cm
16.	RINOM	50	
17.	RINOLM	50	
18.	RINOSM	50	
19.	TINDEL	0. 2	Cm
20.	XMLINM	50	

Part IV. Glossary of Diagnoses

The list contains the corrective measures in the event of either an incorrect tolerance or iterative step function. Any manual corrective adjustment required will be designated by this diagnosis and printed out in the literal form shown under the column "Diagnoses" in Part IV of this Appendix.

Diagnoses	Corrective Measure
1. Cladding tolerance too large	(a) Assumed value of TU is too small. Increase by factor of 2 or 3.
2. Too many iterations in cladding analysis	(a) Cladding tolerance, CLEPS, is too small.
	(b) Maximum iteration number, CLINOM, is too small. (Should solve in less than 100 steps.)
3. Too many iterations in fuel-form-length analysis	(a) Cladding thickness, TKASMD, assumed too small.
	(b) Fuel form tolerance, FFEPS, too large.
	(c) Maximum iteration number, FFINOM, too small.
4. Too many iterations for module adjustment	(a) Reduce module-heat source separation limitations, XMRFHS and XMRFWH.
	(b) Increase module adjustment iteration limit.
5. Too many iterations in heat balance	(a) Engineering efficiency tolerance, EEEPS, is too small.
	(b) Engineering efficiency iterative step, EEDEL, is too small.
	(c) Maximum iteration number, EEINOM, is too small.
6. Element cannot be iterated upon	(a) Reduce element minimum length, ELMIN.
	(b) Reduce module-heat source separation limitations, XMRFHS and XMRFWH.

7. **************

(a) Input or output data are greater than allowed number of places to the left of the decimal point. Change print format.

8. Too many iterations for radiator analysis.

(a) Radiator tolerance, REPS, too small.

(b) Radiator iterative step, RDELL, is too small if RINOL > RINOLM.

(c) Either radiator iterative step, RDELS, is too small if RINOS > RINOSM or RDELL is too large in case RINOL << RINOLM.

(d) Maximum iteration number, RINOLM or RINOSM, is too small.

APPENDIX B

ANALYTICAL EXPRESSIONS FOR SIZING
THE HEAT-SOURCE SUPPORT

APPENDIX B

ANALYTICAL EXPRESSIONS FOR SIZING THE HEAT-SOURCE SUPPORT

The heat-source-support analysis is based upon the compression and shear equations for support. The bearing force is the product of the g-factor for the acceleration of gravity and the mass of the heat source to be supported. The bearing area required for a specific tolerable deflection and support-material modulus of elasticity and thickness can be calculated. The equations are listed according to the support method, and the acronyms are defined in the Glossary of Terms (Appendix A, Part I).

(a) Support by ends only:

$$AEA = 0.785 \times (DHS^2)$$

$$AERQD = WHS \times GA \times QXE/(ECE \times TMDE)$$

$$AERQDS = WHS \times GR \times QXE/(ESE \times TMDR \times 2)$$

(b) Support by ends and radial portion:

$$AEA = 0.785 \times (DHS^2)$$

$$ARA = XLMDL \times 3.14 \times DHS \times (1 - (2 \times CNNO \times (ASINF (WDMDL/DHS))/6.28)) + 0.5 \times (XLHS - XLMDL) \times DHS \times 3.14$$

$$ARRQD = (WHS \times GR - 2 \times WHS \times GA \times ESE \times TMDR/(ECE \times TMDE))/CECR \times TMOR/(CNNO \times QXR) - EXR \times TMDE \times QXE/(ECE \times TMDE \times QXR))$$

$$AERQD = (WHS \times GA - ARRQD \times ESR \times TMDE/QXR) \times QXE/(ECE \times TMDE)$$

(c) Supported by radial portion only:

$$ARA = XLMDL \times 3.14 \times DHS \times (1-(2 \times CNNO \times (ASINF (WDMDL/DHS))/6.28)) + 0.5 \times (XLHS - XLMDL) \times DHS \times 3.14$$

$$ARRQDC = WHS \times GR \times CNNO \times QXR/(ECR \times TMDR)$$

$$ARRQDS = WHS \times GA \times QXR/(ESR \times TMDE).$$